
CONTROL OF THE UNIDIRECTIONAL MOTOR IN
RHODOBACTER SPHAEROIDES

MOSTYN T. BROWN

A THESIS SUBMITTED IN PARTIAL FULFILLMENT OF
THE REQUIREMENTS FOR THE DEGREE OF
DOCTOR OF PHILOSOPHY AT THE UNIVERSITY OF OXFORD



MERTON COLLEGE
UNIVERSITY OF OXFORD
TRINITY TERM 2009

ABSTRACT

CONTROL OF THE UNIDIRECTIONAL MOTOR IN *Rhodobacter sphaeroides*

MOSTYN T. BROWN

THESIS SUBMITTED FOR THE DEGREE OF DOCTOR OF PHILOSOPHY,
UNIVERSITY OF OXFORD, TRINITY TERM 2009

The control of the flagellar motor in *Rhodobacter sphaeroides* was investigated. Unlike most flagellar motors which are controlled by reversing the direction of rotation, the *R. sphaeroides* motor is controlled via a stop-start mechanism. Advanced optical microscopy was employed alongside genetic, biochemical, and behavioural techniques.

High-resolution measurements of rotating beads on flagellar stubs revealed that the *R. sphaeroides* motor is similar to its *E. coli* counterpart, rotating counterclockwise at comparable torques/speeds (1,300 pNnm/rad at stall torque), and exhibiting transient step changes in speed. The mean stop duration, mean stop frequency (number of stops per s), and run bias (fraction of time spent rotating) of wild-type at steady-state were 0.66 ± 1.01 s, 0.31 ± 0.19 s⁻¹, and 0.80 ± 0.20 , respectively.

Manipulating signal inputs to the motor genetically, or by exposing cells to chemotactic stimuli revealed that (i) without chemotactic stimulation the motor rotates continuously, (ii) phosphorylated CheYs are required to stop the motor, and (iii) the chemotaxis system cannot control the speed of rotation of the motor (termed chemokinesis) as previously reported. Complementation studies revealed that CheY₃, CheY₄, and CheY₅ are functionally equivalent. The copy numbers per cell of important CheYs were found to vary greatly under the conditions tested (<1,000, ~3,000, ~60,000 for CheY₃, CheY₄, and CheY₆ respectively).

To determine how CheY-P binding causes the motor to stop, external force (viscous flow or optical tweezers) was applied to chemotactically stopped motors. CheY-P binding might either cause the torque-generating units to disengage from the rotor, analogous to a clutch, or trigger the rotor to jam, analogous to a brake. The rotor resisted re-orientation during a chemotactic stop implying that the motor was held in a locked state. The value of torque resisting forward motion (keeping it locked) was estimated to be 2–3 x stall torque (2,500–4,000 pNnm/rad).

Furthermore beads attached to flagellar stubs stop at fixed angles for several seconds, showing no large-scale Brownian motion. Step analysis revealed that these stop events occur at 27–28 *discrete* angles around the motor, which most likely reflect the periodicity of the rotor (i.e. copies of FliG). This represents the first experimental resolution of steps in the rotation of a wild-type bacterial flagellar motor with a full complement of torque-generating units.

DECLARATION

The work in this thesis was undertaken at the University of Oxford; in the Microbiology Unit, Department of Biochemistry and in the Clarendon Laboratory, Department of Physics. Work was performed from October 2005 to October 2008 under the supervision of Prof. J.P. Armitage. All the work in this thesis is my own unless stated and has not been submitted for a degree at this or any other university.

PUBLICATIONS

A.C. Ind, S.L. Porter, E.D. Byles, S.A.C. Godfrey, **M.T. Brown**, and J.P. Armitage, *An inducible expression plasmid for Rhodobacter sphaeroides and its use to investigate chemotaxis*, In preparation.

T. Pilizota*, **M.T. Brown***, M.C. Leake, R.W. Branch, R.M. Berry, and J.P. Armitage, *A molecular brake, not a clutch, stops the Rhodobacter sphaeroides flagellar motor*, Proceedings of the National Academy of Sciences USA **106**, 11582-11587 (2009). *These authors contributed equally to this work.

ACKNOWLEDGEMENTS

Firstly, thanks to Judy Armitage for giving me the freedom and encouragement to do the experiments I thought were important. Secondly, Richard Berry for allowing a Biologist access to world-class Biophysical resources. In addition I would also like to thank past and present members of both labs for their invaluable help. In particular, Chien-Jung Lo, Richard Branch, Alice Ind, and Mila Kojadinovic. Mostly though, I would like to sincerely thank Steve Porter and Teuta Pilizota - I have learnt a great deal from both of you. Finally, BBSRC for funding, gratefully received.

ABBREVIATIONS

Ap^R	ampicillin resistance
AODs	acousto-optic deflectors
AVI	audio video interleave
BFP	back-focal-plane interferometry
d	derivative
D	distance moved
DIG	digoxigenin
dNTP	deoxynucleoside 5'-triphosphate
DSP	digital signalling processing
EDTA	ethylenediaminetetraacetic acid
F	force
f	viscous drag coefficient (pN nm s/rad ²)
HEPES	sodium N-2-hydroxyethylpiperazine-N'-2-ethanesulphonic acid
M_{CCW}	mean speed
MES	2-(N-morpholino)ethanesulfonic acid
ND	neutral density
OD	optical density
PBS_s	PBS buffer supplemented with 10 mM sodium succinate
PVDF	polyvinylidene fluoride
P_x	x-axis position coordinates
P_y	y-axis position coordinates
r	radius of bead
R_θ	cell body rebound angle
Sm^R	streptomycin resistance
T	torque
t	time
Tc^R	tetracycline resistance
T_{lock}	torque required to move the rotor out of its locked state
T_{max}	maximum torque
T_{stall}	stall torque
θ	angle
ω	angular velocity (rad/s)
κ	stiffness (pN nm/rad ²)
k_θ	tether stiffness
η	viscosity

*To anyone who believes in trying something,
just to see what happens...*

CONTENTS

1	LIFE AT LOW REYNOLDS NUMBER	1
1.1	LIFE FROM A BACTERIUM'S PERSPECTIVE	2
1.2	MOTILITY AND TAXIS IN MODEL SPECIES	3
1.2.1	MOTILITY	3
1.2.2	THE CHEMOTAXIS PARADIGM	4
1.2.3	THE BACTERIAL FLAGELLAR MOTOR	7
1.2.4	SWITCHING	12
1.3	MOTILITY AND TAXIS IN <i>R. sphaeroides</i>	13
1.3.1	MOTILITY IN <i>R. sphaeroides</i>	13
1.3.2	THE COMPLEX CHEMOTAXIS SYSTEM OF <i>R. sphaeroides</i> . .	15
1.4	EXPERIMENTAL TECHNIQUES REVIEW	19
1.4.1	TAXIS ASSAYS	19
1.4.2	AN INTRODUCTION TO ROTATION RATE MEASUREMENTS .	21
1.4.3	BACK-FOCAL-PLANE INTERFEROMETRY	24
1.4.4	OPTICAL TRAPPING	28
1.5	AIMS OF THIS PROJECT	30
1.6	RAW DATA AND PROTOCOLS AVAILABLE ONLINE	30
2	MATERIALS AND METHODS	31
2.1	MOLECULAR MICROBIOLOGY	31
2.1.1	GENERAL GROWTH CONDITIONS	31
2.1.2	MOLECULAR GENETIC TECHNIQUES	35
2.2	PHENOTYPIC ANALYSIS OF CELL POPULATIONS	41
2.2.1	CELLULAR PROTEIN QUANTIFICATION	41
2.2.2	LIGHT MICROSCOPY	43
2.2.3	SWIM-PLATES	43
2.2.4	GROWTH RATES	44
2.3	SINGLE CELL ANALYSIS	44
2.3.1	TETHERED CELL ASSAY	45
2.3.2	<i>R. sphaeroides</i> BEAD ASSAY	45
2.3.3	BFP INTERFEROMETRY AND OPTICAL TRAP SETUP	47
2.3.4	DATA ANALYSIS	48

3	WILD-TYPE MOTOR OUTPUT: SPEED, TORQUE AND STOPS	50
3.1	OVERVIEW AND AIMS	50
3.2	RESULTS	51
3.2.1	THE <i>R. sphaeroides</i> BEAD ASSAY	51
3.2.2	THE MOTOR ROTATES CCW NOT CW	51
3.2.3	WILD-TYPE STOP EVENTS	55
3.2.4	PLATEAU TORQUE	57
3.2.5	TRANSIENT STEP CHANGES IN SPEED	59
3.3	CONCLUSIONS	59
4	FUNDAMENTAL MOTOR CONTROL	61
4.1	OVERVIEW AND AIMS	61
4.2	RESULTS	61
4.2.1	‘DEFAULT’ MOTOR BEHAVIOUR	61
4.2.2	CHEYS STOP THE MOTOR WHEN PHOSPHORYLATED	62
4.2.3	MOTILITY AND MOTOR SPEED IN PBS BUFFER	63
4.2.4	THE CHEMOTAXIS SYSTEM DOES NOT CONTROL MOTOR SPEED	65
4.3	CONCLUSIONS	67
5	MOTOR CONTROL AT THE MOLECULAR LEVEL	68
5.1	OVERVIEW AND AIMS	68
5.2	RESULTS	69
5.2.1	PHENOTYPES OF <i>flhM</i> ₁ POINT MUTANTS	69
5.2.2	PHENOTYPES OF <i>cheY</i> ₃ <i>cheY</i> ₄ POINT MUTANTS	72
5.2.3	COPY NUMBERS OF CHEY _{3/4/6} PER CELL	75
5.2.4	PROTEIN QUANTIFICATION FROM pIND4	78
5.2.5	$\Delta cheY_6$ COULD NOT BE COMPLEMENTED	80
5.2.6	CHEY ₅ IS FUNCTIONALLY EQUIVALENT TO CHEY ₃ /CHEY ₄	82
5.2.7	EFFECT OF EXPRESSION OF <i>E. coli</i> GENES ON <i>R. sphaeroides</i> BEHAVIOUR	84
5.2.8	STOP FREQUENCIES OF STRAINS OVEREXPRESSING CHEYS	86
5.3	CONCLUSIONS	87
6	THE STOP MECHANISM	92
6.1	OVERVIEW AND AIMS	92
6.2	RESULTS	93
6.2.1	APPLICATION OF EXTERNAL TORQUE USING VISCOUS FLOW	93
6.2.2	EXTERNAL TORQUE USING AN OPTICAL TRAP	94
6.2.3	STOPS OCCUR AT DISCRETE ANGLES	97
6.3	CONCLUSIONS	100
7	DISCUSSION AND FUTURE WORK	102
	BIBLIOGRAPHY	107

A	APPENDIX - MEDIA RECIPES AND REAGENTS	120
B	APPENDIX - MOLECULAR MICROBIOLOGY	122
B.1	PLASMID MAP - pIND4	122
B.2	PRIMERS	123
C	APPENDIX - SUPPLEMENTARY DATA	125
D	DIGITAL APPENDIX - ONLINE RESOURCES	131
D.1	THESIS	131
D.2	VIDEOS	131
D.3	MY PROTOCOLS	131
D.4	BEAD ROTATION DATA	131

LIFE AT LOW REYNOLDS NUMBER

Microchips allow fast, controlled communication between components that are physically connected by an electrically conducting material. But Biology at the nanoscale processes information in a radically different way, using chemical signals as well as electrical ones, relayed via messenger molecules, not wires. This invariably involves shape changes in the molecule transmitting the signal. When the ‘shape-changing propensity’ of this molecule is regulated by the binding of another molecule, which in turn is regulated by other molecules, one starts to appreciate the complexity of life.

Hence, in order to make any headway at all, research has tended to focus on simple organisms such as bacteria, worms, flies and fish, as models for understanding more complex systems. Chemotaxis, the foraging behaviour of bacteria, is best characterised in *Escherichia coli* and *Salmonella enterica* where it is used as a model for understanding principles that underlie communication and logic in all biological systems. The operation of the flagellar motor, nature’s most complex rotary motor, is of interest in its own right particularly as bionanotechnology advances.

This project aims to expand what is known about (i) biological control systems, and (ii) the flagellar motor, by investigating motor control in *Rhodobacter sphaeroides* which uses a complicated chemotaxis system to control a largely uncharacterised motor. This chapter draws together information about the chemotaxis pathways in *E. coli* and *R. sphaeroides*, the flagellar motor, and assays which enable its output to be measured. The aims of this project are then discussed before revealing how experiments were performed and what they revealed. Throughout, it is important to remember what it is like to live from a bacterium’s perspective, in a low Reynolds number environment.

1.1 LIFE FROM A BACTERIUM'S PERSPECTIVE

Bacteria have all the characteristics one would expect from a group of organisms that have undergone millions of years of natural selection. They are small, can reproduce quickly and are incredibly diverse. Moreover, they can swap genes between distantly related species via lateral gene transfer. This makes them a formidable biological force responsible for the continued survival of species higher up the food chain, including ourselves.

Bacteria are so small that they are affected by natural forces in ways we are unaccustomed to. For instance, unlike us, bacteria do not coast when they stop swimming; they stop almost instantaneously (0.004 nm) [1]. The Reynolds number ($\frac{\text{inertial forces}}{\text{viscous forces}} = \frac{\text{Size} \cdot \text{Velocity} \cdot \text{Density}}{\text{Viscosity}}$) is used as a measure of which of the two types of force, inertia (arising from the object's momentum) or viscosity (the amount of resistance the fluid exerts on the object), is the dominant factor that limits movement through fluids.¹ Examples of some characteristic Reynolds numbers for self-propelled organisms are shown in Table 1.1.

Organism type	Reynolds number
A large whale swimming at 10 m/s	300,000,000.0
A large dragon fly going 7 m/s	30,000.0
Flapping wings of the smallest flying insects	30.0
A sea urchin sperm swimming at 0.2 mm/s	0.03
A bacterium, swimming at 0.01 mm/s	0.00001

Table 1.1: A spectrum of Reynolds numbers for self-propelled organisms taken from [2]. The Reynolds numbers range from very large values, for a swimming whale, to extremely small values for swimming bacteria. That means that a whale, where inertial effects dominate, will continue to 'coast' for a substantial distance and time after it has stopped actively swimming. For a bacterium on the other hand, inertial effects are irrelevant and viscous effects dominate, so that a bacterium will stop almost instantaneously.

There are several fascinating consequences of living at a low Reynolds number. For instance only rotary (not reciprocal) motion will propel objects forward and steering devices such as rudders do not work well. But perhaps the most important consequence of living in the micro-scale is that Brownian motion is rife. This has governed the evolutionary design of behavioural strategies, intracellular signalling-pathways, and the molecular machines they control:

- Chemicals on the micro-scale will be mixed by Brownian motion, meaning that bacteria cannot sense concentration gradients along their cell body directly.

¹An excellent informal paper, *Life at Low Reynolds Number* (Purcell, 1976), is available online at <http://dx.doi.org/10.1119/1.10903>

- If a bacterium is going to expend energy swimming/building a rotary motor, it must be able to swim fast enough to outrun diffusion. This also has repercussions for chemotactic strategies.
- Transmitting signals by diffusion is fast over short distances.²
- Brownian motion is responsible for conducting heat energy away from small objects. Subsequently it is impossible to replicate any kind of heat motor (e.g. an internal combustion engine) on the nanoscale, because it is impossible to keep compartments at different temperatures.

The vastly different and non-intuitive nature of the environment at this scale is what nanotechnologists hope to exploit. Biology has mastered the nanoscale; in particular through the control and operation of sophisticated molecular machines such as the flagellar motor.

1.2 MOTILITY AND TAXIS IN MODEL SPECIES

1.2.1 MOTILITY

Unlike swimming animals that use muscle, bacteria swim by *rotating* a propeller, reaching speeds of up to 500 body lengths per second.³ The propeller, a long thin rigid helical filament (15 nm x 5–15 μ m) is coupled to the flagellar motor situated at its base by a flexible hook (15 nm x 80 nm) [3, 4]. The filament consists of 11 protofilaments, made from the polymerisation of a single protein, FliC. The FliC monomers polymerise in one of two conformations, long or short, forming either long or short protofilaments respectively. A mixture of long and short protofilaments causes the filament to form a helix [5]. In multi-flagellated bacteria the hook serves as a universal joint allowing filaments from several motors positioned randomly over the cell to come together at the pole.

H.C. Berg explains in simple terms why rotation of this helical filament generates thrust [6]. “The viscous drag on a thin rod is about twice as great when the rod moves sideways as when it moves lengthwise. Thus, when oriented slantwise and pulled downward through a viscous medium, a rod moves to one side.” So, by rotating a helical filament (in effect, a series of slantwise rods), the cell can propel itself forward.

²An oxygen atom will take a few milliseconds to move 10 nm, a minute or so to go a micron, and a hundred years to move one centimetre by pure diffusion.

³For comparison, the cheetah travels at bursts of speed up to 30 body lengths per second.

1.2.2 THE CHEMOTAXIS PARADIGM

The *E. coli* chemotaxis system, responsible for the ability to sense and respond to environmental chemical stimuli, has become a paradigm for signal transduction in biological systems. At $\sim 2 \mu\text{m}$ long and $\sim 0.8 \mu\text{m}$ wide, it is impossible for *E. coli* to sense a difference in concentration from one end of the cell to the other. Since they cannot steer directly, they swim in a biased 3D random-walk, alternating between ‘runs’ and ‘tumbles’ (Figure 1.1). Tumbles occur when flagellar motors ‘switch’ the direction of rotation from counterclockwise (CCW) to clockwise (CW), as viewed from the distal end of the filament. In *E. coli* the mean run interval is about 1 s, the mean tumble interval is about 0.1 s, and the CCW bias (fraction of time spent rotating CCW) is about 0.6–0.7 [7]. During a tumble, the reversed filament comes out of the bundle and transforms from a left-handed to a right-handed helix [8].

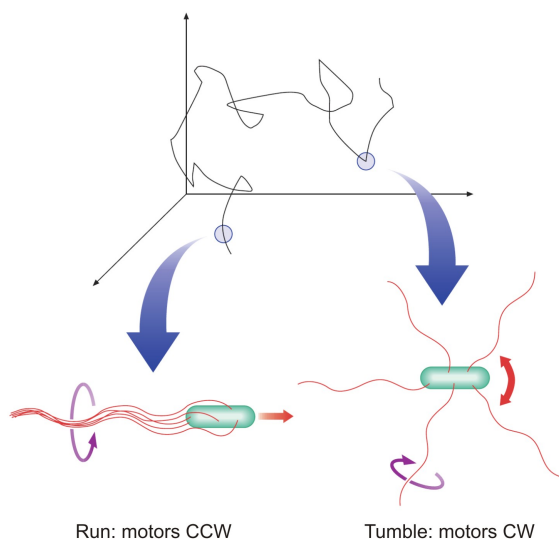


Figure 1.1: An *E. coli* cell swims in a series of ‘runs’ and ‘tumbles’. Rotating 4–10 right-handed helical filaments in the CCW direction push the cell forward in a run. The flexible hook enables the filaments from different motors to form a bundle that propels the cell forward. In a tumble, motors rotate in the CW direction, forcing the bundle to fly apart, which causes the cell to become reoriented. When it starts to swim again it is in a random direction. Figure taken from www.els.net.

So how does the cell know when to tumble? Over 40 years of research to answer this simple question has meant that the chemotaxis pathway is now extremely well-characterised (reviewed in [9]). The cell compares what the chemoeffector concentration is like ‘now’, relative to 3–4 s ago [10]. Remarkably, this works without a dedicated processor that one would find in a robot or higher organism.

Signals are transmitted via a ‘two-component signal transduction system’ consisting of a histidine protein kinase (CheA) and response regulators (CheY and CheB). Two-component signalling is utilised in other bacterial pathways e.g. nitrogen sensing, phosphate utilization, osmosensing and sporulation. In all cases the rate of autophosphorylation of the histidine protein kinase is stimulus-dependent. Phosphoryl groups are then transferred to a conserved aspartate residue on cognate

response regulators. Phosphorylation of the response regulator causes a conformational change, which alters its activity, producing an appropriate response to the original stimulus.

The chemotaxis system regulates the cytoplasmic concentration of phosphorylated CheY (CheY-P) in response to changes in the external concentrations of attractant or repellent (Figure 1.2). External chemoeffector concentration is detected by Methyl-accepting Chemotaxis Proteins (MCPs). MCPs form a large multiprotein complex with CheA and CheW at the cell poles. This allows the integration of signals from five different types of sensor, each of which detect different stimuli, and all of which mediate some response to repellents.

A reduction in the levels of chemoattractants bound to transmembrane MCPs trigger CheA autophosphorylation at His-48, resulting in phosphotransfer to one of the response regulators, CheY (Asp-57) or CheB (Asp-56). Upon phosphorylation, CheY adopts an active conformation; the salt bridge between Lys-109 and Asp-57 is broken, allowing hydrogen bond formation between Thr-87 and the $\beta 4$ - $\alpha 4$ loop [11], forcing Tyr-106 from a surface exposed to a buried conformation [12]. Phosphorylation of CheY increases its affinity for FliM, situated at the base of the flagellar motor, 20-fold [13]. How the binding of CheY to FliM causes a switch is discussed in Section 1.2.4.

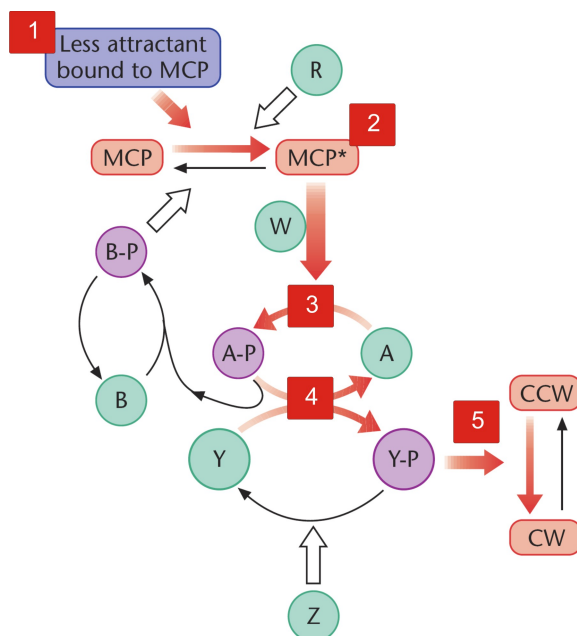


Figure 1.2: Triggering a switch in *E. coli*. *Step 1* The attractant concentration in the environment decreases, which is detected by the sensors (MCPs) that span the membrane at the poles of the cell. *Step 2* MCPs undergo a conformational change. *Step 3* This causes the CheA dimer, which is held in a complex with the MCPs and CheW, to trans-autophosphorylate. *Step 4* This phosphoryl group is then transferred to CheYs, which adopt an active conformation and diffuse throughout the cytoplasm. *Step 5* CheY-P binds to the base of the flagellar motor to cause the motor to switch from CCW to CW. Figure taken from www.els.net.

The key to chemotaxis is knowing *when* to switch. The system outlined above illustrates how this can be achieved when we consider that CheY phosphorylation is stimulus-dependent; the larger the decrease in the concentration of attractants, the

higher the concentration of CheY-P, and the higher the probability that a switch will occur. However the signal termination and adaptation mechanisms make the control system in *E. coli* considerably more sophisticated.

1. Signal termination. The level of CheY-P is regulated in two ways; through phosphorylation via CheA, and dephosphorylation via the phosphatase CheZ. *E. coli* CheY-P typically auto-dephosphorylates in about 10 s, but this reaction is enhanced by a factor of approximately 100 by CheZ [14]. Termination of the signal ensures that cells are free to respond to new stimuli.

2. Adaptation. The more MCPs are exposed to their substrates, the less sensitive they become. CheR (a methyltransferase) constitutively methylates specific glutamates in MCPs making them more sensitive, whilst the methylesterase, CheB, de-methylates them in a phosphorylation-dependent manner. Like CheY, CheB is phosphorylated by CheA with reduced attractant concentrations increasing phosphorylation of CheB. This enhances its methyl-esterase activity 100-fold, decreasing receptor methylation levels, which makes them less sensitive. Adaptation enables the chemotaxis system to operate over a wide range of background concentrations.

The chemotaxis pathway controls when the direction of motor rotation is reversed. In the next two sections we consider the current explanations of (i) how torque is generated in the motor, and (ii), how the binding of the intracellular signal molecule, CheY-P, causes the motor to switch the direction of rotation.

1.2.3 THE BACTERIAL FLAGELLAR MOTOR

The motor, shown in Figure 1.3, is formed from the products of ~ 40 genes, which are expressed in a particular sequence that results in self-assembly across the cell membrane (reviewed in [15]). The motor consists of a central rotor surrounded (in *E. coli* at least) by approximately eleven stator complexes [16]. Torque is generated at the periphery of the rotor by the translocation of ions into the cytoplasm through the stator complexes.

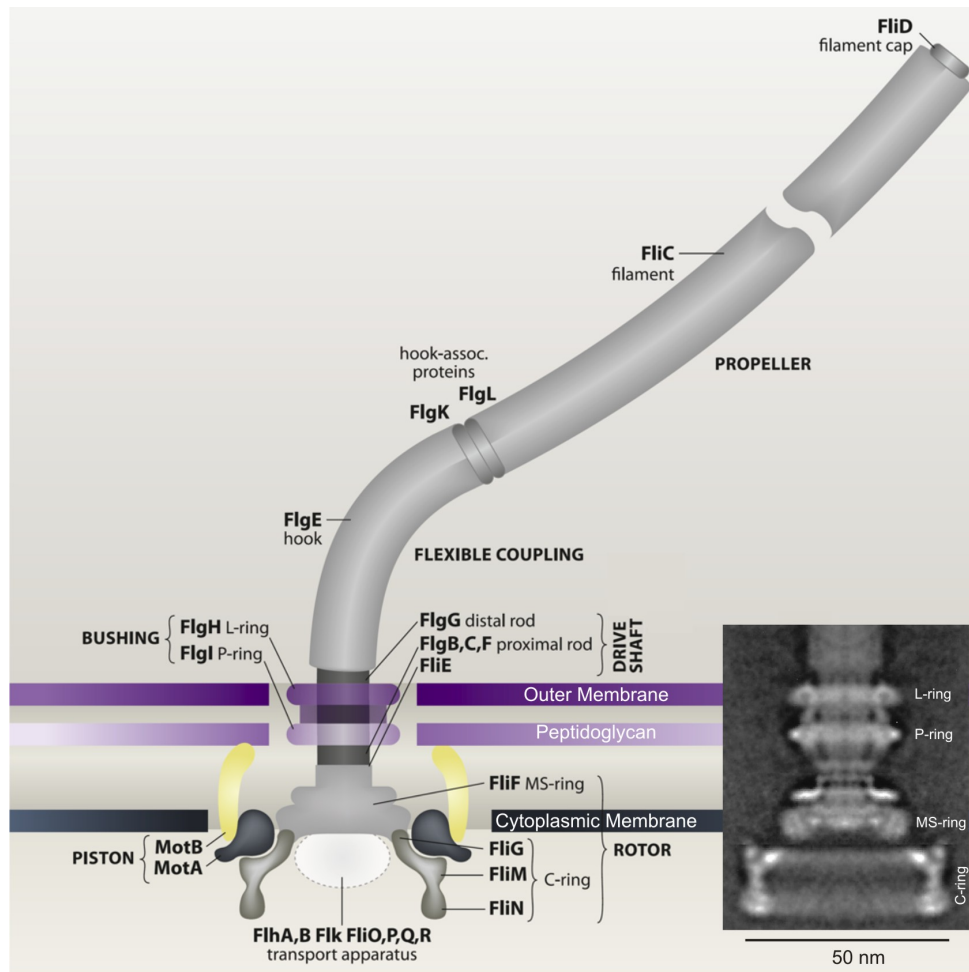


Figure 1.3: A schematic of the bacterial flagellar motor based on an electron micrograph (EM) (adapted from [17] and [18]). The core of the motor is called the ‘basal body’ that spans the cell envelope. The L and P rings are thought to be embedded in the outer lipopolysaccharide membrane and peptidoglycan cell wall, respectively. They may work as a bushing between the rotor and the outer parts of the cell envelope. The flow of ions from the periplasm into the cytoplasm through channels in the stator complexes, drives the rotation of the motor. The switch complex (FliG, FliM, and FliN) is responsible for generating torque of the appropriate sign, dependent on cytoplasmic CheY-P levels. See [19] and [20] for full flagellar motor reviews.

TORQUE-GENERATING UNITS

In proton-driven motors the torque-generating units comprise two proteins in the stoichiometry $\text{MotA}_4\text{MotB}_2$ [21]. In order to make the rotor turn, the stator complexes need something to push against. They are anchored to the cell wall via a putative peptidoglycan-binding motif ($\text{LSX}_2\text{RA}_2\text{V}_3\text{L}$) within the C-terminal periplasmic domain of MotB [22, 23]. It is proposed that this domain plugs the channels in the stators until they assemble at the motor [24]. The linkage between the stator and peptidoglycan must be extremely strong - the stators can generate enough torque around the 45 nm rotor to push the whole cell body, as seen in the tethered cell assay.

Given this fact, one would expect the stators to be firmly incorporated into the motor upon assembly, never to be moved again until the whole motor is recycled by the cell. However, remarkably it was found that the stator complexes diffuse in and out of the motor whilst it is rotating at full speed [25]. This has also been observed when *mot* genes are expressed from a plasmid in a *mot* deficient strain, whereby speed increases in successive steps in a process called *resurrection* (Figure 1.4) [26].

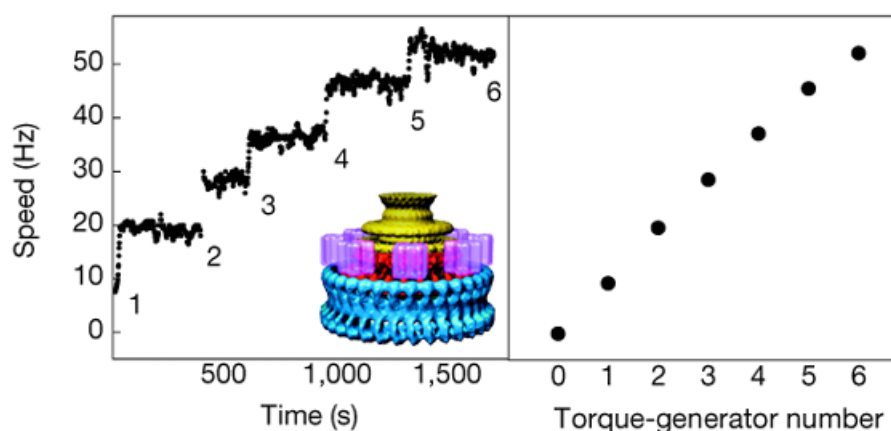


Figure 1.4: Speed-time trace of a motor undergoing resurrection (1.03 μm diameter bead on flagellar stub) (taken from [27]). The number of torque-generating units is inferred from the discrete speed levels. *Inset*, a 3D reconstruction from electron cryomicrographs of the rotor; the positions of the stator units (purple) are hypothetical (taken from [28]).

THE SWITCH COMPLEX

The switch complex (Figure 1.5) contains about 26 copies of FliG, 34 copies of FliM, and more than 100 copies of FliN [29] (see latest summary [30]). FliM and FliN are important in changing the direction of motor rotation in response to CheY-

P binding, whereas FliG is primarily involved in interacting with MotA to generate torque. It is unclear how the ~ 34 FliM proteins, which bind the CheY-P, are connected to the ~ 26 FliG proteins that alter the direction of torque.

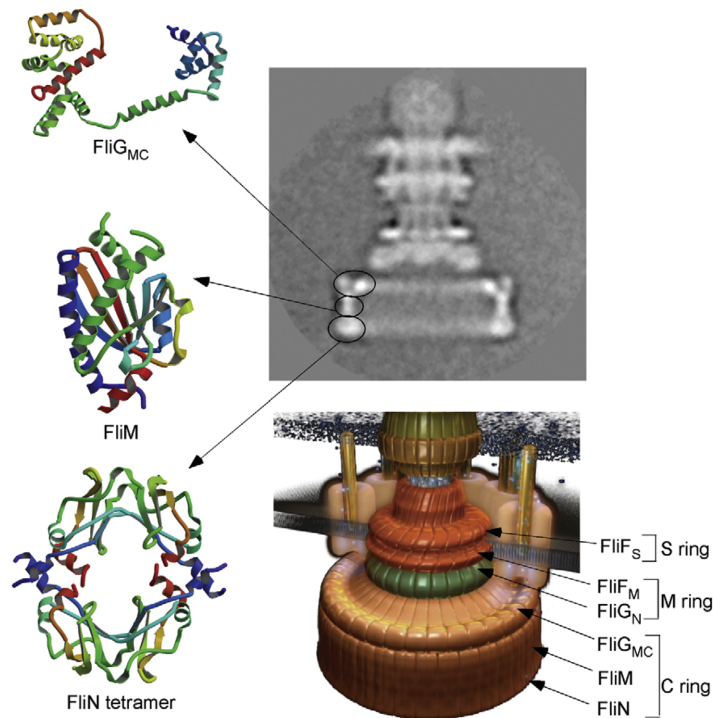


Figure 1.5: The switch complex (figure taken from [31]). *left* Crystal structures of FliG_{MC} (middle and C-terminal domains), FliM, and FliN. *Right upper* Electron cryomicroscopic image of frozen-hydrated hook-basal body in the side view obtained by averaging many images. Arrows indicate the correspondence between domains of the C ring and component proteins. *Right lower* Proposed location of FliF, FliG, FliM, and FliN in the MSC ring.

MOTOR ‘FUEL’

Whilst building the flagellum is an energetically expensive process, operating it requires very little energy. In the process of respiration or photosynthesis, electron transport chains pump protons out of the cytoplasm across the inner membrane. Protons accumulate in the periplasm since the inner membrane is impermeable. Despite the presence of an electrochemical gradient they can only re-enter the cell via specific channels such as F₁F_o-ATPase and MotA₄MotB₂. The protonmotive force (*pmf*) corresponds to the work per unit charge that a proton can do in crossing the cytoplasmic membrane.

Motors found in species like *E. coli* and *S. enterica* run on protons, whereas motors in alkalophilic *Bacillus* and marine *Vibrio* species run on sodium ions. Sodium-

driven motors typically rotate much faster than proton-driven motors. In 2000 it was discovered that hybrid stators consisting of Na^+ - and H^+ -type subunits can work together, resulting in motor rotation [32]. Subsequently several other types of chimaeric motor have been constructed allowing a motor that was originally powered by protons to run on sodium ions [33]. One chimaera that has been used extensively studied uses stators PomA (*V. alginolyticus* MotA homologue) and PotB (a chimaeric protein containing the periplasmic C-terminus of MotB from *E. coli* and the membrane-spanning N-terminus of PomB from *V. alginolyticus*) to form a sodium-driven motor in *E. coli* [33]. This motor/strain is referred to as ‘the chimaera’ throughout this thesis.

TORQUE-SPEED RELATIONSHIP

Motor power (P) is the product of torque (T) and angular velocity (ω) ($P = T \cdot \omega$). Examining the shape of the torque-speed curve provides a crude map of how that power is generated. Torque ($T = \text{viscous drag of object being rotated} \times \text{angular velocity}$) is a measure of the ‘force’ being used to turn (or attempting to turn) an object. Torque-speed curves are constructed by measuring motor speed whilst varying the motor’s load (viscous drag). The bead assay (see Section 1.4.2, Page 21) provides a simple way of varying the viscous drag since it is dependent upon the bead’s diameter, the radius of its orbit and the viscosity of the solution. Increasing the size of the bead or viscosity of the solution increases viscous drag. The mass of the bead does not significantly contribute to the drag and is thus neglected.

Torque-speed curves have been constructed for flagellar motors from several different species (see summary in [34]). They tend to have similar shapes, consisting of a ‘plateau’ of nearly constant torque at low speeds and a much steeper linear decrease in torque with speed at higher speeds (Figure 1.6).

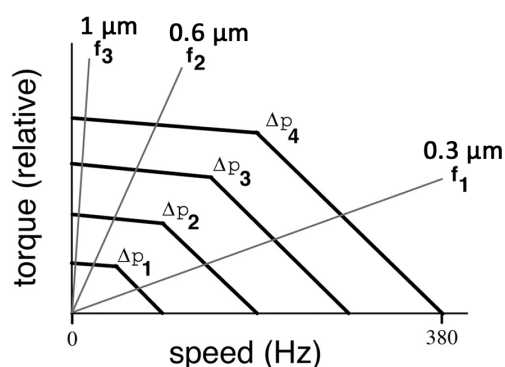


Figure 1.6: Schematic of the torque-speed curve of the wild-type flagellar motor from *E. coli* (taken from [35]). The drag coefficients ($f_1 < f_2 < f_3$) for three different bead diameters are shown. The motor runs at a speed at which the torque generated matches the viscous drag of the bead. Also shown is the ‘idealised’ torque-speed curves of a motor at four different *pmfs*, Δp_1 – $\Delta p_4 = 25\%$, 50% , 75% , and 100% , respectively.

This shape is preserved elsewhere, like in the torque-speed profile of a cyclist, which provides a convenient analogy [36]. At very low speeds, the rider can push the pedals with all his force, and will produce constant torque. But if he is going very fast downhill, there comes a point where he can only just move his legs around fast enough to keep up with the pedals, and is not pushing at all. Here, all his efforts are being dissipated in the motion of his legs. Just as in the flagellar motor, the plateau region represents a regime where the internal processes are not rate limiting. However at lower loads, torque is much reduced, indicating that the speed of rotation is limited by internal processes; in the case of the flagellar motor this could be due to the local availability of ions.

MECHANISM OF TORQUE GENERATION

Whilst it is not known exactly how ion translocation causes the stators to generate torque, a general mechanism is well-established. Binding/release of a proton (or pair of protons) to Asp-32 of MotB may trigger a conformational change in MotA which is transmitted to FliG of the rotor via electrostatic interactions (see Figure 1.7 for the location of functionally important residues). This would cause the rotor to advance one step. There are approximately 26 steps per revolution corresponding to the number of FliG proteins that make up the ‘track’ that the stators run on [37]. The stators may be synchronised (i.e. in similar phases of their torque-generating cycle) since they are all attached to the same rotor ring. The conformation of the rotor is thought to dictate which direction it is pushed by the stators.

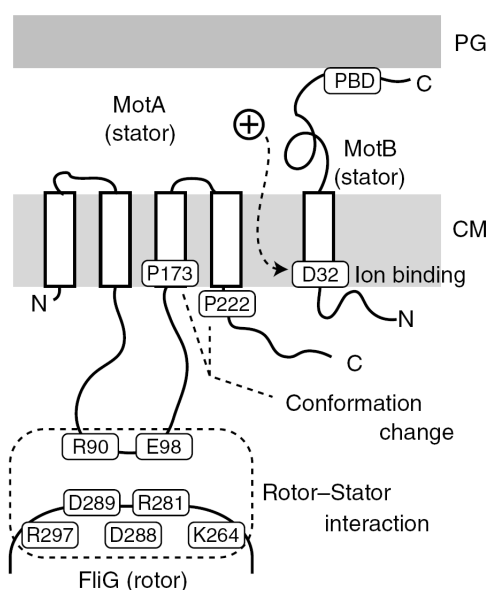


Figure 1.7: Functionally important residues in MotA, MotB and FliG identified in mutational studies taken from [20]. The conserved Asp-32 residue in MotB is critical for rotation and probably functions directly in proton transfer [38]. Certain combinations of MotA mutations with FliG mutations show strong synergism or suppression, in a pattern that indicates that the charged groups of MotA interact with those of FliG. PG, PBD, CM = peptidoglycan, peptidoglycan-binding domain, cytoplasmic membrane respectively.

1.2.4 SWITCHING

How does binding of CheY-P to FliM cause the motor to switch direction (often within 10 ms), while generating the same torque in either direction [39]? Rather than the reversal of ion flow, it is much more likely that the motor genuinely ‘changes gear’. That is to say, the stators carry on as normal, but the effect is to force the rotor in the other direction. It is thought that binding of CheY-P to the N-terminus of FliM, causes FliG to change conformation which results in different electrostatic interactions at the rotor-stator interface (Figure 1.8). Note that FliN may contribute to the binding site for CheY [40].

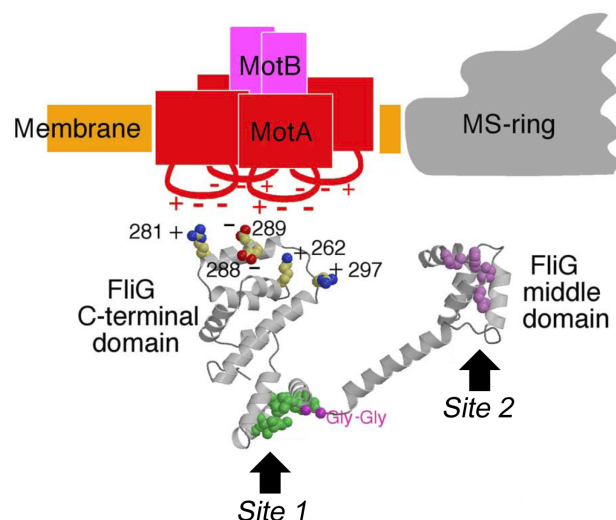


Figure 1.8: The current working model to explain how the flagellar motor switches (based on [41] and supported by [42] and [30]). FliG is anchored to the rotor via its N-terminus (not shown), whilst the C-terminus of FliG interacts with MotA to generate torque in either direction. Sites 1 and 2 refer to two alternative associations of a FliM monomer with FliG. It is hypothesised that CheY-P binding causes FliM to bind to Site 1 rather than the default Site 2 of FliG. This changes the position of the C-terminus of FliG which causes the motor to rotate in the alternative direction. The hinge region (Gly-Gly) of FliG maybe critical in providing this C-terminal flexibility [43, 44].

The motor tends to rotate full speed in either direction - it spends very little time switching between states. This is characterised by the steep input-output relation between CheY-P binding and motor bias [45]. CheY-P and FliM do not bind cooperatively (tested *in vivo*) [46]. Thus a model termed ‘conformational spread’ (a form of allostery reviewed in [47]) has been proposed to explain this ‘ultrasensitivity’. A free-energy penalty for adjacent FliM proteins in different states (‘CCW’ or ‘CW’) means that the rotor is most stable with all the proteins in either the CW or CCW states [48].

1.3 MOTILITY AND TAXIS IN *R. sphaeroides*

It is clear from studying chemotaxis in other bacteria, that *E. coli* has an atypically simple chemotaxis system. Most bacterial species, such as *R. sphaeroides* have more complicated systems (reviewed in [49]). The subject of this project was to investigate motor switching in *R. sphaeroides*. By comparing how chemotaxis systems are designed in species other than *E. coli* and *S. enterica* we can begin to learn more about how biological signalling pathways operate in general. This approach can be extended to investigating the *R. sphaeroides* flagellar motor, as it has some unusual characteristics compared to those examined previously. Before discussing these aspects, some background information about *R. sphaeroides* is provided below.

R. sphaeroides is a non-pathogenic α -proteobacterium that inhabits soil and water. It is approximately 1.6 μm long by 1.2 μm wide [50]. It has a minimum doubling time of 2 hrs compared to 20-30 mins for *E. coli*. Like other related organisms, it has a complex genome consisting of two circular chromosomes (CI and CII, 3.19 and 0.94 Megabases (Mb) respectively) plus several plasmids. *R. sphaeroides* can survive by assimilating resources from a number of sources (including the fixation of CO_2 and N_2 from air). It can also metabolise them in a number of different ways, growing either by aerobic or anaerobic respiration, fermentation, or photosynthesis. It exhibits taxis to weak organic acids (such as propionate), sugars, oxygen and light. These inputs are transmitted by the same core pathway. Responses to certain chemoeffectors vary with the conditions under which the cells have been grown e.g. only photoheterotrophically grown cells respond to light (phototaxis).

1.3.1 MOTILITY IN *R. sphaeroides*

R. sphaeroides motility has been studied for over 25 years. In this time, under all conditions tested, wild-type (WS8N) cells have only been observed to swim using a single flagellum (*fla1*) that rotates unidirectionally [51]. However upon sequencing it was discovered that the *R. sphaeroides* genome contains another set of *fla* genes that encode for a second flagellum (termed *fla2*). Whilst *fla1* system may have been acquired by lateral gene transfer, it is the only one used for swimming under lab conditions.

R. sphaeroides swims in a series of runs and tumbles (a video of swimming *R. sphaeroides* available in Appendix D.2, Page 131; rotation rates are slowed down by adding Ficoll to increase the viscosity of the solution). Tumbles occur when the motor stops. During a stop the cell is reorientated by Brownian motion. The

filament can undergo polymorphic transitions between apparently straight/helical forms when swimming (Figure 1.9), to a coiled form when stopped which perhaps facilitates re-orientation of the cell body [52]. It is thought that the filament consists of a right-handed helix (determined from 2D images of filaments from tethered cells) [53] which propels the cell forward when rotated in the CW direction (determined by observing the direction of rotation of tethered cells) [51]. Only the handedness of large-coiled form has been resolved by video analysis (dark-field microscopy) and was found to be right-handed [54]. The filament is connected to the motor via a straight hook [55], unlike the highly curved and flexible *E. coli* hook.

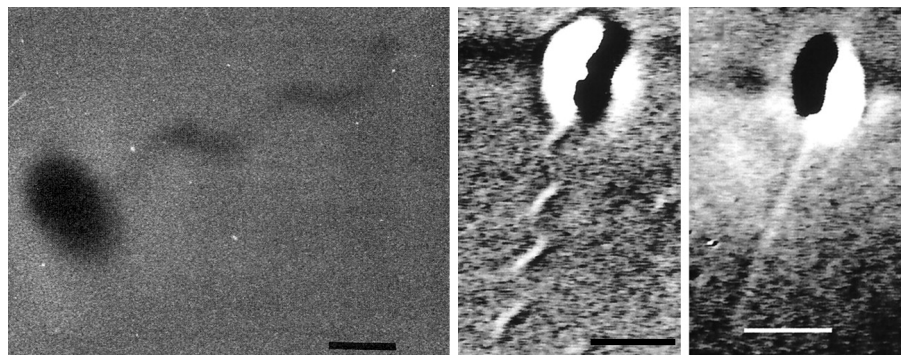


Figure 1.9: The *R. sphaeroides* flagellar filament from swimming cells. *Left*, antibody-decorated filaments of WS8N visualised using phase-contrast microscopy [53]. *Middle, Right*, differential interference contrast (DIC) images of the filament showing a helical and straight forms [52]. 1 μm bars are shown.

SINGLE UNIDIRECTIONAL FLAGELLUM (fla1)

Only four things are known for certain about the fla1 flagellum: (i) it only rotates in one direction [51], (ii) it is proton-driven [56], (iii) there is only one flagellum per cell, and (iv) it is not located at a cell pole. Even less is known about the fla2 flagella.

UNCHARACTERISED MULTIPLE POLAR FLAGELLA (fla2)

Whilst fla1⁻ mutants are non-motile, a recent study has generated a motile fla1⁻ suppressor mutant that expresses the fla2 genes producing multiple polar flagella [57]. In contrast to bacterial species which use a second flagellar systems for moving over surfaces (known as swarming), the second flagellar system of *R. sphaeroides* produces flagella that are used for swimming.

WILD-TYPE MOTILITY REVISITED

It is not known whether *fla2* genes are ever expressed in wild-type *R. sphaeroides* but they are not seen in transcription profiles (S. Kaplan, personal communication). The working assumption has been that they are not (since *fla1*[−] mutants are non-motile). However, a recent discovery questions that assumption. Deletion of *fliM*₂ from the *fla2* gene set does reduce taxis in WS8N under laboratory conditions (E. Byles and S.L. Porter, unpublished). It is unknown why this occurs and the discovery is so recent that the deletion has yet to be complemented.⁴

1.3.2 THE COMPLEX CHEMOTAXIS SYSTEM OF *R. sphaeroides*

The *R. sphaeroides* genome encodes multiple chemotaxis homologues organised in three *che* operons and two *che* gene clusters (Figure 1.10). The remaining *che* genes seem to be positioned at random. *cheOp*₁ is not required for wild-type taxis under any condition tested so far, and is presumed not to be expressed under lab conditions. Fluorescent fusions show that the proteins encoded by *cheOp*₂ predominantly localise to the poles of the cell, whereas proteins encoded by *cheOp*₃ localise to a cluster in the cytoplasm [58]. Part (b) of Figure 1.10 depicts the current working model of the chemotaxis pathway in *R. sphaeroides* (recently reviewed in [59]), based on the phenotypes of deletions, sub-cellular localisation of fluorescent protein fusions [58], and *in vitro* phosphotransfer reactions. Attractants are thought to be sensed by the polar chemotaxis cluster, and signals reflecting the metabolic state of the cell are believed to be sensed by the cytoplasmic chemotaxis cluster.

Recent work has revealed additional complexity. (1) Three single-domain response regulators, encoded away from the other *che* genes, were identified and shown to impair wild-type taxis when deleted (S.L. Porter, unpublished). (2) CheA₃ is a specific kinase phosphatase for CheY₆-P, which could explain the absence of CheZ homologues in *R. sphaeroides* [60].

CHEY CONTROL OF *fla1*

Signalling from both pathways (polar and cytoplasmic) are essential for *fla1*-dependent chemotaxis [61]. Porter *et al.* showed that only two CheYs (CheY₆ and either CheY₃

⁴Complementation refers to the process where by the phenotypic effects of a mutation are restored to the wild-type phenotype, by expressing the gene that is deleted in the mutant from a plasmid. Only then can one be certain that the mutant phenotype is the result of the absence of that particular protein.

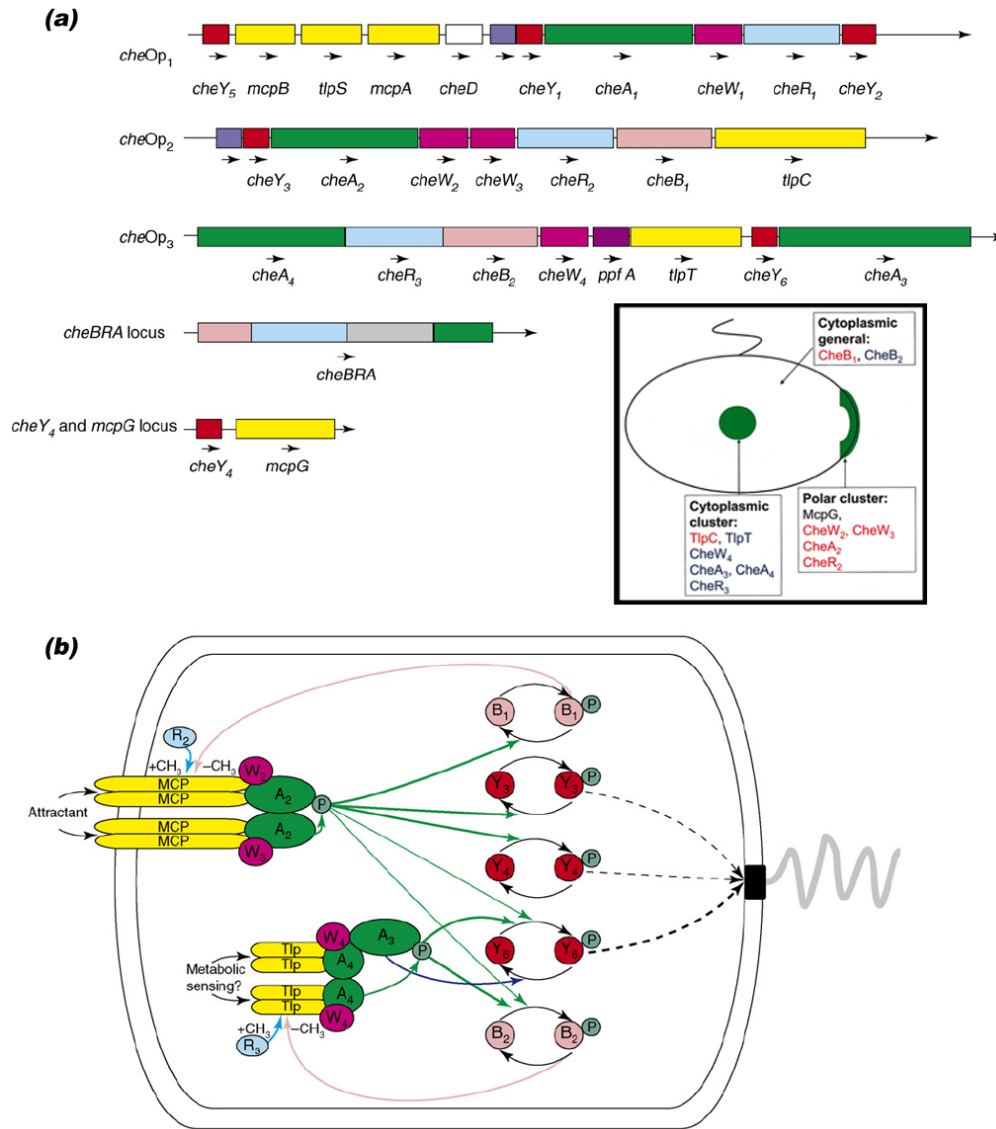


Figure 1.10: Summary of *R. sphaeroides* chemotaxis (figure and caption from [59]). (a) Genetic organisation of chemotaxis genes. In addition to the chemoreceptors shown (yellow), there are seven more at unlinked loci in the genome. Tlp (transducer-like protein) refers to an MCP that lacks transmembrane regions. Despite deleting numerous receptors it has not been possible to ascertain which receptors respond to which stimulus. Inset shows sub-cellular localisation of Che proteins. (b) Working model of the fla1 chemotaxis signal-transduction pathway. Only the proteins that are required for chemotaxis are shown. There are two clusters of chemosensory proteins: one at the cell poles, comprising transmembrane chemoreceptors (MCPs) and associated signalling proteins from *cheOp2*, and one in the cytoplasm, comprising the cytoplasmic chemoreceptors (Tlp) and associated signalling proteins from *cheOp3*. Attractants are thought to be sensed by the polar chemotaxis cluster, and signals reflecting the metabolic state of the cell are believed to be sensed by the cytoplasmic chemotaxis cluster. Phosphotransfer from CheA₂ to CheY₆ and CheB₂ is slow *in vitro* (illustrated using thin arrows). The differential targeting of polar and cytoplasmic chemoreceptors by CheB₁ and CheB₂, respectively, is hypothetical.

or CheY₄) are required for wild-type taxis [62]. CheY₃ and CheY₄ share 75 % sequence identity and give the same phenotypes following mutagenesis, thus *cheY₄* and *cheY₃* most likely arose via a gene duplication event/events. *cheY₃* is nestled in *cheOp₂* on the large chromosome (CI) whilst *cheY₄* is located with only one other *che* gene (*mcpG*) on CII. Table 1.2 shows that CheY₅ also shares a high sequence identity with CheY₃ and CheY₄ (69–75 %). CheY₁ shares ~50 % sequence identity with the CheY₃₄₅ group, whilst CheY₂ and CheY₆ share only ~30 % sequence identity with other CheYs. Figure 1.11 shows a sequence alignment of chemotaxis response regulators from *E. coli* and *R. sphaeroides*.

	CheY ₁	CheY ₂	CheY ₃	CheY ₄	CheY ₅	CheY ₆	CheYec
CheY ₁		30	49	49	50	32	39
CheY ₂	30		30	27	26	30	34
CheY ₃	49	30		75	69	33	33
CheY ₄	49	27	75		74	36	32
CheY ₅	50	26	69	74		30	32
CheY ₆	32	30	33	36	30		32
CheYec	39	34	33	32	32	32	

Table 1.2: CheY sequence identity, reproduced from [63]. Values indicate percentage identities between the proteins along their entire length. CheYec, referring to *E. coli* CheY, is provided for comparison.

The phenotypes of several mutations made in CheY₃, CheY₄ and CheY₆ have been elucidated [62]. Mutating the conserved phosphorylation site to alanine renders these proteins non-functional, just like in *E. coli*. However, an asparagine mutant of the phosphorylation site of CheY₆ (CheY₆(D56N)) permanently stops the flagellar motor (with or without other CheYs present), rendering it completely non-motile. Mass spectrometry revealed CheY₆(D56N) is stably phosphorylated at an alternative site, Ser-83. The equivalent mutations in CheY₃ or CheY₄ reduce wild-type taxis but have no identifiable effect on the stopping frequency.

CheY₆ can be phosphorylated *in vitro* by the CheAs of both polar and cytoplasmic clusters, whereas CheY₃ and CheY₄ are only phosphorylated by CheA₂ of the polar cluster [66]. Figure 1.12 shows that the N-terminus of the fla1 FliM (FliM₁) (containing the putative CheY-binding site) contains some highly conserved residues among the first 50 amino acids. *In vitro* binding studies have shown that CheYs_{1–6} can bind to FliM₁ and that this binding is enhanced by phosphorylation ~3-fold [67]. However, the effect on flagellar rotation of FliM₁ binding the different CheYs is unknown.

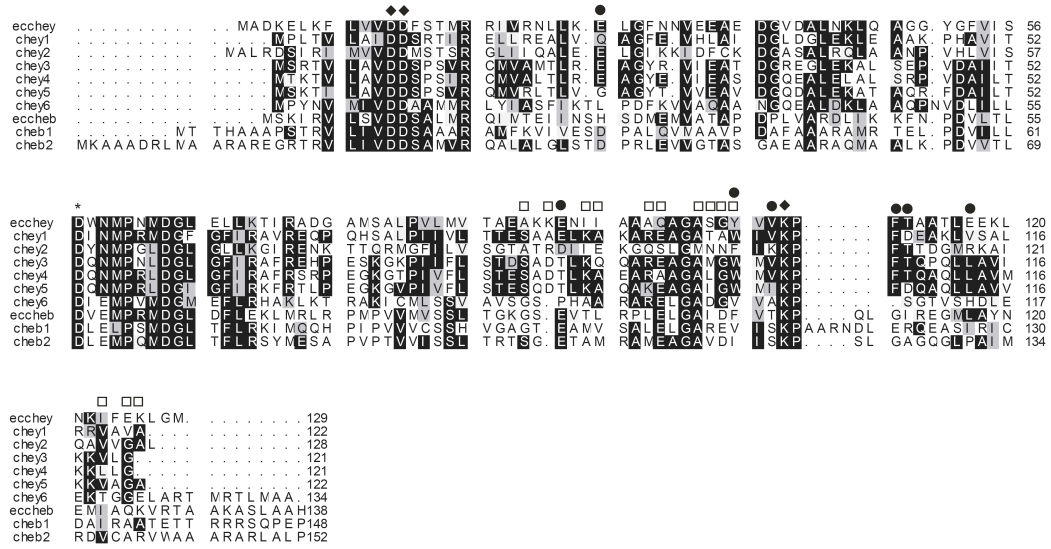


Figure 1.11: Alignment of chemotaxis response regulators from *E. coli* and *R. sphaeroides* (alignment and caption from [63]). Only the N-terminal regulatory domain of the CheBs is shown. The conserved aspartate (D12, D13 and D57 in *E. coli* CheY) and lysine (K109 in *E. coli* CheY) residues are found in all response regulators. * indicates the phosphorylation site on each protein. Black-filled-diamonds indicate the conserved aspartate and lysine residues in the response regulators. White-filled-squares indicate the residues of *E. coli* CheY that interact with *E. coli* CheA [64]. Black-filled-circles indicate the residues of *E. coli* CheY that interact with FliM [65].

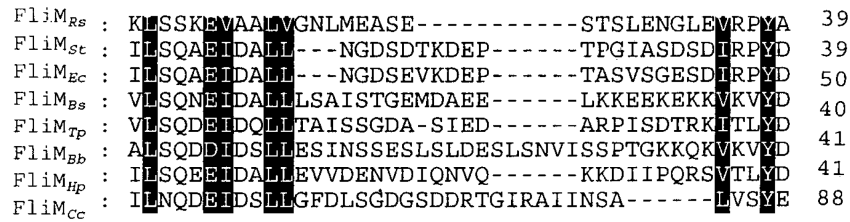


Figure 1.12: Alignment of the N-terminus of FliM₁ (residues 7–39) from *R. sphaeroides* with FliM sequences from other bacterial species (taken from [68]). FliM_{Ec} [*E. coli*], FliM_{St} [*S. enterica*], FliM_{Bb} [*Borrelia burgdorferi*], FliM_{Tp} [*Treponema pallidum*], FliM_{Bs} [*Bacillus subtilis*], FliM_{Hp} [*Helicobacter pylori*], FliM_{Cc} [*Caulobacter crescentus*].

Clearly if a CheY₆ point mutant can stop the motor it is likely that activated wild-type CheY₆ can too, but it is not known if this is the case for CheY₃ or CheY₄. Since the N-terminus of FliM (containing the putative CheY-P binding site) is required for torque-generation in *R. sphaeroides*, it has been suggested that the binding of certain CheYs promote rotation; thus the motor stops when CheYs are not bound to the motor [69]. This sounds less implausible when one considers that CheY-P binding is required to make *B. subtilis* cells run [70].

Another possibility is that some CheYs are unable to stop flagellar rotation and, instead, compete for FliM binding with CheYs that can stop flagellar rotation. This competition might have a key role in integrating the signals from both sensory clusters.

Alternatively, some CheYs may act as ‘phosphate sinks’ as is proposed for CheY₁ in *Sinorhizobium meliloti* [71].⁵ Both response regulators are phosphorylated by the same kinase. Dephosphorylation of the target response regulator by the phosphate sink proceeds via reversed phosphotransfer from the target response regulator to the kinase and from there onto the phosphate sink.

CHEY CONTROL OF fla2

Dreyfus *et al.* showed that the CheYs encoded in *cheOp*₁ (CheY₁, CheY₂, CheY₅) are all required for control of the fla2 flagella, whilst CheY₃, CheY₄, and CheY₆ are not [72]. All of these CheYs can be phosphorylated by one or more of the CheAs encoded by *cheOp*₂ and *cheOp*₃ *in vitro* [66]. The potential for cross-talk between these chemotaxis pathways illustrates the complexity of chemotaxis in *R. sphaeroides* and the difficulty of unravelling how it works.

1.4 EXPERIMENTAL TECHNIQUES REVIEW

There are a number of ways one can investigate the chemotaxis pathway and the motor. Each method has their own merits and drawbacks, highlighted below.

1.4.1 TAXIS ASSAYS

The swim-plate, flow cell and photoresponse assays permit the behaviour of wild-type and *che* mutant strains to be probed.

⁵Porter *et al.* defines a phosphate sink as ‘a response regulator that aids the dephosphorylation of another response regulator’ [59].

SWIM-PLATE ASSAY

In the swim-plate assay⁶ (best described in [73]), bacteria are inoculated as spots of culture onto a Petri dish containing semi-solid nutrient agar and a low concentration of chemoattractant. The agar concentration (0.2 % to 0.35 %) allows bacteria to swim but is not so dilute that currents in the media disperse them evenly.

The plate is typically left at 30 °C allowing the bacteria to grow. During growth, the cells metabolise the chemoattractant resulting in a cell density dependent concentration gradient. Chemotactic cells can respond to this gradient, biasing their swimming behaviour so as to migrate away from the site of inoculation where the chemoattractant concentration is lowest. After 12–48 h growth the area of bacteria is visible by eye and can be measured with a ruler.

Besides its simplicity and its robustness, the advantages of this technique is that conceptually it mimicks what might occur in the wild. However, the drawback is that this relies on other cellular processes (e.g. metabolism and growth) as well as chemotaxis.

FLOW CELL ASSAY

Rather than evaluating the collective behaviour of a population of bacteria as in swim-plates, the flow cell assay enables the chemotactic ability of strains to be assessed by recording the behaviour of single cells whilst exposing them to different concentrations of chemoeffector. Cells are tethered by their flagella to the coverslip via antibodies. Cell body rotation is monitored using a microscope. The specially designed microscope slide is connected to a reservoir intake and a waste beaker via thin (0.5 mm) tubes. Chemotactic cells should swim more when attractant concentration is reduced and *vice versa*. In order to detect obvious chemotactic responses, chemoeffector concentration is typically varied from a base of 0 mM to a maximum of 0.1 or 1 mM in under a second.

This is a very artificial test, since free-swimming cells will never encounter such a gradient; *R. sphaeroides* cells typically take over 60 s to adapt to their pre-stimulus behaviour. An additional limitation arises because it is hard to know when the cells first sense the stimulus making the measurement of meaningful reaction times impossible. Both these problems can be circumnavigated by using the photoresponse assay.

⁶Note that swim-plates used to be called ‘swarm plates’. The swarm plate assay is identical to the swim-plate assay apart from the cells must swarm over the top of denser nutrient agar rather than swim through it.

PHOTORESPONSE ASSAY

Simple, reliable and permits the response of single cells to be recorded whilst sub-saturating stimuli are delivered at the speed of light. The only drawback is that only certain bacterial species are photoresponsive. Conveniently, *R. sphaeroides* is one of them.

Cells are again tethered by their flagella to the coverslip and cell body rotation is monitored with a microscope. Cells respond to changes in light intensity. Figure 1.13 illustrates how *R. sphaeroides* responds to a brief (0.21 s) removal of light. Motor bias (fraction of time spent rotating) decreases following the removal of light and then gradually returns to its pre-stimulus bias over the next few seconds as it adapts [74]. Next we deal with how motor output can be measured.

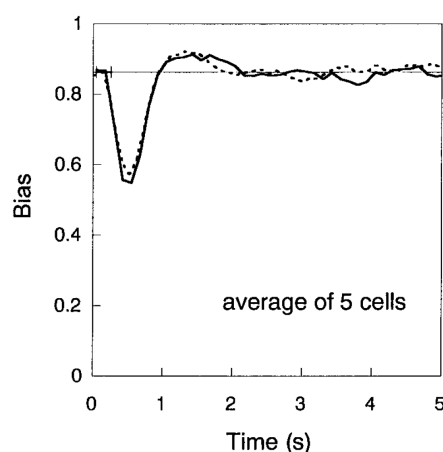


Figure 1.13: The average impulse response of 5 different cells (solid line) in response to the brief removal of light (for 0.21 s, the interval marked by the small vertical bars). The horizontal line represents the cell's resting bias. The dotted line shows the impulse response predicted by computer simulation. Taken from [74].

1.4.2 AN INTRODUCTION TO ROTATION RATE MEASUREMENTS

How does one accurately record the output of a nano-scaled molecular machine which in nature rotates in excess of 100 Hz? Only two techniques actually attempt to measure the rotation of the filament directly [75, 76]. Most techniques rely on observing the rotation of a 'marker', either a polystyrene bead or the cell body itself, which is large enough to track and tends to decrease the speed of rotation. Typically a video camera or a quadrant photodiode is used to detect the marker.

It is important to stress that the behaviour of the motor is only accessible by observing the behaviour of the marker. Events occurring at the motor will not be instantaneously transmitted to the marker; there will always be a delay. This delay (the response time) is due to the compliance of the components that connect the marker to the motor. The larger the drag coefficient or the more compliant the connector, the greater the delay.

TETHERED CELLS

Cells are stuck by their flagella via an anti-filament antibody to a glass coverslip, causing the cell body to rotate about its motor (Figure 1.14(a)). This is analogous to watching a ship's hull rotate about its propeller. Since the drag coefficient of the cell body is significantly larger than that of the filament, the rotation rates observed are considerably lower than the rotation rates of filaments in free-swimming cells. In addition, it has been observed in *S. enterica* that cells often gyrate around the centre spot leading to interaction with the glass surface [77].

BEADS ON FLAGELLAR STUBS

Studying the motor at more physiologically relevant speeds has become possible thanks to the pioneering work of Ryu *et al.* [27] who were the first to attach small (from 40–2000 nm diameter) polystyrene beads to truncated flagellar stubs (Figure 1.14(b)). The viscous drag coefficient of a 300 nm diameter bead on a truncated filament is approximately equal to that of a flagellar filament in a free-swimming cell.

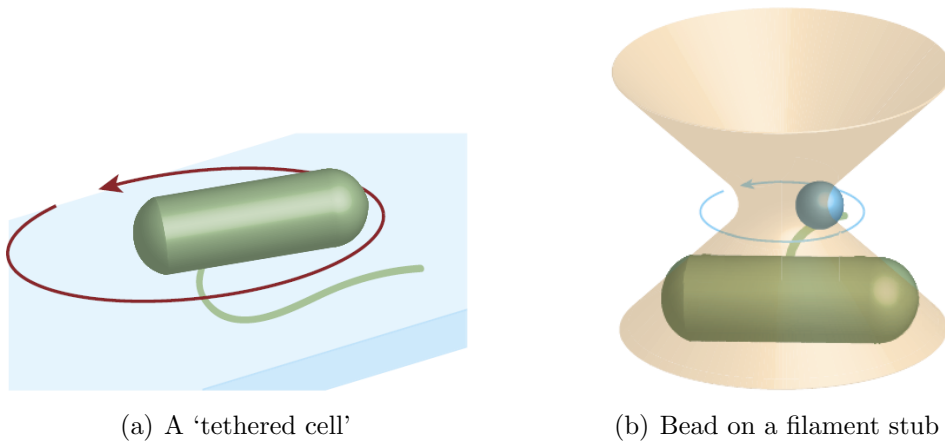


Figure 1.14: Two assays for measuring motor rotation rates (taken from [78]). Cells (green) are $\sim 2 \mu\text{m}$ long. (a) Tethered cell assay - the cell body rotates about its fixed flagellum. (b) Bead assay - a small polystyrene bead is attached to a flagellar stub from a cell which is stuck down to the coverslip by polylysine. Filaments are truncated by passing cells through a narrow tube between hand-held syringes. For *E. coli* the bead spontaneously binds to a mutated filament protein, $\text{FliC}^{\text{sticky}}$ [79], whereas in *R. sphaeroides* we had to develop a protocol using antibodies. Bead rotation is detected using a focussed laser beam (depicted by the dumbbell).

IMAGE DETECTION WITH A VIDEO CAMERA

Before this study, *R. sphaeroides* motor rotation had only been studied by recording *tethered cells* with a *video camera* [80, 81] (bar one exception which used a quadrant photodiode [74]). This procedure which is still being used today is outlined below.

A phase-contrast image of tethered cells is recorded to VHS tape at a sampling rate of 50 Hz. After recording, the fields from the VHS tape are read by custom software on the Hobson Bactracker computer. Regions of interest are specified for each cell and a program (Arot7) calculates the position of the cell each frame giving a notoriously noisy speed-time output. Points are typically filtered (moving average) and then combined with data from other cells to give a speed-time plot for the population (see Figure 1.15).

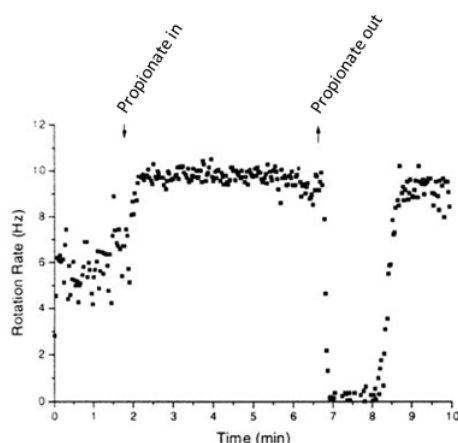


Figure 1.15: Example of the traditional way of assessing the chemotactic ability of a *R. sphaeroides* strain. A population of aerobically grown wild-type cells are shown. Speed-time traces from several cells are pooled. The increase in rotation speed upon addition of propionate is striking. After propionate is removed cells stop for ~ 1 min. Taken from [82].

This method has been used to infer properties of the *R. sphaeroides* motor [83, 84, 80, 81, 85], which have tended to neglect the shortcomings of the method. Many of these problems (outlined in Chapter 3) can be circumnavigated by using a quadrant photodiode to detect rather than a camera.

IMAGE DETECTION WITH A QUADRANT PHOTODIODE

The advantage of using a quadrant photodiode is simple - it is a cheap way of increasing the rate at which one can sample a rotating object. A quadrant photodiode detects photons and outputs current at a very fast rate. The photodiode is split into four separate quadrants that together make up a circle (Figure 1.16(a)). The output current from each quadrant is converted to a voltage which is proportional to the intensity of the light hitting the diode. The amplified voltage signals (V_a , V_b , V_c and V_d) are then processed into P_x and P_y (referring to the position of the bead/cell body in x and y); $P_x = \frac{(V_b+V_d)-(V_a+V_c)}{V_a+V_b+V_c+V_d}$ and $P_y = \frac{(V_a+V_b)-(V_c+V_d)}{V_a+V_b+V_c+V_d}$.

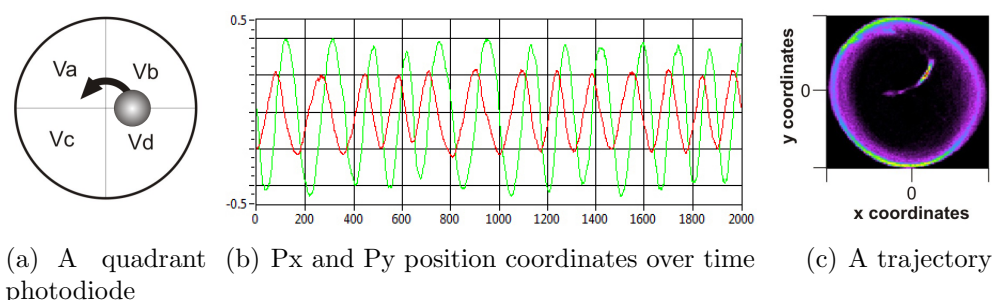


Figure 1.16: The output voltages from the four quadrants (V_a , V_b , V_c and V_d), which vary according to the position of the bead/cell body, are saved during experiments at a certain sampling rate. They are then used to calculate x and y position coordinates (P_x (red) and P_y (green) respectively) to give a trajectory.

In the simplest configuration, an image of a tethered cell is projected onto the face of the quadrant photodiode. Berry and Armitage used this technique to record tethered cells at 128 Hz sampling rate using a light microscope [74]. The large response time of tethered cells makes it pointless to sample at a higher rate. Using the bead assay in conjunction with back-focal-plane (BFP) interferometry permits the use of higher sampling rates (e.g. 10 kHz).

1.4.3 BACK-FOCAL-PLANE INTERFEROMETRY

Since 2000, accurate detection of the position of a sub-micron bead attached to a flagellar stub using BFP interferometry has become routine [27]. BFP interferometry is achieved using a laser focused by an objective lens in the image plane. The stage is moved so that the bead to be detected is located near the focus. The bead interferes with the light from the laser. When this light interacts with the light that was unperturbed by the bead, an *interference pattern* is created in the BFP of the condenser. The light is then collected by a condenser lens and the BFP of the condenser⁷ is imaged onto a quadrant photodiode, enabling the light intensity differences created via interference to be detected. At the BFP one detects the interference pattern created by a refractive bead near the focus of the laser [86].

For simplicity, the practicalities of performing BFP interferometry are described with specific reference to the apparatus/methods used in this study, starting with Figure 1.17 which shows a stripped-down version of the setup. As well as being

⁷The BFP of the condenser is a plane at the back of the condenser lens where the rays that enter the system parallel to the optical axis are focused.

able to detect the position of beads via BFP interferometry using low laser powers (below $\sim 50 \mu\text{W}$), this microscope can also optically trap particles (Section 1.4.4) using higher laser powers ($\sim 100 \text{ mW}$). It is also fitted with an iris to change the size of the focus of the laser in the image plane to change the range in which one is detecting, so that the rotation of different bead sizes can be measured.

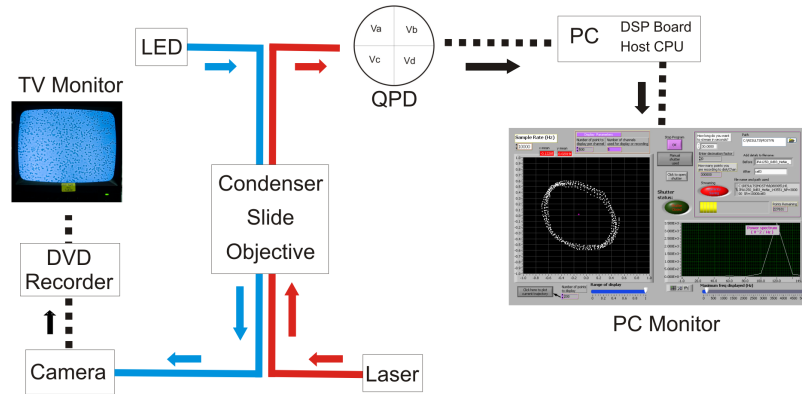


Figure 1.17: Outline of the detection system used in this thesis. A light-emitting diode (LED) is used for sample illumination. A camera and monitor enable the user to find spinning beads and align it with a crosshair which marks where the laser is. The interference pattern is detected by the quadrant photodiode. The voltages from the four quadrants are sampled by the digital signalling processing (DSP) board at a user defined rate. The analogue signal is converted into a digital format by the DSP board and saved to the hard-drive of a PC. Data is then converted into text files (four voltages in rows) after the experiment is complete and transferred to another PC for analysis.

CHOICE OF LASER WAVELENGTH

Focussing a laser onto biological samples inevitably results in photodamage. This can be circumnavigated by using lasers which emit light at infra-red wavelengths (e.g. 1064 nm), resulting in very low levels of photodamage [87]. Alternatively if shorter wavelengths (such as 632 nm) are required (which give a better resolution and permit the detection of smaller particles), experiments must be conducted on short time-scales (e.g. $< 60 \text{ s}$).⁸

THE SIGNAL

As described above, the interference pattern (created when light that interferes with the bead interacts with the light that was unperturbed by the bead) is detected by

⁸As a general rule it is only possible to detect/trap particles that have a diameter which is at least half the laser's wavelength.

the quadrant photodiode. As shown in Figure 1.16 it is possible to convert the voltages from the four quadrants to calculate where the bead is in terms of x and y position coordinates. During experiments a program performs this calculation and displays a representation of the bead's location on an xy grid on the PC monitor in real-time (Figure 1.17).

SIGNAL DETECTION AND PROCESSING

Currents from each of the four quadrants of the quadrant photodiode are amplified using a home-made current to voltage amplifier and sampled at up to 10 kHz by a DSP board (Figure 1.17). Only the output voltages of the four quadrants of the quadrant photodiode are saved. Given the volume of data that is recorded, it is not possible to record continuously, resulting in small (e.g. 1–2 s) gaps inbetween files.⁹

DATA ANALYSIS

Data are then typically analysed using the ‘power-spectrum’ or ‘ $d\theta/dt$ ’ method (θ being angle). The power-spectrum method (Figure 1.18) is much quicker to run and it is easier to store/manipulate the smaller files. The $d\theta/dt$ method (Figure 1.19) takes longer to run and cells with bad trajectories must be discarded (assessed by eye), but it provides much more information, namely the angle the bead is held at over time. Angle-time may be of interest in its own right or used to plot angular velocity ($d\theta/dt$, see Section 2.3.4).

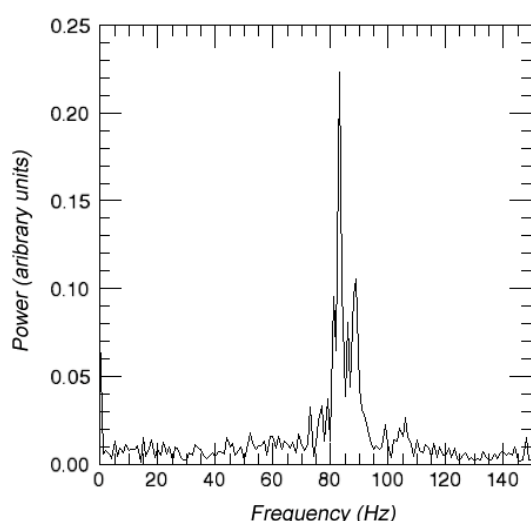


Figure 1.18: Power spectrum from 1 s of data from a $0.83 \mu\text{m}$ bead on a *R. sphaeroides* filament (Figure made by Dr C-J Lo). Data for P_x and P_y are combined to form a complex signal (see Section 1.3.4 of [78] for full details). The peak in the power-spectrum of the complex signal corresponds to the bead's direction of rotation and speed (Hz) for that period of time (the block length). The user specifies the block length and the time increment (dt) to take the next peak for that window. By working its way through the xy coordinates the program creates a speed-time trace for the duration of the recording.

⁹One can record continuously for longer by reducing the sampling rate. With the setup used in this study a maximum of 300,000 points were taken per file (e.g. 30 s at 10 kHz).

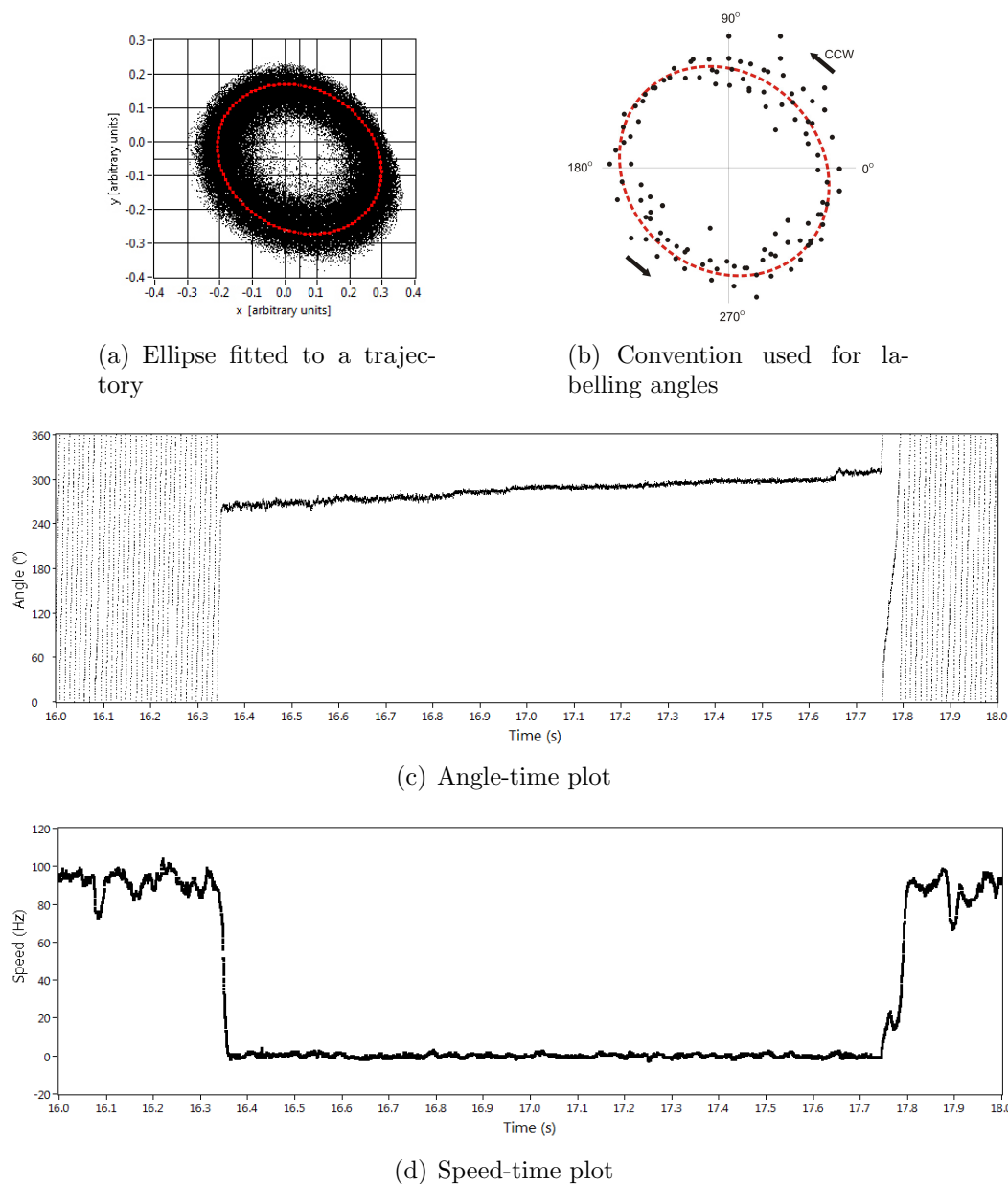


Figure 1.19: Analysis using the $d\theta/dt$ method. An ellipse is fitted to the bead trajectory (black dots). The angle (looking directly from above) for each point is calculated by inferring where the bead intercepts the ellipse. Angular velocity (ω) was calculated from angle versus time traces ($\omega = d\theta/dt$).

1.4.4 OPTICAL TRAPPING

Optical traps (often referred to as ‘optical tweezers’) are widely known for their ability to manipulate microscopic samples. The picoNewton and nanometer ranges of force and distance accessible to optical traps have permitted the measurement of forces that maintain nucleic acid, protein and cellular architectures, and the forces generated by molecular machines (reviewed in [88]).

An optical trap relies on using a sharply focussed laser beam to hold a small dielectric particle (e.g. a bead or cell body) at a fixed position in three dimensions. Particles close to the focus, with a refractive index greater than their surroundings are drawn into a ‘potential well’ close to the focal point. High laser powers (~ 100 mW) are used trap and manipulate samples. Trapped particles can be moved by external manipulation of the laser beam. For instance, one can pick up a cell, move it several microns to the left and then drop it by shuttering the laser.¹⁰ The trap’s stiffness (κ) determines how easy it is for the particle to escape the well [89]. Increasing the power of the laser increases κ . Where distances moved are small (e.g. < 500 nm for the trap used in this study), force (F) and distance moved (D) form a simple linear relationship ($F = \kappa \cdot D$).

Figure 1.20 provides a basic overview of how a focussed laser beam creates this ‘potential well’ based on ray optics (see [90], a review with a more sophisticated and intelligible explanation). It is the combined effect of two forces (gradient and scattering forces) that constitute the optical trap. The scattering force arises from the photons striking the particle along their propagation direction, pushing the particle along the incident beam. Gradient forces are generated by the beam interacting with the dielectric particle and it is dependent on the intensity gradient of the beam, pulling the particle towards the direction of increasing intensity. A steep intensity gradient is achieved by sharply focusing the laser with an objective of high numerical aperture. This counteracts the effects of the scattering force so that the particle is pulled towards the focal point (settling slightly above the focal point in z).

Many of these techniques were used along with biochemical and behavioural assays to fulfil the aims of this project.

¹⁰By using a computer to control multiple lasers you can perform sophisticated tasks... like play Tetris (see the video at <http://tiny.cc/TrapTetris>).

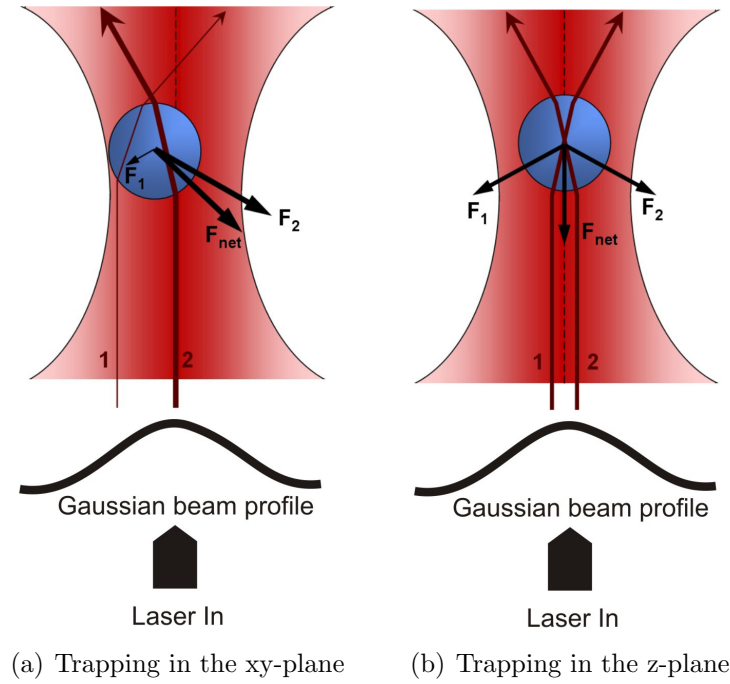


Figure 1.20: Schematics showing the principle of optical trapping using ray optics. A bead is illuminated by a Gaussian profiled laser beam. The representative laser paths are shown as red lines with arrows indicating the direction of beam propagation. The thickness of the red lines indicates the intensity of laser beam. (a) The gradient forces (black lines) are generated by the refraction of the beam when they interact with the particle, resulting in a change of photon momentum which is transferred on to the particle, thus generating the forces F_1 and F_2 . As more photons follow path 2 than 1 (because the beam intensity is higher along the former), force F_2 is stronger than F_1 . Consequently, the net gradient force (F_{net}) in the lateral direction directs the particle to centre of the beam, keeping it trapped in the same position in x and y . (b) To achieve a three-dimensional trap, the scattering force needs to be compensated as well. This is achieved by sharply focussing the laser thus generating an axial gradient force towards this region when the particle is in its vicinity. The scattering force (not shown) is in the direction of propagation of the laser beam (i.e. upward in this figure) and is proportional to the intensity of the beam. The bead is trapped slightly beyond the focused spot where the gradient force and scattering force are in equilibrium in the z -plane.

1.5 AIMS OF THIS PROJECT

Whilst experimental objectives are discussed at the start of each results chapter, here is a summary of questions this project was designed to answer:

- Recording tethered cells with a video camera is unsatisfactory - how can we improve the resolution of stop events and reliably record motor speed?
- Having developed the bead assay for *R. sphaeroides*, what can we learn about the motor e.g. is it equivalent to *E. coli* in terms of torque/speed?
- What is the ‘default’ state of the motor i.e. without chemotactic stimulation does it continually rotate or is it permanently stopped?
- Can the chemotaxis system regulate motor speed as well as controlling stop events?
- Do the multiple CheYs present in *R. sphaeroides* all do the same job - can we use this information to piece together a model for how the two chemotaxis pathways interact in this species?
- How does the chemotaxis system stop the motor - does it lock the motor in a particular configuration (a brake) or cause a loss in transmission of torque (a clutch)?

1.6 RAW DATA AND PROTOCOLS AVAILABLE ONLINE

In addition to my experimental aims, measures have been taken to make the experiments presented in this thesis as accessible as possible. The information used to construct this thesis has been deposited on a website¹¹ (Digital Appendix - Appendix D) and in a CD at the back of the original copy. It contains much of my raw data, protocols, analysis programs and all the files used to compile this document.

¹¹<http://databank.ouls.ox.ac.uk/objects/dataset:3.html>

MATERIALS AND METHODS

The details of how experiments were performed are described below. See Appendix D (Digital Appendix) for step by step protocols.

2.1 MOLECULAR MICROBIOLOGY

2.1.1 GENERAL GROWTH CONDITIONS

The strains and plasmids used in this study are shown in Tables 2.1 and 2.2 respectively.

E. coli strains were grown at 37 °C, either in Luria-Bertani (LB) medium (Appendix A) with shaking, or on 1.5 % LB agar plates.

R. sphaeroides strains were grown in succinate medium (Appendix A) either aerobically with shaking in the dark at 30 °C, or anaerobically (25 ml universals) in the light (c. 40 $\mu\text{mol.m}^{-2}.\text{s}^{-1}$). For swim-plate inoculation and molecular genetic techniques (such as genomic DNA extraction), *R. sphaeroides* was grown overnight in 1.5 ml succinate medium in 1.7 ml Eppendorfs and exposed to the same light source as for universals. *R. sphaeroides* was also grown on 1.5 % LB agar plates at 30 °C. Details of how cells were grown for each experiment are provided in this chapter in the sections to follow.

Antibiotics were used at 100 $\mu\text{g/ml}$ for ampicillin, 25 $\mu\text{g/ml}$ for kanamycin and nalidixic acid.

Strain	Description	Source
XL-1 Blue	General <i>E. coli</i> cloning strain. <i>lacI^q</i> , Tc ^R	Stratagene
M15pREP4	<i>E. coli</i> expression host containing pREP4. Kn ^R	Qiagen
S17-1λ-pir	<i>E. coli</i> strain capable of mobilizing the suicide vector pK18 <i>mobsacB</i> into <i>R. sphaeroides</i> . Sm ^R .	[91]
WS8N	Spontaneous nalidixic acid resistant mutant of wild-type WS8	[92]
JPA410	WS8N derivative that carries a <i>cheY</i> ₃ gene that has been insertionally inactivated (named <i>cheY</i> ₃ [*]) [†]	[82]
JPA421	Δ <i>cheY</i> ₄ derivative of WS8N	[82]
JPA425	<i>cheY</i> ₃ [*] , Δ <i>cheY</i> ₄ derivative of WS8N	[82]
JPA1025	Δ <i>cheY</i> ₁ Δ <i>cheY</i> ₂ Δ <i>cheY</i> ₃ Δ <i>cheY</i> ₄ Δ <i>cheY</i> ₅ derivative of WS8N	[62]
JPA1337	Δ <i>cheY</i> ₁ Δ <i>cheY</i> ₂ Δ <i>cheY</i> ₃ Δ <i>cheY</i> ₄ Δ <i>cheY</i> ₅ Δ <i>cheY</i> ₆ derivative of WS8N	[62]
JPA443	Δ <i>cheOp</i> ₁ and Δ <i>cheY</i> ₅ derivative of WS8N	S.L. Porter
JPA1349	Δ <i>cheBRA</i> , ΔRSP2230 derivative of WS8N	S.L. Porter
JPA1278	Δ <i>fliM</i> ₂ (RSP6099) derivative of WS8N	S.L. Porter
<i>fliM</i> ₁ (E12D)	<i>fliM</i> ₁ (E12D) derivative of WS8N*	R.E. Sockett
<i>fliM</i> ₁ (E12Q)	<i>fliM</i> ₁ (E12Q) derivative of WS8N*	R.E. Sockett
<i>fliM</i> ₁ (S9F)	<i>fliM</i> ₁ (S9F) derivative of WS8N*	R.E. Sockett
JPA419	Δ <i>cheOp</i> ₂ and Δ <i>cheY</i> ₄ derivative of WS8N	[82]
JPA1301	Δ <i>cheOp</i> ₃ derivative of WS8N	[61]
JPA1336	Δ <i>cheY</i> ₆ derivative of WS8N	[61]
JPA1314	Δ <i>cheA</i> ₃ derivative of WS8N	[61]
JPA1353	Δ <i>cheOp</i> ₁ (<i>cheY</i> ₅ , <i>cheD</i> , <i>cheP</i> ₁ , <i>cheY</i> ₁ , <i>cheA</i> ₁ , <i>cheW</i> ₁ , <i>cheR</i> ₁ , <i>cheY</i> ₂), Δ <i>cheOp</i> ₂ (<i>cheP</i> ₂ , <i>cheY</i> ₃ , <i>cheA</i> ₂ , <i>cheW</i> ₂ , <i>cheW</i> ₃ , <i>cheR</i> ₂ , <i>cheB</i> ₁ , <i>tlpC</i>), Δ <i>cheOp</i> ₃ (<i>cheA</i> ₄ , <i>cheR</i> ₃ , <i>cheB</i> ₂ , <i>cheW</i> ₄ , <i>ppfA</i> , <i>tlpT</i> , <i>cheY</i> ₆ , <i>cheA</i> ₃), Δ <i>cheBRA</i> , Δ <i>cheY</i> ₄	S.L. Porter

Continued...

Strain	Description	Source
JPA1319	$\Delta cheA_2$, $\Delta cheA_3$ derivative of WS8N	S.L. Porter
JPA1213	<i>cheY</i> ₆ (D56N) derivative of WS8N	[62]
JPA1216	<i>cheY</i> ₆ (D56A) derivative of WS8N	[62]
JPA1218	<i>cheY</i> ₃ (D53N) derivative of WS8N	[62]
JPA1220	<i>cheY</i> ₄ (D53N) derivative of WS8N	[62]
JPA917	<i>cheY</i> ₃ [*] , <i>cheY</i> ₄ (D53A) derivative of WS8N (parental = JPA425)	This study
JPA918	<i>cheY</i> ₃ [*] , <i>cheY</i> ₄ (D53N) derivative of WS8N (parental = JPA425)	This study
JPA919	<i>cheY</i> ₃ (D53A), <i>cheY</i> ₄ (D53A) derivative of WS8N (parental = JPA917)	This study
JPA920	<i>cheY</i> ₃ (D53N), <i>cheY</i> ₄ (D53N) derivative of WS8N (parental = JPA918)	This study

Table 2.1: Strains used in this study. †JPA410 was made by cloning a *Mlu*I linker (5'-GACGCGTC-3') into the *Eco*RV site near the beginning of *cheY*₃, introducing a stop codon at the site of insertion with a new *Mlu*I restriction site, which is expected to produce a truncated peptide of 26 N-terminal amino acids (named CheY₃^{*}) [82]. *For future reference, strains made by R.E. Sockett were assigned JPA numbers so they can be located in the freezers (*fliM*₁(E12D), *fliM*₁(E12Q), *fliM*₁(S9F) = JPA1249, JPA1250, JPA1251 respectively). *lacI*^q denotes the gene encoding the high expression mutant of the *lacI* gene. Tc^R, Kn^R, Sm^R denote tetracycline, kanamycin, streptomycin resistance respectively.

Plasmid	Description	Source
pUC19	High copy number cloning vector. Ap ^R	Pharmacia
pREP4	Plasmid carrying the <i>lacI</i> gene.	Qiagen
pIND4	<i>R. sphaeroides</i> inducible expression plasmid†, P _{A1/04/03} , <i>lacI</i> ^q , Kn ^R	[93]
pK18 <i>obsacB</i>	Allelic exchange suicide vector. Kn ^R , Sucrose sensitive	[94]
pK18Y3D53A	Construct for replacing <i>cheY</i> ₃ with <i>cheY</i> ₃ (D53A) in <i>R. sphaeroides</i> genome; pK18 <i>obsacB</i> derivative	[62]
pK18Y3D53N	Construct for replacing <i>cheY</i> ₃ with <i>cheY</i> ₃ (D53N) in <i>R. sphaeroides</i> genome; pK18 <i>obsacB</i> derivative	[62]
pK18Y4D53A	Construct for replacing <i>cheY</i> ₄ with <i>cheY</i> ₄ (D53A) in <i>R. sphaeroides</i> genome; pK18 <i>obsacB</i> derivative	[62]
pK18Y4D53N	Construct for replacing <i>cheY</i> ₄ with <i>cheY</i> ₄ (D53N) in <i>R. sphaeroides</i> genome; pK18 <i>obsacB</i> derivative	[62]
pQEY1	CheY ₁ expression plasmid. pQE30 derivative	[95]
pQEY2	CheY ₂ expression plasmid. pQE30 derivative	[95]
pQEY3	CheY ₃ expression plasmid. pQE30 derivative	[95]
pQEY4	CheY ₄ expression plasmid. pQE30 derivative	[95]
pQEY5	CheY ₅ expression plasmid. pQE30 derivative	[66]
pQEY6	CheY ₆ expression plasmid. pQE30 derivative	[61]
pQEY6D56N	CheY ₆ (D56N) expression plasmid. pQE30 derivative	[62]
pQEYFP-Y6	YFP-CheY ₆ expression plasmid. pQE30 derivative	[62]
pIND-empty	As pIND4 above, i.e. empty vector used as a control	[93]
pIND-Y1	<i>cheY</i> ₁ cloned into pIND4	This study
pIND-Y2	<i>cheY</i> ₂ cloned into pIND4	This study

Continued...

Plasmid	Description	Source
pIND-Y3	<i>cheY</i> ₃ cloned into pIND4	This study
pIND-Y3D53A	<i>cheY</i> ₃ (D53A) cloned into pIND4	This study
pIND-Y3D53N	<i>cheY</i> ₃ (D53N) cloned into pIND4	This study
pIND-Y4	<i>cheY</i> ₄ cloned into pIND4	This study
pIND-Y4D53A	<i>cheY</i> ₄ (D53A) cloned into pIND4	This study
pIND-Y4D53N	<i>cheY</i> ₄ (D53N) cloned into pIND4	This study
pIND-Y5	<i>cheY</i> ₅ cloned into pIND4	This study
pIND-Y6	<i>cheY</i> ₆ cloned into pIND4	This study
pIND-Y6D56A	<i>cheY</i> ₆ (D56A) cloned into pIND4	This study
pIND-Y6D56N	<i>cheY</i> ₆ (D56N) cloned into pIND4	This study
pIND-YFPY6	<i>yfp-cheY</i> ₆ cloned into pIND4	This study
pIND-YFPY6D56A	<i>yfp-cheY</i> ₆ (D56A) cloned into pIND4	This study
pIND-ecY	<i>E. coli cheY</i> cloned into pIND4	This study
pBAD-ecYD13K	<i>E. coli cheY</i> (D13K) expression plasmid. pBAD24 derivative	Y. Sowa
pIND-ecY**	<i>E. coli cheY</i> (D13K, Y106W) cloned into pIND4	This study
pIND-ecYZ	<i>E. coli cheY, cheZ</i> cloned into pIND4	This study
pIND-ecZ	<i>E. coli cheZ</i> cloned into pIND4	This study

Table 2.2: Plasmids used in this study. Kn^R , Ap^R denote ampicillin and kanamycin resistance respectively. $\text{P}_{\text{A1/04/03}}$ denotes an isopropyl -D-1-thiogalactopyranoside (IPTG) inducible promoter. †See Appendix B.1, Page 122 for pIND4 plasmid map.

2.1.2 MOLECULAR GENETIC TECHNIQUES

STANDARD DNA TECHNIQUES

Preparation of Plasmid DNA - Carried out using the QIAprep Spin Miniprep Kit (Qiagen) according to the manufacturer's instructions.

Restriction Digests - Carried out using enzymes from New England Biolabs (NEB); 0.5 μl of each enzyme, 2 μl 10X buffer, 2-4 μl DNA to be digested, made up with sterile water to a total volume of 20 μl .

Gel Electrophoresis - Multi purpose agarose (Roche) was made up at between 0.8

and 2 % in 0.5X TBE buffer (90 mM Tris-borate, 2 mM EDTA, pH 8.0) and electrophoresed at between 100 and 150 V. The gels were stained for 20 mins in 1 ng/ml ethidium bromide and visualised on a UV transilluminator.

Purification of DNA Fragments - DNA fragments were cleaned from agarose gels or from solution using the Genelute Gel Extraction Kit (Sigma) according to the manufacturer's instructions.

Ligations - 2 μ l T4 DNA ligase (NEB) was used in a final volume of 50 μ l with vector and insert DNA in a ratio of about 1:3 and the supplied reaction buffer and incubated at 15 °C for at least 16 hours.

Competent E. coli Cells - Prepared using the calcium chloride method of Sambrook and Russell [96] and stored in 200 μ l aliquots at -80 °C.

Transformation - DNA was transformed by incubation with 200 μ l of the competent cells on ice for 1 hour, followed by 2 min at 42 °C and 2 min on ice. 1 ml of LB was added and incubated at 37 °C for 1 hour. The mixture was spread on LB-agar plates containing appropriate antibiotics.

Polymerase Chain Reaction (PCR) - Reactions consisted of DNA template (~100 ng), 100 pmol of each primer (Sigma-Genosys), 12.5 nmol dNTPs, and 1 unit of *pfu* DNA polymerase (Promega), made up to a final volume of 25 μ l. Thermocycling was performed in a Thermal MiniCycler (MJ Research) as follows:

Step 1	98°C x 5 min
Step 2.1	98°C x 2 min
Step 2.2	55°C x 1.5 min
Step 2.3	72°C x 4 min
Step 3	repeat step 2, 25 times
Step 4	72°C x 5 min

DNA Sequencing - All constructs were sequenced before use by the Automated DNA Sequencing Service (Geneservice, Source BioScience) using BigDyeTM dye terminators (PE Biosystems) on a 3730 DNA sequencer (Applied Biosystems). Sequences were assembled using the Staden Software Package and analysed using Clone Manager Software (Scientific and Educational Software).

DIG Labelling of DNA Probes for Southern Blot - DNA for use as a probe in Southern blots was purified from agarose gels as described previously and labelled using the random hexanucleotide priming technique with the DIG DNA Labelling and Detection Kit (Roche) according to the manufacturer's instructions.

Southern Blotting - DNA for Southern blotting was separated on an agarose gel, depurinated, denatured, neutralised and transferred to Hybond-N membrane (Amersham) by capillary transfer as described in [96]. The membrane was dried, UV fixed, prehybridised for at least 3 hours. Hybridisation of the probe was carried out at 68 °C in a Hybaid oven over night. Detection was performed using the DIG colour detection kit (Roche) according to the manufacturer's instructions.

Conjugation - Plasmids were conjugated into *R. sphaeroides* from the donor strain *E. coli* S17-1 λ -pir. A stationary phase culture of S17-1 containing the appropriate plasmid was diluted 1:30 into fresh medium and grown at 37 °C to an optical density (OD) of OD₆₀₀ ~0.1. 1 ml of the *E. coli* culture and 1 ml of stationary phase *R. sphaeroides* were centrifuged at 4000 g, washed gently in succinate medium and finally resuspended in 100 μ l of succinate medium. 10 μ l of *E. coli* was mixed with 100 μ l of *R. sphaeroides* cells and pipetted onto a 0.45 μ m filter (Whatman) on an LB-agar plate. After overnight incubation at 30 °C the filter was washed with 1 ml of succinate medium and plated on 1.5 % LB-agar plates containing kanamycin.

R. sphaeroides Chromosomal DNA Preparation - 1.5 ml of cells were spun down and frozen in liquid nitrogen. The pellet was resuspended in 0.5 ml of 65 °C lysis buffer (10 mM Tris-HCl pH 8.0, 1 mM EDTA, 1 % SDS) and 0.1 mg proteinase K added. This was incubated at 42 °C for 2 hours and extracted twice with 0.5 ml phenol:chloroform:isoamyl alcohol (25:24:1 v/v). The DNA was precipitated with 100 % ethanol, washed in 70 % ethanol and dried. The pellet was resuspended in 30 μ l of water with RNAase and stored at 4 °C until required.

NON-STANDARD DNA TECHNIQUES

Overlap Extension PCR - Overlap extension PCR (Figure 2.1) was used to make two point mutants generating CheY₆(D56A) and *E. coli* CheY(Y106W) (see Appendix B.2, Page 123 for primer sequences). Primers were designed to amplify regions upstream and downstream of the desired mutation site. Primer B (and its complementary primer C) contained a deliberate mismatch enabling the mutation

to be generated. The PCR conditions were the same as described above except that the two DNA templates were present in the reaction mix.

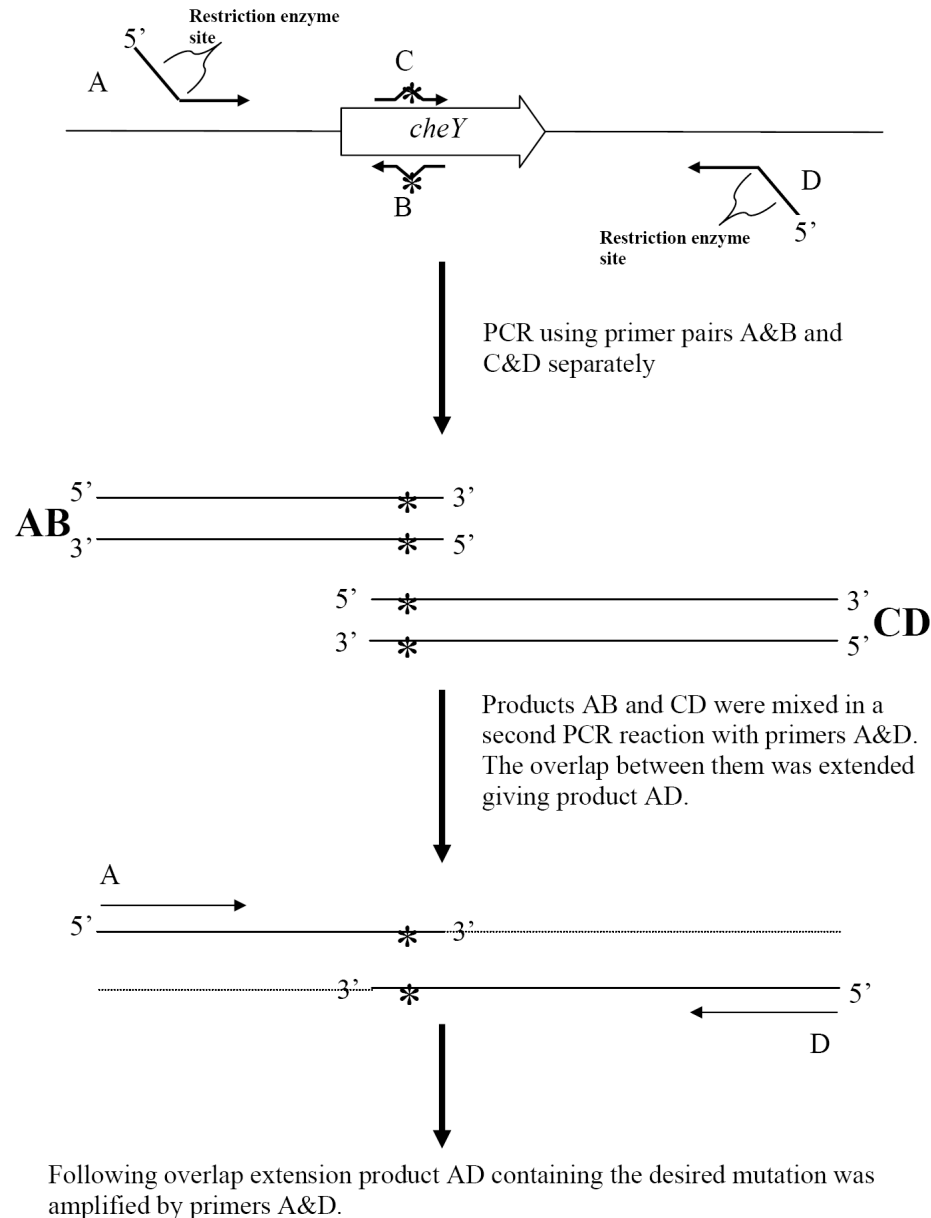


Figure 2.1: Overlap extension PCR to generate CheY point mutants taken from [63] (* indicates the site of mutation).

Cloning of Genes into pIND4 - The coding regions of the genes were amplified by PCR to include exogenous 5' and 3' restriction sites, facilitating in-frame cloning of genes into pIND4 at the *NcoI* site situated downstream of the $P_{A1/04/03}$ IPTG-inducible promoter (see Appendices B.1 and B.2, Pages 122 and 123 for the pIND4 plasmid map and primer sequences respectively). The expression of the

cloned gene is under the control of the IPTG inducible *lac* promoter. Plasmids were introduced into *R. sphaeroides* by conjugation and selected for by growth on 25 $\mu\text{g/ml}$ kanamycin agar plates.

Mutating CheY Genes on the R. sphaeroides Genome - The procedure for introducing mutated genes into the *R. sphaeroides* genome is shown in Figure 2.2. Plasmids (pK18*mobsacB* derivatives) containing the mutated *cheY* genes and upstream and downstream flanking sequences were introduced into the appropriate *R. sphaeroides* strain via conjugation. Since the suicide vector was unable to replicate in *R. sphaeroides*, transconjugants having undergone a single homologous crossover event in either the upstream or downstream flanking regions were selected for by growth on kanamycin. Transconjugants were then grown for two days in the absence of kanamycin to allow a second recombination event to occur, excising the vector DNA. Selection for transconjugants having undergone the second recombination event was achieved by plating the cultures on M22 minimal media containing 10 % sucrose (Fluka) and naladixic acid. Only cells which had excised the vector DNA (and hence do not contain the *sacB* gene which converts sucrose to levansucrose, making it toxic to the cell) will grow on these plates. Sucrose resistant colonies were replica plated to ensure kanamycin sensitivity (and hence the loss of the vector DNA). The DNA from sucrose resistant, kanamycin sensitive colonies was analysed by Southern blotting to determine which colonies contained the desired mutation. Successful transconjugants were then subject to PCR and sequenced to confirm that the *cheY* genes contained the desired mutations.

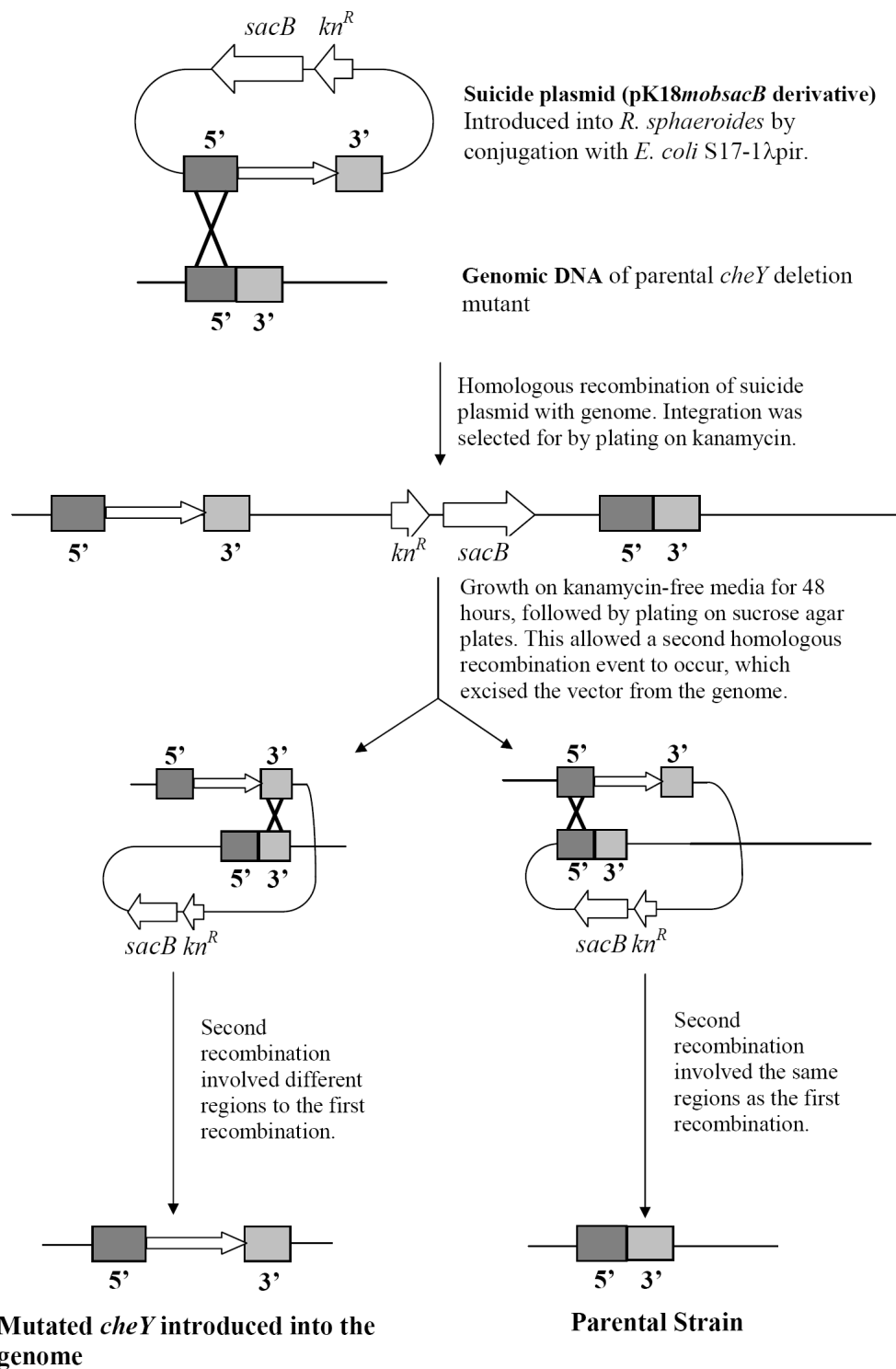


Figure 2.2: The process of introducing the mutant *cheY* genes into the *R. sphaeroides* genome, taken from [63].

2.2 PHENOTYPIC ANALYSIS OF CELL POPULATIONS

2.2.1 CELLULAR PROTEIN QUANTIFICATION

SAMPLE PREPARATION FOR IMMUNOBLOTS

Colonies were grown to stationary phase in Eppendorf tubes with appropriate antibiotics. Three colonies were picked per strain. 50 μl of each stationary culture was used to inoculate 10 ml succinate medium in 125 ml flasks. Cultures were grown micro-aerobically (i.e. flasks had foam caps) with shaking at 30 °C until they reached an OD₇₀₀ of 0.5–0.7 (typically this takes \sim 14 h). 1250 μl of culture, OD₇₀₀ = 0.6 were spun down at 16,000 g for 2 min, resuspended in 125 μl of SDS loading dye (Appendix A) and boiled for 10 min at 95 °C. Volumes above and below OD₇₀₀ = 0.6 (but within the 0.5–0.7 range) were compensated by dilution/concentration i.e. 1250 μl x 0.6 = χ μl to spin down x OD.

PROTEIN STANDARDS FOR IMMUNOBLOTS

HIS-tagged CheY₃, CheY₄ and CheY₆ were purified using Ni-NTA-agarose (Qiagen) and quantified using the Bradford assay (BioRad) as described in [97].

SEMI-QUANTITATIVE WESTERN BLOTS

Samples and purified protein standards of known concentration were electrophoresed in SDS-PAGE gels (15 %). Proteins were then electrophoretically transferred to a nitrocellulose PVDF membrane (Biorad). The membrane was exposed to appropriate primary antibodies, developed with ECLTM Western Blotting Detection Reagents (Amersham Biosciences), and visualised using X-OMAT AR film (Kodak).

QUANTITATIVE IMMUNODOTBLOTS

The quantitative immunodotblot procedure is described in Figure 2.3. A set volume (0.5, 1, 2 or 5 μl) of sample and standard were dotted onto dry nitrocellulose PVDF membrane (Biorad). Three replicates per protein standard produced good standard curves. Samples (including dilutions) were added as many times as possible (typically three times for each sample). Samples were left to dry on a light box for 20-50 min until each spot had completely dried and then left overnight in 5 % powdered milk solution made up in phosphate buffered saline (PBS).

The blots were developed in the same way as western blots described above. Blots were then scanned and analysed using ImageQuant 5.1 software. Mean intensities for each region of interest were calculated and subtracted from the background. A standard curve was constructed enabling sample concentrations to be determined. The slope and intercept of the standard curve was used to calculate sample concentrations, which were then converted to numbers of copies per cell using the following procedure¹:

1. **ng in 1 ml of cells** = $\text{ng}/\mu\text{l} \times 100$ (would be $\times 1000$ but the samples are 10 times concentrated when they are spun down i.e. $1250 \mu\text{l}$ to $125 \mu\text{l}$)
2. **ng per cell** = $\text{ng per 1 ml cells} / \text{number of cells in 1 ml}$ ($= 379.8 \times 10^6$) [98])
3. **moles per cell** = $\text{ng per cell} / \text{Mr (Da)} \times 1 \times 10^9$
4. **molecules per cell** = $\text{moles per cell} \times \text{Avogadro's number}$ (6×10^{23})

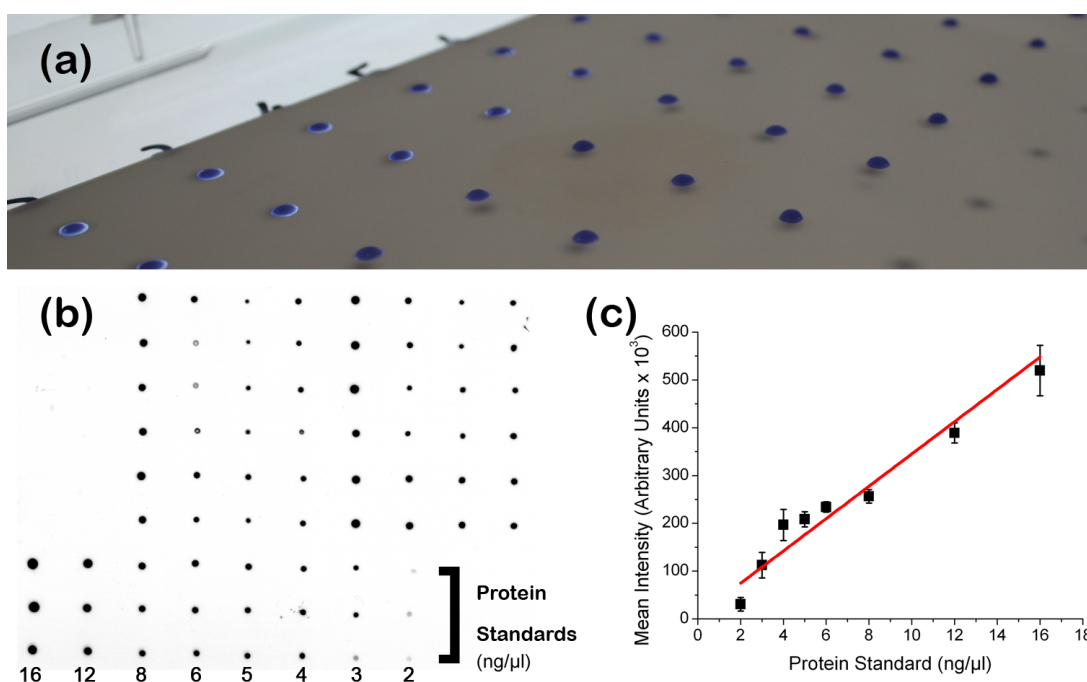


Figure 2.3: Quantitative immunodotblot methodology. (a) A set volume of samples and standards were dotted ~ 2 cm apart (in all directions) onto dry nitrocellulose membrane with a pipette. (b) The blot ($23 \text{ cm} \times 17.5 \text{ cm}$) is developed as for western blots and analysed using ImageQuant 5.1 software. (c) A standard curve was constructed enabling sample concentrations to be determined.

¹See template excel file in Appendix D.3.

2.2.2 LIGHT MICROSCOPY

A phase-contrast microscope (Nikon, 400X magnification) was used to access the stopping frequency of free-swimming and temporarily tethered cells from various strains. Cells were drawn up into optically flat capillary tubes (0.2 x 2 mm, Vitro-com). The capillary ends were left unsealed to allow oxygen to reach the cells; only cells near the end of the capillary tube were assessed. Experiments were conducted blind as described in full below.

The data presented in Figures 4.4, 5.2, and 5.5 (summary in Figure C.1, Page 126) were obtained at the same time to ensure that enough strains were examined for the experiment to be fully blind. Single colonies from the 11 different strains were picked, grown to stationary phase, and used to inoculate a new flask of succinate medium, growing overnight to reach a motile OD by morning. When using pIND4, strains were grown in the presence of kanamycin and 1 mM IPTG. The OD₇₀₀ of each strain was measured, the strain code was noted at the base of the 1 ml cuvettes, and an optically flat capillary tube was placed in each one. The 11 cuvettes were then placed in a random order by another lab member, returning the cuvettes to the polystyrene case that obscured the strain code. The eleven capillaries were carefully placed in order on a microscope slide. The microscope was focussed on the top surface as close to the end of the capillary as possible was used to visualise the swimming behaviour of the cells in each capillary. Their behaviour was marked on a scale of 1 = smoother than WS8N, 2 = indistinguishable from WS8N, 3 = stoppier than WS8N. Each capillary was tested three times (n = 3). This constituted a 'round'. The process was repeated for a total of three rounds (n = 9). The entire process (starting from a new starting colony each time) was repeated a further two days (n = 27). A chi-squared test was then used to find if there a strain was significantly different stop frequency ($P < 0.05$) from the 2:24:1 (smoother:WT:stoppier) ratio of WS8N (df = 2). It is probably slightly easier to tell if a strain is smoother than WS8N, as opposed to telling if it is stoppier than WS8N and thus may represent a small experimental bias.

2.2.3 SWIM-PLATES

Swim-plates were made from M22 minimal media (Appendix A), supplemented with Bitek agar (0.25 % unless otherwise stated) and 100 μ M propionate. Swim-plates using strains with pIND4 required kanamycin and IPTG at appropriate concentrations (final concentrations of 1-50 μ M and 0.1-10 mM IPTG were achieved by

inoculating each 75 ml plate with the appropriate volume from 0.01 and 1 M stocks respectively). Medium was prepared in large flasks (1 or 2 l) ensuring that plates for each run were from the same bottle.

Hand-hot agar (75 ml) was poured into each plate and immediately transferred to the 30 °C room where they were left to set for 2 h. Plates were inoculated with 5 μ l photoheterotrophically grown stationary phase culture. Swarm diameters were measured after 48 h of growth at 30 °C in a micro-aerobic environment (i.e. the room was sufficiently well-ventilated but the lid on top of the plate may have restricted the availability of oxygen). All assays were carried out in triplicate, with each strain being compared to others inoculated on the same plate. Statistical significance between strains were assessed using a one-way ANOVA with Tukey's modification using the SPSS (v16.0) software package.

2.2.4 GROWTH RATES

Aerobic cultures were grown to stationary phase from single colonies and their OD₇₀₀ measured. An appropriate volume of culture (typically \sim 600 μ l) was used to inoculate 10 ml succinate medium (plus kanamycin or IPTG when required) in 125 ml flasks so that the OD₇₀₀ was 0.15 at time zero. The OD₇₀₀ was then measured every 2 h. All assays were carried out in triplicate and statistical analysis was conducted as above using doubling times.

2.3 SINGLE CELL ANALYSIS

FROZEN STOCKS

A universal containing succinate medium was inoculated with a single colony and grown for 3 days photoheterotrophically in the light cabinet. 8 ml of cells were added to 8 ml of succinate medium and 8 ml 50 % glycerol to give a final volume of 24 ml. 300 μ l stocks were aliquoted into 0.5 ml Eppendorfs and stored at -80 °C.

GROWTH

Approximately 100 μ l of frozen stock was used to inoculate 10 ml succinate medium in 125 ml flasks. Cultures were grown micro-aerobically with shaking at 30 °C until they reached an OD of 0.45–0.65 (typically this takes \sim 12 h). Occasionally cultures were grown photoheterotrophically, in sealed universals in the light (c. 40 μ mol.m⁻².s⁻¹).

SLIDE TYPES

Two types of slide were used, a *tunnel slide* or a *flow cell*. The tunnel slide was prepared by bridging a coverslip (22 x 22 mm) over a gap of 2–5 mm between two parallel strips of double-sided sticky tape. Flow cells were similar in design; a single strip of double-sided sticky tape was placed down the axis of the slide that had two holes drilled in it at either end. A channel was formed by cutting out a section in the strip of tape and placing a coverslip (22 x 40 mm) over the top. In both cases coverslips were soaked in saturated KOH in 95 % ethanol, washed and dried immediately prior to use.

2.3.1 TETHERED CELL ASSAY

1 ml of cells were centrifuged at 4,000 g for 2 min and resuspended in 500 μ l of HEPES buffer (10 mM Na-HEPES, pH 7.2, Appendix A). Anti-filament IgG was diluted 1/10 in 18 μ l of cell suspension, added to the tunnel or flow slide and left to incubate for 15 min upside down. 200 μ l of HEPES was flushed through to remove untethered cells.

2.3.2 *R. sphaeroides* BEAD ASSAY

SUMMARY

Cells had their flagella truncated and were stuck down to the coverslip using polylysine. Primary antibody raised in a rabbit to sheared filaments (predominantly containing FliC) was then bound to the flagellar stubs. Polystyrene beads, which had previously been labelled with secondary antibody, then bound to primary antibody on the flagellar stubs (Figure 2.4).

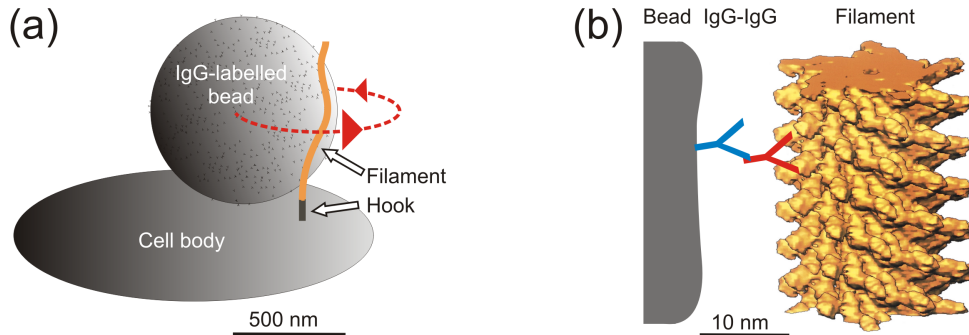


Figure 2.4: The *R. sphaeroides* bead assay, drawn to scale. Representation of filament in (b) is based on cryo-electron data, taken from [99].

BEAD PREPARATION

100 μl carboxyl-modified beads (0.83 or 1.90 μm , 4 % w/v, Interfacial Dynamics Corp.) were added to 1.5 ml MES buffer (50 mM 2-(N-morpholino)ethanesulfonic acid, pH 6.0), spun down at 16,000 g for 7 min, resuspended in 50 μl 1-Ethyl-3-(3-dimethylaminopropyl) carbodiimide hydrochloride (EDAC, Figure 2.5) (50 mg/ml in MES, Invitrogen), and sonicated in an ultrasonic bath (Ultraware Ltd.) for 15 min. The beads were then washed twice by spinning down in 1.5 ml MES (16,000 g for 7 min). The pellet was resuspended in 100 μl goat anti-rabbit IgG (0.6 mg/ml in MES, AbCam), sonicated again for 15 min, and gently agitated overnight at 4 $^{\circ}\text{C}$. Antibody-labelled beads were kept at 4 $^{\circ}\text{C}$ and used within a few weeks.

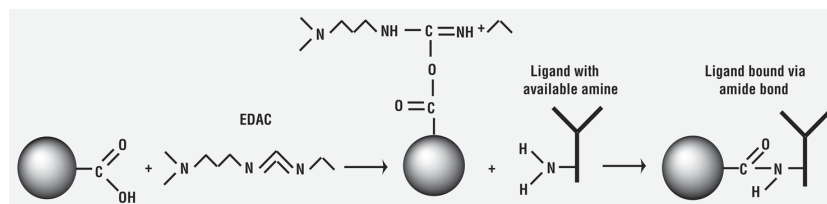


Figure 2.5: Carboxyl-modified beads are coupled to antibodies via EDAC.

SLIDE PREPARATION

Four buffers were used in the slide preparation; Buffer 1 - 80 mM NaCl, 0.1 % BSA in HEPES pH 7.2, Buffer 2 - 20 mM NaCl in HEPES pH 7.2, Buffer 3 - 20 mM NaCl, 0.1 % BSA in HEPES pH 7.2, and Buffer 4 - HEPES pH 7.2. 10 μl of IgG stock beads was added to 1.5 ml Buffer 1 and spun down at 16,000 g for 7 min, resuspended in 20 μl Buffer 1, and sonicated for 15 mins to prevent clumping. Approximately 800 μl of cells (grown to OD_{700} 0.45–0.65) had their flagellar filaments sheared off by passing the suspension back and forth 40 times between two syringes with 26-gauge needles connected by a piece of polyethylene tubing. The cells were then spun down (4,000 g, 2 min) and resuspended in 400 μl Buffer 4. 20 μl of 0.1 % polylysine (Sigma) was added to the flow cell and left for 20–60 s, followed by 100 μl Buffer 2, and then 20 μl cell suspension. This was left upside down for 5–10 min. 100 μl Buffer 3 was wicked through, followed by 10 μl of diluted anti-filament rabbit IgG (diluted 1/5 in Buffer 3), which was then left to bind for 15 min. 20 μl of antibody-labelled bead suspension was added (taken from ultrasonic bath immediately before use) and incubated for 5 min before gently flushing out with 50 μl Buffer 2 and then 100 μl Buffer 4. The volumes were increased (approximately 10 times) when preparing a flow cell rather than a tunnel slide.

2.3.3 BFP INTERFEROMETRY AND OPTICAL TRAP SETUP

The optical trap used in these experiments was built by Dr Pilizota [100, 101]. Figure 2.6 shows the layout of the trap. It consists of a custom-built inverted microscope and two lasers - a 632 nm Helium Neon (Coherent, USA) and a 1064 nm Ytterbium fibre laser (IPG Photonics Corporation, USA). Position detection is by BFP interferometry using either laser beam focused into the specimen plane by the objective and collimated by the condenser onto the face of a quadrant photodiode in the BFP of the condenser. The 1064 nm laser was also used to trap cell bodies for experiments in Chapter 6. Data acquisition and control of the optical trap via the acousto-optic deflectors (AODs) were all performed by a DSP board installed in a host computer.

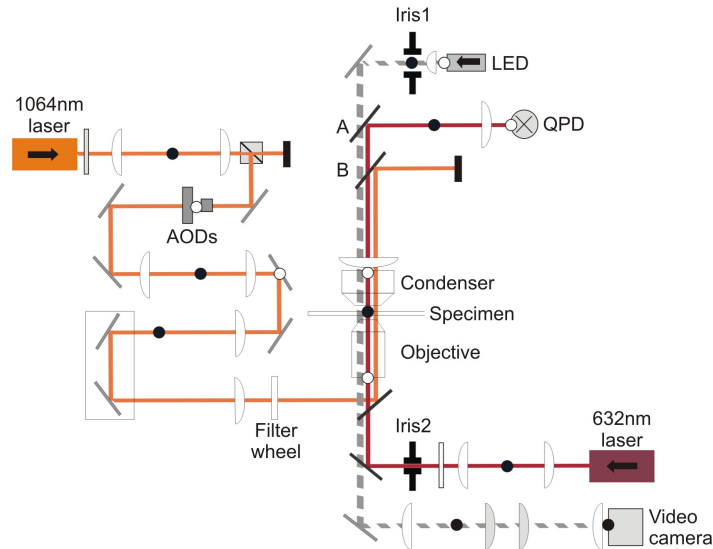


Figure 2.6: Layout of the optical trap used in these experiments (adapted from [100]).

Bright-field imaging. Bright-field imaging uses an LED, high numerical aperture condenser, 100X oil-immersion objective, and a high-sensitivity black and white charge-coupled device video camera (LCL-902K, Watec).

632 nm detection. In addition to the presence of two neutral density (ND) filters (both $ND = 1$, giving an intensity of $177 \mu\text{W}$), the intensity of the laser could be reduced by closing the iris (Iris2), which increased the detector range at the expense of sensitivity. Beads of diameters $0.83 \mu\text{m}$ (iris half-closed) and $1.90 \mu\text{m}$ (iris fully-closed) were recorded with a laser power of $20 \mu\text{W}$ and $1.8 \mu\text{W}$ respectively.

1064 nm detection. 1064 nm detection was achieved by swapping dichroic mirrors labelled A and B. The laser power whilst detecting was 10 mW (100 mW with no filters).

1064 nm trapping. Fine control of the trapping laser is achieved with AODs and the DSP board in the PC. The intensity of the 1064 nm laser was varied via the laser diode current. For experiments in Chapter 6 a filter-wheel containing ND filters ($ND = 0.0, 0.3, 0.5$, and 1.0) was used for fast, uniform intensity changes.

2.3.4 DATA ANALYSIS

ROTATION ANALYSIS

As explained in Section 1.4.3, two methods were used to record bead position over time; the power-spectrum method or the $d\theta/dt$ method. In the power-spectrum method, P_x and P_y were combined to form a complex signal. The peak in the power-spectrum was taken for each 1 second window of data every 0.1 s (note that the program converts any negative speeds, objects rotating in the CW direction, to equivalent positive speeds) [27]. In the $d\theta/dt$ method, an ellipse is fitted to the bead's trajectory using a downhill simplex method as described in Section 2.6 of [78]; ellipses are then projected onto a circle. The quality of the fit depends on the bead's trajectory which can vary greatly between cells (see Figure 3.2 for examples). Trajectories that did not fit the ellipse well (judged by eye), were discarded. Angular velocity (ω) was calculated from angle versus time data ($\omega = d\theta/dt$) and filtered with a 200 point median filter (sliding window in 1 point increments). The $d\theta/dt$ method was used unless otherwise stated (Sections 3.2.2 and 4.2.4).

STOP ANALYSIS

For Chapter 3 a Matlab program (written by Dr T. Pilizota and R. Branch) selected cells as follows. (1) The mean speed (M_{CCW}) was calculated by fitting a Gaussian to the speed histogram of the 30 s data trace. (2) Stop events were measured from when speed decreased to 0.1 M_{CCW} to when speed increased above 0.4 M_{CCW} . (3) Stop events were screened by a 45° moving window and the largest number of stops registered within a 45° sector subjected to a binomial test. Cells with non-uniformly distributed stop angles (i.e. those that were sticking) were discarded. Deceleration times were defined as the time it takes for the speed of the bead attached to the filament stub to decrease from 0.7 M_{CCW} to 0.1 M_{CCW} (or from 0.1 M_{CCW} to 0.7 M_{CCW} for acceleration times). See Figure 2.7 for an example.

TORQUE ANALYSIS

The M_{CCW} was calculated by fitting a Gaussian to the speed histogram of the 30 s data trace, above a threshold of 20 Hz and 1 Hz for 0.83 μm and 1.90 μm beads respectively. Torque ($T = f \cdot \omega$) was estimated by calculating (1) $\omega = 2\pi \cdot M_{CCW}$ and (2) the viscous drag (f) on the bead, $f = 8\pi\eta r^3 + 6\pi\eta r l^2$ where η is viscosity, r is bead radius, and l is eccentricity (radius of orbit). For the bead sizes used, contribution from the filament stub is negligible [34] and was therefore neglected.

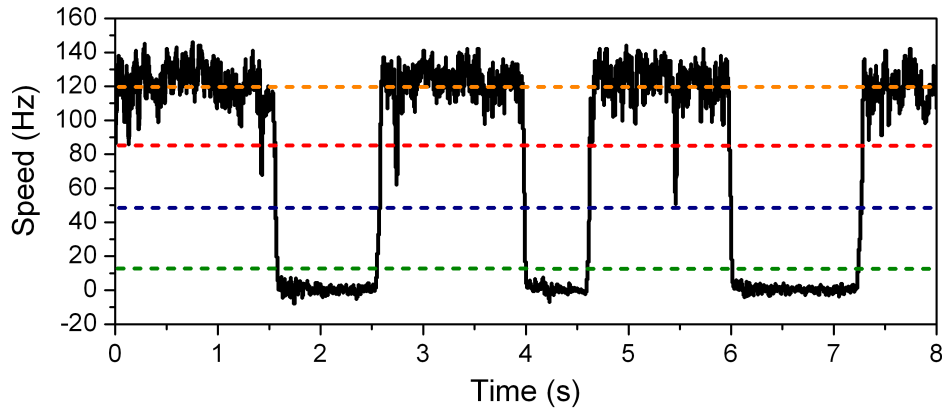


Figure 2.7: An illustration of how stop events were identified and measured. The orange line represents the M_{CCW} . Stop events were identified and measured from when speed decreased to $0.1 M_{CCW}$ (green line) to when speed increased above $0.4 M_{CCW}$ (dark blue line). The red line ($0.7 M_{CCW}$) represents the start of the deceleration and the end of the acceleration. The green line ($0.1 M_{CCW}$) represents the end of the deceleration and the start of the acceleration. Using this method the shortest recorded stop event was 3.2 ms.

The eccentricity of rotation was measured as follows (previously described in [101]). (1) A bead stuck to the coverslip was moved through the detector laser focus using the piezo stage to find the centre of the detector beam. (2) With the bead in the centre, the position of the detection laser in x and y were adjusted to zero using a mirror that steers the detector laser beam onto the quadrant photodiode. (3) Steps 1 and 2 were repeated several times to get the best possible alignment. (4) By applying known voltages, the stage was moved over a $\sim 1 \mu\text{m}^2$ range (following a virtual grid), whilst the position of the stuck bead was recorded as normal. (5) Calibration parameters were computed by fitting the known and measured values obtained above (in the linear detection range only). This procedure was carried out immediately before recording beads on flagellar stubs for both bead sizes used.

STEP ANALYSIS

Step analysis was performed by Dr T. Pilizota using a computer algorithm as described previously [37]. This algorithm fits one step, then another, and another and so on. As it goes, it works out a ‘quality factor’ which provides an indication of the ratio of [the number of steps found] to [the number of steps fitted].² In theory the peak value of ‘quality factor’ gives a fit that best represents real steps in the data [102]. In practice a fit that slightly overfits the data (but still gives a high quality factor) was chosen [102, 37].

²This has been validated using fake datasets with a known number of steps.

WILD-TYPE MOTOR OUTPUT: SPEED, TORQUE AND STOPS

3.1 OVERVIEW AND AIMS

The aim of this project was to learn more about how *R. sphaeroides* controls its start-stop flagellar motor. Previously, bar one exception where a quadrant photodiode was used, motor behaviour has been studied by recording tethered cells with a video camera as described in Section 1.4.2. There are several fundamental problems with this procedure.

1. **Speed analysis.** Little can be concluded about motor speed due to (a) uncontrolled load variation (i.e. cell body dimensions differ widely), (b) 25 Hz maximum speed accuracy, and (c) limitations in tracking software including a bias towards larger/dividing cells.
2. **Stop analysis.** The poor time resolution and quality of the data means that analysing stop events is very difficult as many stop events will be missed or smoothed so much they appear as slow-downs.
3. **Data presentation.** Because of the difficulty of identifying stop events, typically a speed-time graph of the population (formed by averaging together all the single-cell responses) is used to describe a strain's chemotactic ability (see Figure 1.15). This is very crude and provides limited information about the chemotactic response - stop frequency versus time would be more appropriate.

Considering that recording the rotation of sub-micron beads on flagellar stubs of *E. coli* at a high resolution is now standard practice, there was a strong incentive to develop a bead assay for *R. sphaeroides*. In the *E. coli* bead assay the bead spontaneously binds to a mutated filament protein, FliC^{sticky} [79]. The same mutations have been made in *R. sphaeroides* but produces a non-flagellate strain (G.H. Wadhams, unpublished).

Thus the initial aim of this chapter was to produce a reliable bead assay for *R. sphaeroides*. Upon achieving this goal, the output of *R. sphaeroides* motors under the control of the wild-type chemosensory system was examined in detail.

3.2 RESULTS

Wild-type cells were recorded in a tunnel slide and analysed using custom software as described in Section 2.3.

3.2.1 THE *R. sphaeroides* BEAD ASSAY

A protocol for sticking beads to *R. sphaeroides* flagellar stubs using antibodies was designed by Dr M.C. Leake, Dr T. Pilizota, Dr M. Kojadinovic, and myself. Carboxyl-modified polystyrene beads were labelled with secondary antibody (goat anti-rabbit IgG) using a linker called EDAC. Then cells, prepared in the same way as *E. coli* (sheared and stuck down to the coverslip with polylysine) were exposed anti-filament IgG raised in rabbits. When the beads were added, the secondary antibody labelled beads bound to the primary antibody labelled flagellar stubs.

Beads on flagellar stubs of *R. sphaeroides* behaved differently to beads on *E. coli* stubs. The trajectories tend to be messier (*E. coli* trajectories are smoother) and beads on long filaments often rotated on very tight trajectories well above the cell body, moving closer to the cell body when stopped (see Figure 3.1 and video in Appendix D.2, Page 131). These traits most likely reflect differences in the hook and filament between the two species.

3.2.2 THE MOTOR ROTATES CCW NOT CW

The direction of bead rotation was determined by examining the trajectory (Figure 3.2). Of the 385 wild-type cells recorded in this study, 382 (99.2 %) rotated in the CCW direction as viewed from the distal end of the filament. Of the three beads rotating in the CW direction, two were on their side and the other was probably

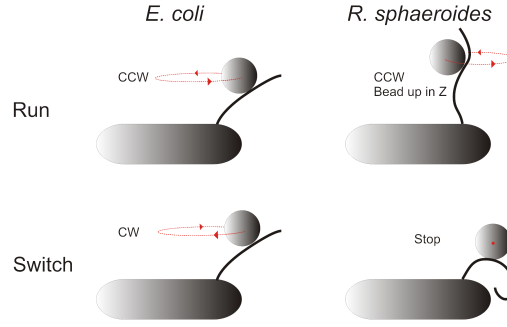


Figure 3.1: Cartoon comparing the *E. coli* and *R. sphaeroides* bead assay. In *R. sphaeroides*, beads attached to long filaments often rotated on very tight trajectories well above the cell body. During a stop the bead moved closer to the cell body, as expected if the filament adopted a high-amplitude short-wavelength coil as previously observed [52].

misaligned in the trap. In contrast, Armitage and Macnab (1987) stated that the motor rotated in the CW direction by monitoring the direction of tethered cells [51].

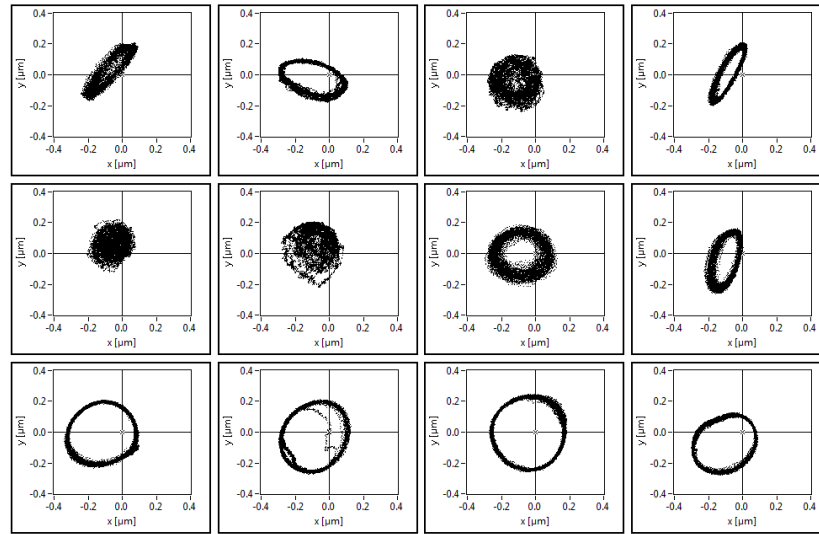


Figure 3.2: Examples of $0.83 \mu\text{m}$ bead trajectories on the filament stubs of *R. sphaeroides*. The best trajectories are those which are near circular. The four trajectories on the bottom row are by far the best but are from cells with filaments that have not been sheared well enough and were therefore not included in the analysis. 1 s of data are shown (10,000 points).

There are several factors to take into consideration when deciding whether a motor rotates in the CW or CCW direction. For instance, one must be aware of the convention (viewed from the distal end of the filament), and the presence of any inversions in the microscope setup (e.g. whether the microscope is focused on the coverslip not the glass base/whether the microscope objective is inverted/whether the signal

from the quadrant photodiode is inverted). However, beads on *R. sphaeroides* stubs rotate in the same direction as CCW-rotating beads on *E. coli* stubs when recording with the same setup (i.e. slide preparation, microscope and board/programs), indicating that the *R. sphaeroides* motor rotates in a CCW direction.

TETHERED CELLS ROTATE IN EITHER DIRECTION

Next, tethered cell slides were prepared and videos examined to see why the direction of motor rotation is different to that measured previously [51]. It was apparent that slides typically contained some cells that rotated in one direction and some that rotated in the other direction (but were not seen to switch). Unlike the bead assay in which 99.2 % of motors rotate in the same direction, typically only 84–93 % of tethered cells rotate in the same direction (see Table C.1, Page 125 for raw data).¹ These proportions can vary greatly from slide to slide; often the ratio was about 50:50, which conflicts with the bead data where motors rotate in the same direction.

So how can tethered cells rotate in both directions when beads only rotate in one direction? One possibility was that the cell bodies rotate faster than 25 Hz and thus become aliased. Aliasing is responsible for the *stroboscopic effect* giving the illusion that a rotating object (commonly a car’s wheel or plane’s propellor) is rotating with a different speed/sign than its true rotation (see Figure 3.3 for an example).

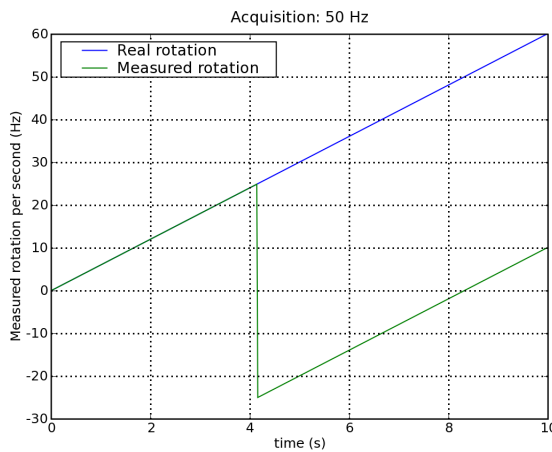


Figure 3.3: Aliasing simulation performed by Dr M. Kojadinovic. In this example imagine a tethered cell slowly accelerates from 0 to 60 Hz (blue line). If one were recording and analysing at 50 Hz (as is the case with the video camera/Hobson Bactracker setup, green line) cells rotating faster than 25 Hz would become aliased and appear to be rotating at the wrong speed and potentially in the wrong direction (e.g. a cell rotating forward at ~35 Hz would appear to be rotating backwards at ~15 Hz).

To address the aliasing problem, tethered cells were recorded by BFP interferometry (1064 nm laser and quadrant photodiode sampled at 5 kHz) rather than a video camera. Figure 3.4 shows their mean speeds. Whilst speeds of many cells are

¹Note that a CCW rotating motor will cause beads and tethered cells to rotate in the CCW direction when using the same setup.

high enough to become aliased, the sign of the peak of the power spectrum (relating to the speed and direction of the rotation of the cell body) corresponded to the direction of rotation detected by eye, except in a few instances. These cells were easily identifiable from their characteristic *strobing* motion. Thus aliasing does not explain why tethered cells can rotate in both directions.

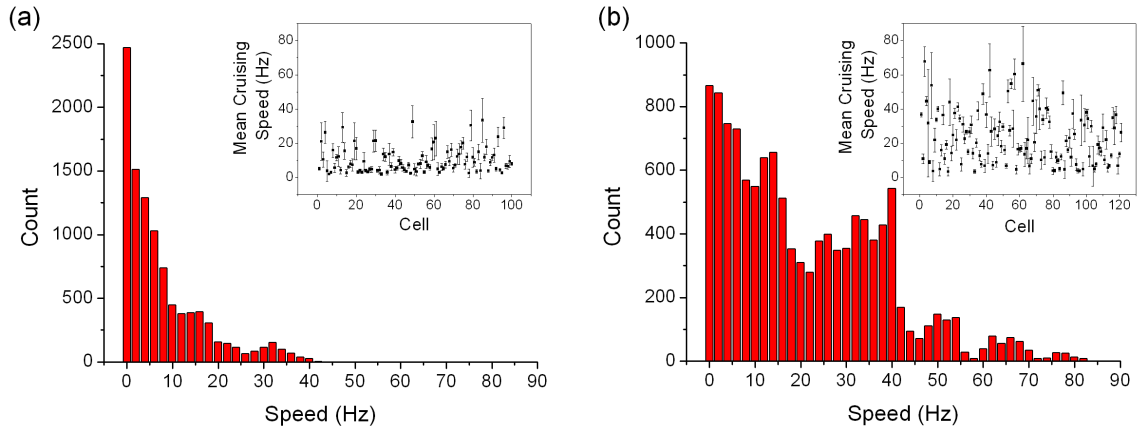


Figure 3.4: Speeds of tethered cells (grown (a) aerobically $n = 100$, (b) photoheterotrophically $n = 121$) recorded by BFP interferometry to see if they rotate fast enough to become aliased when recorded with a video camera. Each cell was recorded for 10 s each. The power-spectrum method was used to generate a speed-time trace for each cell which were combined to construct a histogram of the population. The mean speed and standard deviation of each cell (above a threshold of 1 Hz to remove stop events) was calculated (insets) yielding a population mean of aerobically and photoheterotrophically grown cells of 10.2 ± 7.5 Hz and 23.2 ± 15.5 Hz respectively. The speeds of photoheterotrophically grown cells were probably higher since they tend to be much smaller than aerobically grown cells and thus exert a lower load on the motor. The large range of speeds reflects large variation in cell size (and thus load on the motor).

So it is unclear why this discrepancy between beads and tethered cells exist. Perhaps cells are anchored to the glass either by another filament (as could be the case in a dividing cell) or part of the cell body itself, and the untethered filament/motor causes the cell body to be pushed round the anchor. Recording the motion of tethered cells expressing a fluorescently tagged motor component (e.g. Ypet-FliM (JPA1639)) may resolve this issue.

3.2.3 WILD-TYPE STOP EVENTS

The main incentive for the development of the *R. sphaeroides* bead assay was to improve the resolution of stop events. Here we examine the steady-state behaviour of WS8N. The rotation of $0.83\ \mu\text{m}$ beads on flagellar stubs from aerobically grown WS8N were recorded from three different populations for 30 sec each with the 632 nm laser at a sampling rate of 10 kHz. Data were 200 point median filtered (sliding window in 1 point increments). This gives a resolution of 20 ms at worst. Only beads with good trajectories were analysed. Of the 108 cells recorded, 41 were selected for analysis. Five traces are shown in Figure 3.5.

Next, what was counted as ‘a stop’, had to be defined. As this is an arbitrary measure, various cut-off thresholds were tried before the levels that consistently gave appropriate results were finalised. The motor was said to have stopped when speed transiently dropped below 10 % the motors mean running speed (M_{CCW}) before returning to above 40 % M_{CCW} . From the dataset, a total of 376 stop events were identified (see Appendix D.4, Page 131 for raw data). The mean deceleration and acceleration times² were $0.032 \pm 0.031\ \text{s}$ and $0.026 \pm 0.032\ \text{s}$ respectively. There was no indication of ‘de-resurrection/resurrection’ going into/out of stops and there was no correlation between the time taken to decelerate/accelerate and the duration of stop (Figure 3.6). Mean stop length and mean stop frequency (number of stops per s) were $0.66 \pm 1.01\ \text{s}$ and $0.31 \pm 0.19\ \text{s}^{-1}$ respectively, giving a run bias (fraction of time spent rotating) of 0.80 ± 0.20 . This is comparable with two other studies using tethered wild-type cells that were grown photoheterotrophically; cells stopped on average for $1.04 \pm 3.18\ \text{s}$ at a frequency of $0.22 \pm 0.17\ \text{s}^{-1}$ [81], and gave an unstimulated run bias of about 0.85 [74].

Whilst bias is regularly used as a measure of the chemotactic state of the cell, it is rather crude since two cells with the same bias could have markedly different free-swimming behaviours. Thus stop frequency may be a more appropriate measure of ‘re-orientation’ frequency. However, this is also problematic. Firstly, short stops below a certain threshold will not cause the cell to re-orientate at random, if indeed any re-orientation occurs at all. And secondly, due to the importance of Brownian motion at the micron scale, unless a cell swims for a certain distance before re-orientating, it is effectively still in the same place. Thus perhaps only stops of a certain/weighted length separated by a set time spent running are chemotactically relevant and should be analysed accordingly.

²The time taken to go from 0.7 to 0.1 or 0.1 to 0.7 M_{CCW} .

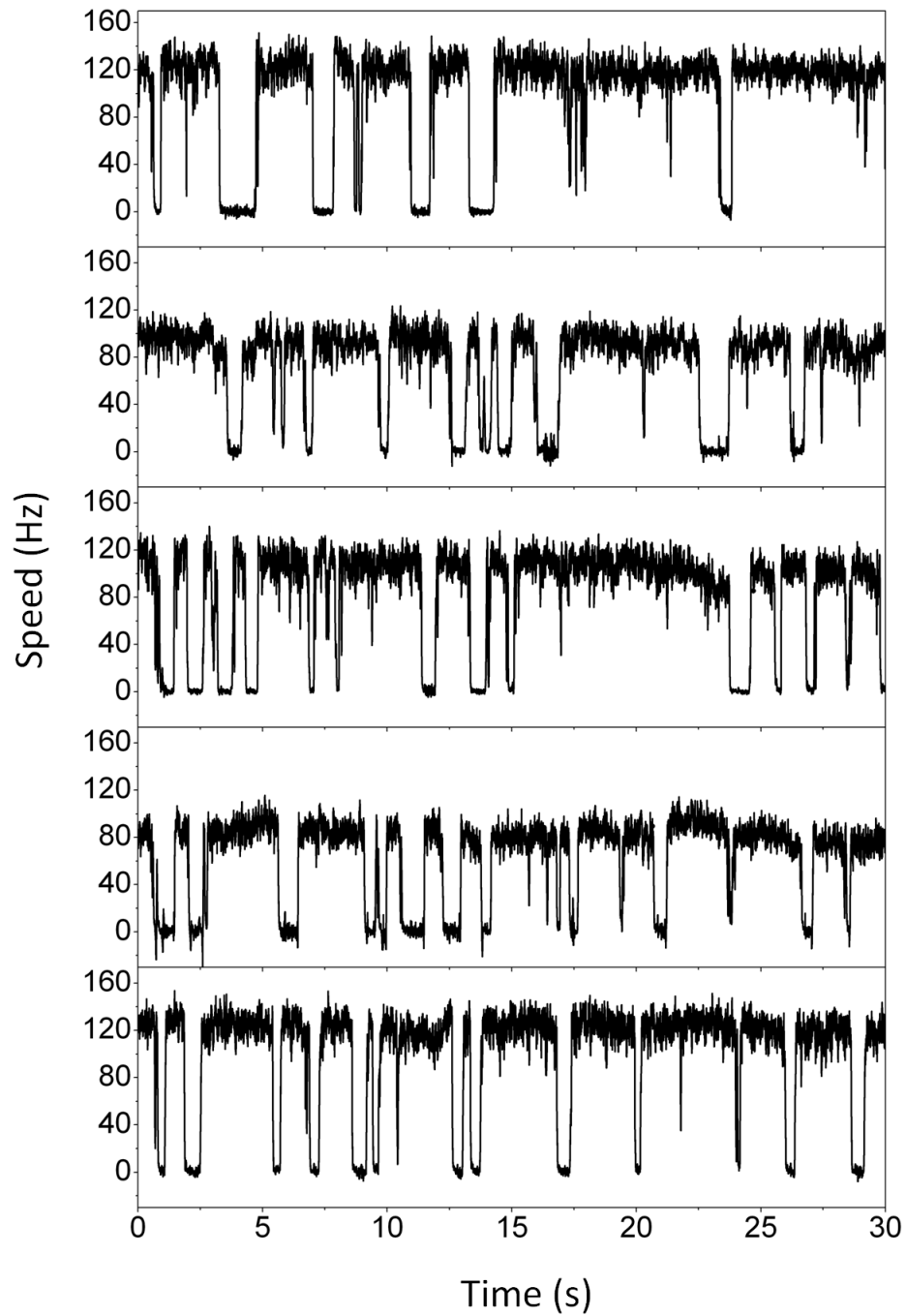


Figure 3.5: Five speed-time traces of $0.83 \mu\text{m}$ beads attached to flagellar stubs of WS8N. The variation in speed when undergoing a stop is significantly less than the variation in speed whilst rotating. At this load, the motor rotates at $\sim 100 \text{ Hz}$.

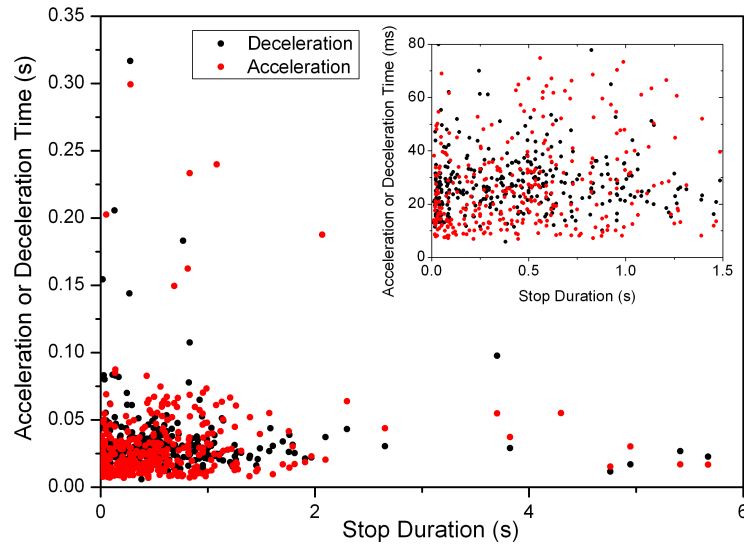


Figure 3.6: Length of stop observed in wild-type versus the acceleration or deceleration time associated with each stop. No correlation is apparent. *Inset*, expansion of first 1.5 s. The minimum time to decelerate of ~ 8 ms might reflect the time taken for a $0.83 \mu\text{m}$ bead on a *R. sphaeroides* flagellar stub to stop (due to its compliance).

3.2.4 PLATEAU TORQUE

In addition to examining stop events at a higher resolution, the *R. sphaeroides* bead assay permitted the examination of some basic motor characteristics; namely torque and speed. The torque-speed relationship of three flagellar motors have been examined in detail; the proton motor from *E. coli*, the sodium motor of *V. alginolyticus* and the chimaera³. At high loads ($> 0.6 \mu\text{m}$ beads attached to flagellar stubs), motors tend to rotate slowly, with a consistently high (plateau) torque [34]. The plateau torque is useful here because it provides a point of comparison between other motors.

For this reason (and as will become apparent in Chapter 6) motor torque was calculated from the speed and eccentricity radii of $0.83 \mu\text{m}$ and $1.90 \mu\text{m}$ diameter beads attached to flagellar stubs (Figure 3.7 and Table 3.1). The mean torque of $1,120 \pm 250$ and $1,330 \pm 290$ pNnm/rad for $0.83 \mu\text{m}$ and $1.90 \mu\text{m}$ beads respectively, is comparable to the plateau torque of the proton-driven motor from *E. coli* ($1,260 \pm 190$ pNnm/rad calculated using $1 \mu\text{m}$ beads [16]).

³An *E. coli* strain carrying non-native stators; PomA (*V. alginolyticus* MotA homologue) and PotB (a chimaeric protein containing the periplasmic C-terminus of MotB from *E. coli* and the membrane-spanning N-terminus of PomB from *V. alginolyticus*).

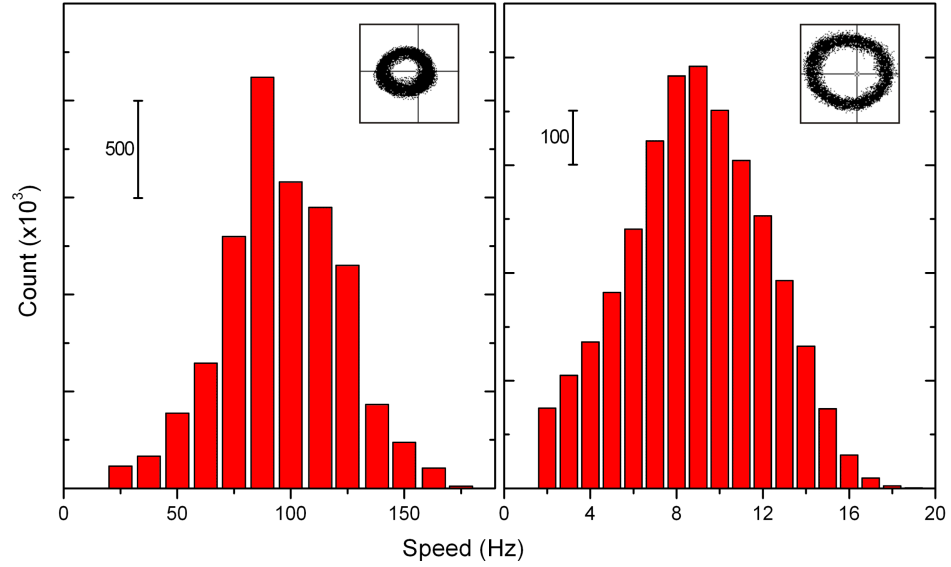


Figure 3.7: Speeds of motors pushing 0.83 μm and 1.90 μm diameter beads (left and right respectively). Cells were recorded for 30 s with the 632 nm laser at a sampling rate of 10 kHz (for 0.83 μm beads, $n = 41$) and 2 kHz (for 1.90 μm beads, $n = 110$). Beads of each size were recorded from three different populations. All the speeds from each bead size dataset were combined and used to construct the histograms. A threshold of 20 and 1 Hz was applied to 0.83 μm and 1.90 μm datasets respectively to remove stop events. *Insets* show a typical bead trajectory (10,000 data points) for each bead size used; the radii are 152 ± 28 nm and 311 ± 37 nm for 0.83 μm and 1.90 μm beads respectively.

Bead diameter (μm)	0.83	1.90
Speed (Hz)	98.6 ± 22.4 (41)	9.8 ± 2.9 (110)
Eccentricity radii (nm)	127 ± 28 (15)	299 ± 91 (46)
Angular velocity (rad/s)	620	62
Drag (pN nm s/rad ²)	1.80	21.64
Torque (pNnm/rad)	$1,120 \pm 250$	$1,330 \pm 290$

Table 3.1: Computing torque for motors pushing 0.83 μm and 1.90 μm diameter beads, calculated as described in Section 2.3.4. Measured speeds and eccentricities of rotation (size of orbit) are shown in the top panel. The numbers in brackets relate to the number of beads recorded; eccentricity radii were determined on a subset of the population. The middle panel shows the speed (in appropriate units) and calculated drag coefficient of the beads (see Section 2.3.4, Page 48 for equation). A value of 9.86×10^{-10} nP was used as the viscosity value. See excel file in Appendix D.4 for full details of the calculation. Note that a *R. sphaeroides* motor pushing a 0.83 μm bead generates $\sim 7 \times 10^5$ pN nm/s of power.

3.2.5 TRANSIENT STEP CHANGES IN SPEED

Being able to determine motor speed with such accuracy also allows other events to be identified. It has been observed that wild-type *E. coli* motors can fluctuate between discrete speed levels (thought to correspond to the addition or removal of a stator or two) [16]. Similar speed changes were often observed in *R. sphaeroides* motors in both wild-type and *che* mutant strains such as JPA1353. Figure 3.8 shows some examples from wild-type cells. Unfortunately it was not possible to identify a common step size and thus estimate the number of stators per motor.

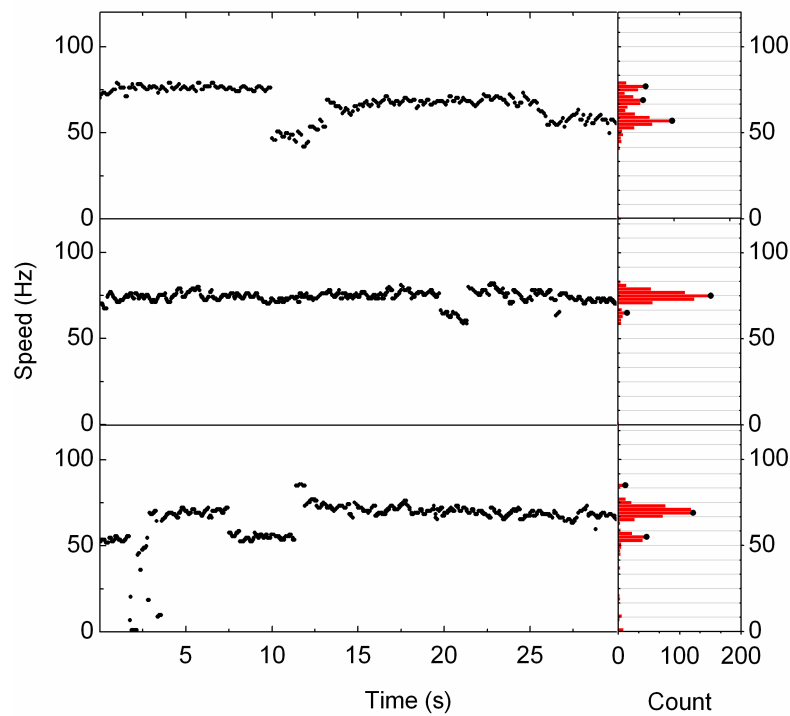


Figure 3.8: Some examples of abrupt changes in speed that were often observed in *R. sphaeroides* speed-time traces from $0.83 \mu\text{m}$ beads attached to flagellar stubs. The black dots in the histogram represent peaks picked out by the standard LabView peak-finding algorithm (performed by Dr T. Pilizota).

3.3 CONCLUSIONS

Establishing a reliable bead assay protocol, which will enable future experiments to be conducted at a high-resolution at controllable loads, is a major contribution of this thesis. It has permitted the accurate measurements of the *R. sphaeroides* motor output in terms of speed, torque and stop events.

Under the conditions tested, the *R. sphaeroides* motor exhibits a similar performance to its *E. coli* proton-driven counterpart:

1. The plateau torque (1,120–1,330 pNnm/rad) is comparable to the plateau torque of the proton-driven motor from *E. coli* (1,260 pNnm/rad) [16]. Using smaller beads will permit the lower part of the *R. sphaeroides* flagellar motor torque-speed curve to be measured.
2. Also like in *E. coli*, motor speed often jumps from one level to another. Future *resurrection* experiments will determine the approximate number of stators in a typical *R. sphaeroides* motor.
3. Finally, the *R. sphaeroides* motor rotates in the same direction as the *E. coli* motor. This suggests that the *R. sphaeroides* helical filament may well be left-*not* right-handed as previously thought [53].

In order for *R. sphaeroides* to propel its cell body forward (see video in Appendix D.2, Page 131), a CCW rotating motor would need to be coupled to a left-handed helical filament (like in *E. coli*). However it was previously determined, from 2D phase-contrast images of filaments from tethered cells, that the propulsive filament form is right-handed (see Figure 1.9, Page 14) [53]. However, it is impossible to determine the handedness of a helix from a 2D projection (Shin-Ichi Aizawa, personal communication), a 3D stack/video is required (see how your brain can be tricked by this optical illusion (ppt slide in Appendix D.2, Page 131)). Fluorescently-labelling the filament and monitoring its rotation in free-swimming cells suspended in a very viscous solution will enable both the handedness of the helix and the direction of rotation to be determined simultaneously.

Despite similarities in motor performance, the motors found in *E. coli* and *R. sphaeroides* are coupled to a different molecular gearbox. The bead assay enabled the examination of wild-type stop events. There was a large variability in stopping frequencies between cells. This could be due to stochastic variations in copy number of chemosensory pathway components. Alternatively, perhaps it is because what seems to be a homogeneous environment to us, is not from a bacterium's perspective; just like surfaces that look smooth to the eye actually consist of a series of ridges and valleys when viewed with a microscope. Long time course measurements of single cells could determine if the variability was primarily due to differences between cells or simply that each cell exhibits a wide range of stopping behaviours over time. The next chapter deals with a much more fundamental issue concerning stops - do CheYs stop or promote motor rotation in *R. sphaeroides*?

FUNDAMENTAL MOTOR CONTROL

4.1 OVERVIEW AND AIMS

This chapter is concerned with understanding the fundamentals of motor control in *R. sphaeroides*; primarily, what is the ‘default’ behaviour of the motor? In addition, can *R. sphaeroides* really control motor speed (termed chemokinesis) as previously reported [80, 81, 83, 84, 85]?

4.2 RESULTS

The previous chapter described the behaviour of motors under the control of the wild-type chemotaxis system. Here, signal inputs to the motor were manipulated, either genetically or by exposing cells to different chemotactic stimuli.

4.2.1 ‘DEFAULT’ MOTOR BEHAVIOUR

In *E. coli*, a $\Delta cheY$ strain is smooth swimming since there is no CheY-P to cause the motors to switch [103]. In contrast a *B. subtilis* $\Delta cheY$ strain constantly tumbles since CheY-P is required to stabilise CCW rotation [70, 104, 105]. However in *R. sphaeroides*, the stop frequency of unstimulated JPA1337 ($\Delta cheY_{1-6}$) and WS8N are indistinguishable from one another [62]. Despite the deletion of many of chemotaxis genes, no obvious effect on unstimulated stopping frequency has been observed in over 20 years of research. To identify the default motor behaviour, a strain was examined that had all known *che* genes deleted (JPA1353 (Δche), Figure 4.1).

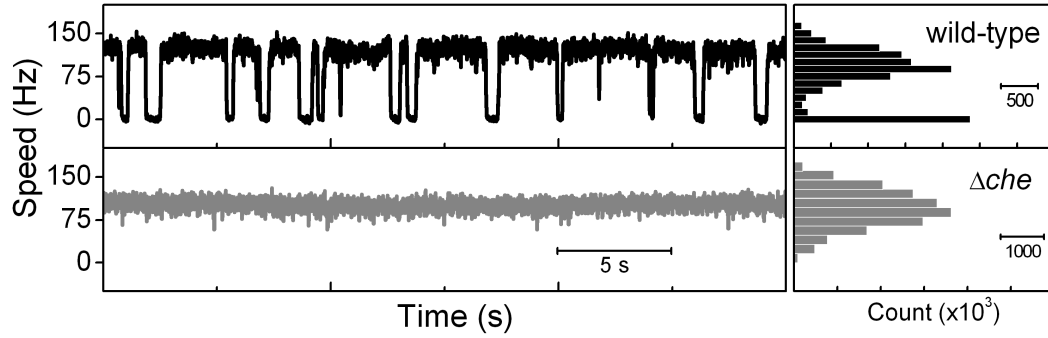


Figure 4.2: The behaviour of $0.83 \mu\text{m}$ beads attached to flagellar stubs of WS8N (black, $n = 41$) compared to JPA1353 (Δche , grey, $n = 63$). The $d\theta/dt$ method was used to generate a speed-time trace for each cell. The speeds of all the cells in each population were combined to construct the histograms.

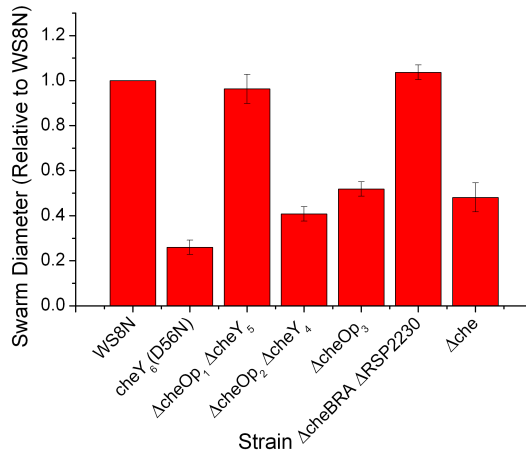


Figure 4.3: Swarm diameters of JPA1353 (Δche) relative to WS8N and other strains that host large deletions; JPA443 ($\Delta cheOp_1$ and $\Delta cheY_5$), JPA419 ($\Delta cheOp_2$ and $\Delta cheY_4$), JPA1301 ($\Delta cheOp_3$), and JPA1349 ($\Delta cheBRA$ and $\Delta RSP2230$). JPA1213 ($cheY_6(D56N)$) is a non-motile control.

JPA1319 was smoother swimming than wild-type (Figure 4.4, $P < 0.05$ Chi-Sq), suggesting that the CheYs must stop the motor when phosphorylated. However at this stage, the data do not identify which CheYs are responsible. More detailed experiments are needed to identify the roles of different components, particularly since CheY₃/CheY₄ are phosphorylated by CheA₂ and CheY₆ is primarily phosphorylated (and de-phosphorylated) by CheA₃.

4.2.3 MOTILITY AND MOTOR SPEED IN PBS BUFFER

The preliminary *R. sphaeroides* bead assay protocol was carried out in PBS buffer (as beads stuck well to filaments in this buffer). However when wild-type cells (grown in succinate medium to an OD where cells are vigorously motile) are resuspended in PBS buffer, they become entirely non-motile. It has been suggested that phosphate ions alone are enough to elicit this response [106]. To understand why this occurs, the motility of JPA1353 in PBS buffer was investigated to see if the

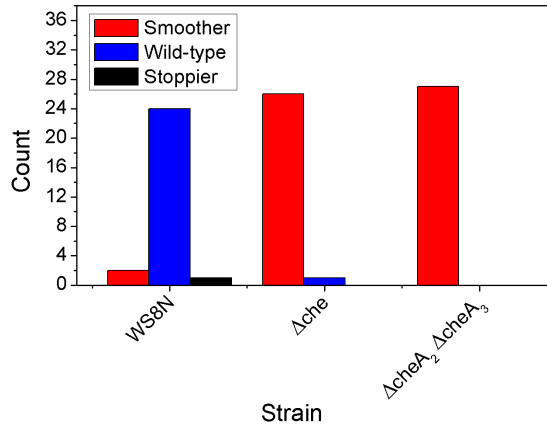


Figure 4.4: Free-swimming phenotype of JPA1319 ($\Delta cheA_2 \Delta cheA_3$) relative to WS8N and JPA1353 (Δche), tested blind in capillary tubes by eye using a light microscope. Their behaviour was marked on a scale of 1 = smoother than WS8N, 2 = indistinguishable from WS8N, 3 = stoppier than WS8N. See Section 2.2.2, Page 43 for method. Only 3 of the 11 strains tested at the same time are shown. JPA1353 and JPA1319 are significantly smoother than WS8N ($P < 0.05$ Chi-Sq).

non-motile phenotype was due to a chemotactic response. JPA1353 motility was indistinguishable whether resuspended in succinate medium or PBS buffer. When the test was repeated with WS8N, the entire population was virtually non-motile in PBS buffer. Thus the non-motile phenotype of WS8N in PBS buffer is a chemotactic response. No other chemoeffector has been found to elicit a repellent response in *R. sphaeroides*. Once a controlled experiment is carried out in a flow cell, it may reveal that a component of PBS² is the first *R. sphaeroides* repellent to be identified.

The speed of motor rotation in PBS_s was compared to that in HEPES. PBS_s stands for PBS buffer supplemented with 10 mM sodium succinate (which acts as an attractant, thus increasing the yield of WS8N slides). Table 4.1 shows a comparison of the speeds of motors with 0.83 μm beads, obtained with WS8N and JPA1353 in the two different buffers. Whilst the speed difference between the two strains in either buffer is negligible, there is a significant difference in speed between the two buffers ($P < 0.05$ ANOVA). Motors rotate $\sim 75\%$ slower in PBS_s. This is in part due to an increased (less electronegative) membrane voltage in PBS_s buffer (Table C.2, Page 125).

Strain	Buffer	n	Mean Speed (Hz)
WS8N	HEPES	41	98.6 ± 22.4
JPA1353	HEPES	63	94.7 ± 23.1
WS8N	PBS _s	41	75.1 ± 17.4
JPA1353	PBS _s	105	70.1 ± 18.0

Table 4.1: Mean speeds of 0.83 μm beads attached to flagellar stubs of WS8N and JPA1353 in HEPES and PBS_s buffer. Beads were recorded for 30 s each at 10 kHz with the 632 nm laser. Speeds were determined for each cell as described in Section 2.3.4.

²PBS buffer consists of 1.5 mM KH_2PO_4 , 8.1 mM Na_2HPO_4 , 140 mM NaCl, and 2.7 mM KCl.

4.2.4 THE CHEMOTAXIS SYSTEM DOES NOT CONTROL MOTOR SPEED

The term ‘chemokinesis’ was coined by Brown *et al.* to describe the controlled variation in swimming speed of *R. sphaeroides* in response to changes in chemoeffector concentration [84]. Early studies of free-swimming cells showed that *R. sphaeroides* swam significantly faster when resuspended in HEPES supplemented with weak organic acids (44 % and 60 % faster in 1 mM propionate or pyruvate) than in HEPES alone [83, 84]. More controlled experiments, using tethered cells in a flow cell, confirmed that the same pattern was observed in single cells (as in Figure 1.15, Page 23) [80, 81]. It was also concluded, from the analysis of tethered cells at steady-state, that *R. sphaeroides* had a “variable-speed rotor” [85]. In all cases cells were recorded with a video camera.

Chemokinesis has also been observed in *Sinorhizobium meliloti* and the lateral flagella of *V. alginolyticus* [107, 108]. In both cases, tethered cells were recorded with a video camera. As one would expect, the *S. meliloti* strains $\Delta cheA$ and $\Delta cheY_2$ swim significantly faster than a wild-type strain [107]. Given that the motors from the *R. sphaeroides* strains JPA1353 and WS8N rotate at the same speed (Section 4.2.1) it questioned whether chemokinesis really existed in *R. sphaeroides*.

To test this, the rotation of 0.83 μm beads attached to flagellar stubs of aerobically ($n = 16$) and photoheterotrophically grown cells ($n = 10$) were recorded in a flow cell from three different populations with a 1064 nm laser at 2 kHz. Each bead was recorded for 2 min in HEPES buffer, 2 min in 1 mM propionate (made up in HEPES), and 4 min in HEPES. It took approximately 45 s to exchange buffers during which no data were recorded. Figure 4.5(a) shows some typical recordings; stop frequency clearly reduces in the presence of propionate but motor speed remains the same. When propionate is removed the bead stops, typically for 1–2 mins, after which periods of rotation become more and more frequent as the cell adapts. Of the 26 cells recorded, the mean speed difference in the two buffers (Figure 4.5(b)) was 0.42 Hz.

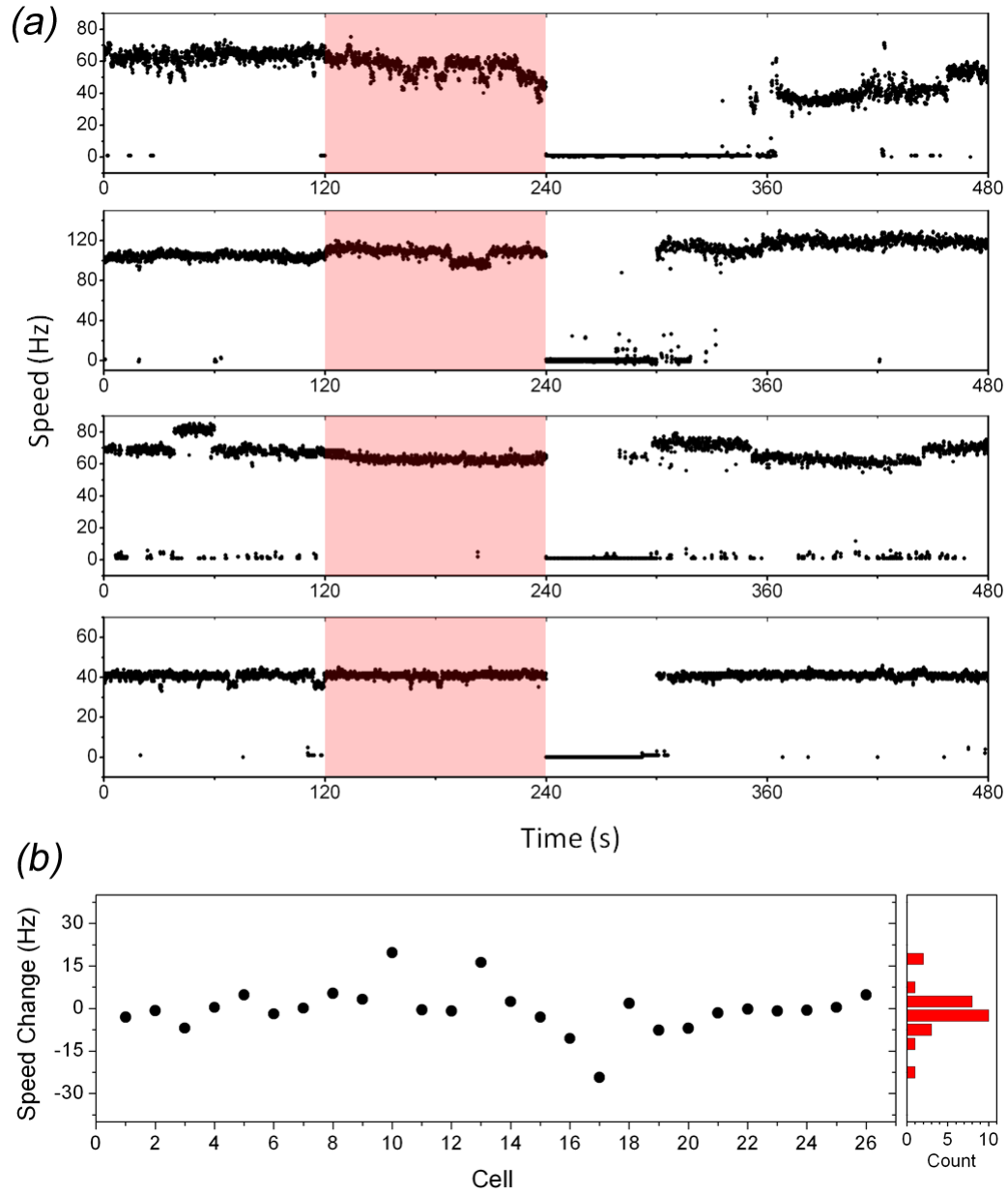


Figure 4.5: Measuring changes in motor rotation rate during chemotactic stimulation. (a) Four speed-time traces of $0.83\ \mu\text{m}$ beads attached to flagellar stubs of wild-type cells recorded in a flow cell. The pink shaded regions (120–240 s) correspond to when the cells were in 1 mM propionate solution. The power-spectrum method was used to calculate speed-time traces for each cell. The top two traces are from aerobically grown cells, whilst the bottom two are from photoheterotrophically grown cells. (b) The difference in speed for each cell exposed to 1 mM propionate versus just HEPES. This was calculated by subtracting the mean speed in propionate (2–4 mins) from the mean speed in HEPES (0–2 mins). Note mean speed was calculated above a threshold of 10 Hz to remove biases from stops. Cells 1–16 cells were grown aerobically; cells 17–26 were grown photoheterotrophically. Histogram (*right*) shows speed that the speed change centres about 0 Hz.

4.3 CONCLUSIONS

The results of this chapter can be summarised in a single sentence. *The R. sphaeroides motor rotates continuously at full speed unless it receives a signal to stop by phosphorylated CheYs.*

It is likely that the previous observed phenomenon of chemokinesis [80, 81, 83, 84, 85] was an artifact of using a low resolution experimental setup (i.e. recording with a video camera and using sub-optimal analysis). Stop events maybe smoothed so much that they appear as slow downs. Fewer stop events in propionate solution may have given the impression that motor speed increases when actually it does not. If this premise is correct, then tethered JPA1353 cells should appear to rotate faster than WS8N when analysed using video microscopy. It also remains to be seen whether *S. meliloti* and *V. alginolyticus* really exhibit chemokinesis, since in both cases cells were recorded with video cameras. The bead assay could be used to find out.

Another finding was that phosphorylated CheYs stop the motor, since a strain lacking functional CheA proteins showed smoother rotation than wild-type. Thus one can assume that CheA₂ and CheA₄ auto-phosphorylate upon attractant removal (resulting in a long stop), but this must be tested directly. The next chapter addresses whether all the CheYs have the same motor-stopping capabilities.

MOTOR CONTROL AT THE MOLECULAR LEVEL

5.1 OVERVIEW AND AIMS

It is well documented in *E. coli* and *S. enterica* that the direction of motor rotation is regulated by the interaction between CheY and FliM proteins. Upon phosphorylation by CheA at the pole of the cell, CheY-P diffuses throughout the cytoplasm and binds to FliM situated at the base of the motor, causing a change in motor direction. The aim of this chapter was to probe interactions between the *R. sphaeroides* CheY and FliM proteins. A previous study showed that all six CheYs (CheY₁₋₆) bind to FliM₁ *in vitro* and that this binding is enhanced ~ 3 -fold upon phosphorylation [67]. Here the interaction was probed *in vivo*, beginning by examining mutants that have point mutations in the putative CheY-binding domain of FliM₁.

Next, strains containing *cheY*₃ *cheY*₄ phosphorylation site mutants were analysed. This builds on previous mutational analysis of the *cheY* genes, which showed that a minimum of two CheYs, CheY₆ plus either CheY₃ or CheY₄¹, can support chemotaxis in *R. sphaeroides* [62]. Interestingly, mutation of the CheY₆ phosphorylatable aspartate to asparagine (D56N) produced a permanently stopped motor, whilst mutating it to alanine (D56A) simply rendered the strain motile but non-chemotactic. This is similar to the situation in *E. coli* where a D56N mutant permanently tumbles [109]. It was found that CheY₆(D56N) was stably phosphorylated at an alternative site, Ser-83 (conserved in all response regulators), by CheA₃. D53N

¹I.e. CheY₃ and CheY₄ perform the same role.

point mutants were also made independently in both CheY₃ or CheY₄, but no difference in stop frequencies were observed². It could be that a stopped phenotype (like *cheY*₆(D56N)) was not be observed because the signal could be bypassed by using the other available CheY. Thus a strain carrying a double mutation, *cheY*₃(D53N) *cheY*₄(D53N), was constructed and phenotyped.

Additional experiments centred on using a new (and untested) inducible expression plasmid (pIND4, made by Dr A.C. Ind). These tested whether overexpression of *cheY*₁, *cheY*₂, *cheY*₃, *cheY*₄, *cheY*₅, or *cheY*₆ (individually) increased the stop frequency of *R. sphaeroides*³ and whether CheY₃/CheY₄ have more or less of an effect than CheY₆. Before carrying out this work it was necessary to test the functionality of pIND4. Immunoblots were used to quantify the plasmid's output of CheY₃, CheY₄, and CheY₆. Comparisons were made between different plasmid inserts, IPTG concentrations and wild-type levels. The remaining work in this chapter used pIND4 to answer other questions. For example (a) do any of the CheYs have the same role (e.g. can overexpression of *cheY*₃ restore taxis in a *cheY*₆(D56A) strain) and (b) how is *R. sphaeroides* chemotaxis affected by the expression of *E. coli che* genes?

5.2 RESULTS

The results of this chapter were primarily derived from swim-plate and immunoblot assays of wild-type and *che* mutant strains (see Section 2.1 for methodology of how these mutants were made). Swim-plates and immunoblots were always carried out with cells growing in a micro-aerobic environment (see Sections 2.2.3 and 2.2.1 for full details), three replicates per strain. Swim-plates consisted of 0.25 % agar unless otherwise stated; graphs display the mean swim diameter plus/minus the standard deviation. We begin by examining the phenotype of strains that carry point mutants in the putative CheY-binding domain of FliM₁.

5.2.1 PHENOTYPES OF *fliM*₁ POINT MUTANTS

In *S. enterica* the CheY-binding domain of FliM is located at the N terminus, within residues 1 to 16 [110]. Mutations in the N-terminus of *S. enterica* FliM (FliM(L8I), FliM(S9Y), FliM(E12G) (numbers refer to residues in *R. sphaeroides fliM*₁; see Figure 1.12, Page 18 for sequence alignment) cause cells to switch less [111],

²D53 is the phosphorylation site of CheY₃ and CheY₄.

³In *E. coli*, CheY overexpression, causes a 'tumbly' phenotype due to exclusive CW rotation.

probably because they bind CheY-P less well than wild-type FliM [110]. However when the same mutations were made in *R. sphaeroides*, only FliM₁(S9Y) gave an obviously different phenotype; the strain migrated 80 % the diameter of wild-type on swim-plates and exhibited an increase in stop frequency, opposite to the effect in *S. enterica* [69]. The authors reasoned that in *R. sphaeroides* either the binding of CheY to FliM₁ promotes swimming and the absence of this interaction promotes a stop, or these mutations increased FliM₁–CheY binding rather than reducing it.

Conveniently three strains containing similar mutations at the start of *fliM*₁ were kindly donated by Prof R.E. Sockett to allow the experiments to be conducted using our methodology. Figure 5.1 shows how the mutants performed on swim-plates. *fliM*₁(E12Q) swims significantly further than WS8N ($P < 0.05$ ANOVA) and is thus said to ‘hyperswarm’. Hyperswarming has been observed in other bacteria such as *E. coli*, *V. cholerae*, *Proteus mirabilis* [112, 113], and *R. sphaeroides*⁴, but it is not known why it occurs.

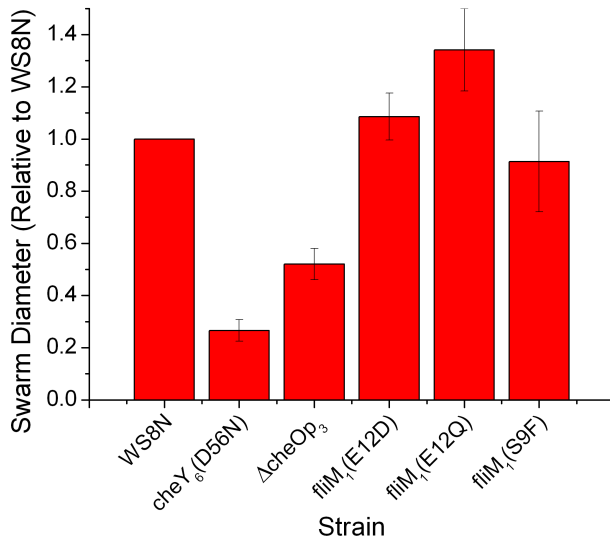


Figure 5.1: A comparison of swarm diameters of strains with mutations in *fliM*₁ (*fliM*₁(E12D), *fliM*₁(E12Q), *fliM*₁(S9F)). JPA1213 (*cheY*₆(D56N)) and JPA1301 (Δ*cheOp*₃) are non-motile and non-chemotactic controls respectively.

Whilst only *fliM*₁(E12Q) exhibits a hyperswarming phenotype ($P < 0.05$ ANOVA), when tested blind under a light microscope, both *fliM*₁(E12Q) and *fliM*₁(S9F) (but not *fliM*₁(E12D)) exhibited a swimming phenotype that was stoppier than WS8N (Figure 5.2, $P < 0.05$ Chi-Sq). In light of the findings of the previous chapter (that without chemotactic stimulation the motor rotates continuously) one predicts that the mutations FliM₁(E12Q) and FliM₁(S9F) have a higher affinity for binding CheY_x-P than wild-type FliM₁.

⁴Deletion of a gene encoding the McpJ chemoreceptor in *R. sphaeroides* (located at an unlinked locus) led to increased migration of 1.45 relative to WS8N in swim-plate assays (the growth rate, tethered and free-swimming behaviour of this strain was indistinguishable from wild-type) [114].

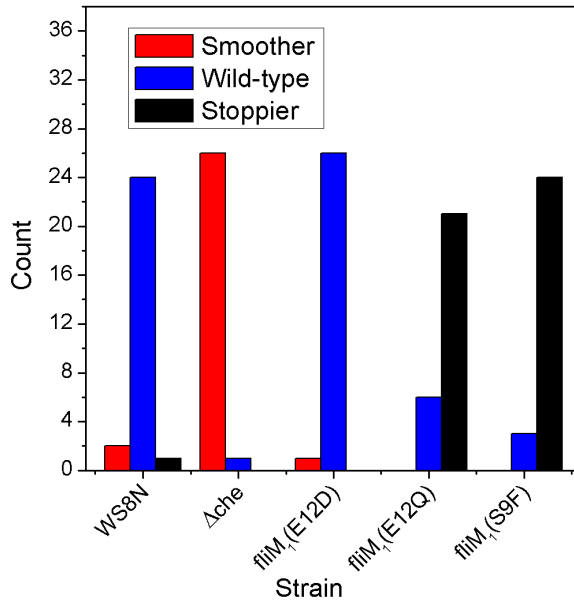


Figure 5.2: Free-swimming phenotypes of strains carrying *fliM*₁ point mutants (*fliM*₁(E12D), *fliM*₁(E12Q), *fliM*₁(S9F)), tested blind in capillary tubes using a light microscope. Their behaviour was marked on a scale of 1 = smoother than WS8N, 2 = indistinguishable from WS8N, 3 = stopper than WS8N. See Section 2.2.2, Page 43 for method. Only 5 of the 11 strains tested at the same time are shown. *fliM*₁(E12Q) and *fliM*₁(S9F) are significantly stopper than WS8N ($P < 0.05$ Chi-Sq).

Since *fliM*₁(E12Q) does not have a faster growth rate (no significant difference in doubling time, $P > 0.05$ ANOVA, Figure C.4, Page 127), it was hypothesised that the increased stop frequency could account for its migration further through 0.25 % agar. This could be due to the structure of the agar mesh i.e. it may be that taxis, coupled with a higher frequency of direction changes, is an advantage under these conditions as cells would waste less time trying to swim through agar blocks, as shown for *E. coli* [73]. It should have less of an effect in a liquid environment.

As a test, various strains were tested on swim-plates which varied in agar concentration from 0.20 %, which was as low as it was practical to go, to 0.55 % which was virtually solid. Figure 5.3 shows that *fliM*₁(E12Q) consistently outperforms WS8N at all tested agar concentrations. It was hoped that *fliM*₁(E12Q), which hyperswarms in 0.25 % agar, would exhibit a different relationship to WS8N in different per cent agar concentrations since that should select for different stop frequencies. Unfortunately it is impossible to conduct an assay with plates lower than 0.20 %. If one could, one may find that WS8N performs better than *fliM*₁(E12Q).

Thus it has not been possible to explain why *fliM*₁(E12Q) can outperform WS8N on swim-plates. Undoubtedly, first and foremost, the hyperswarming strain must be able to perform chemotaxis. However with this condition in place, an increased stop frequency may facilitate movement through the agar mesh, but further experiments are required to identify the mechanism.

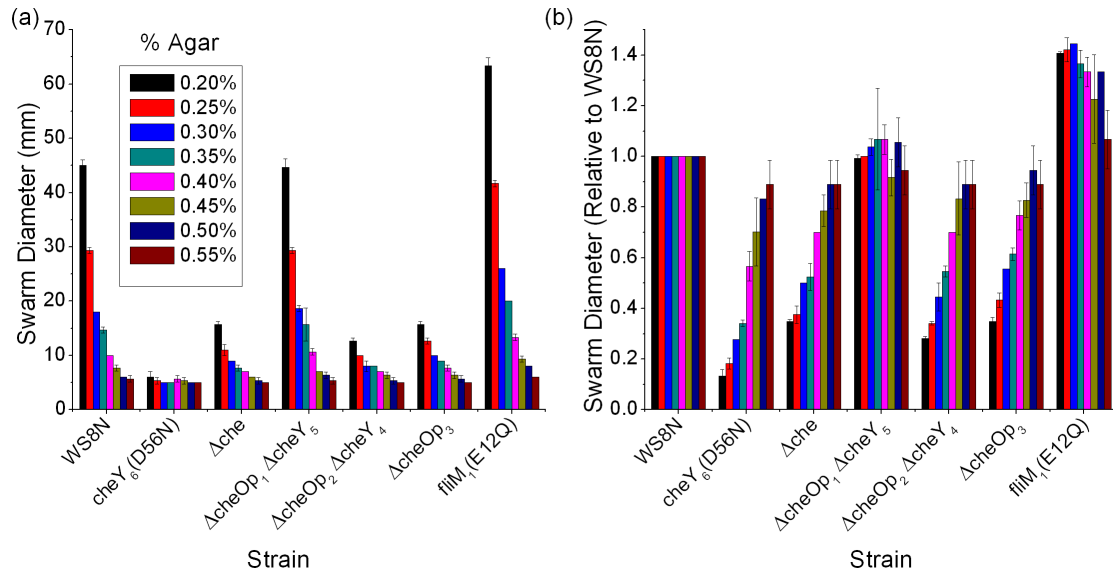


Figure 5.3: The migration of *fliM*₁(E12Q) relative to other strains on swim-plates of various agar concentrations; JPA1213 (*cheY*₆(D56N)), JPA1353 (Δche), JPA443 ($\Delta cheOp_1$ and $\Delta cheY_5$), JPA419 ($\Delta cheOp_2$ and $\Delta cheY_4$), and JPA1301 ($\Delta cheOp_3$). Graphs contain the same data but are plotted in real and relative units ((a) and (b) respectively).

5.2.2 PHENOTYPES OF *cheY*₃ *cheY*₄ POINT MUTANTS

Previously D53N phosphorylation site point mutations had been made independently in both *CheY*₃ or *CheY*₄, but no difference in stop frequencies were observed [62], perhaps because the signal could be bypassed via the other functional *CheY*. Thus strain JPA920 carrying the double mutation (*cheY*₃(D53N) *cheY*₄(D53N)) was constructed. JPA919 carrying a double mutation, *cheY*₃(D53A) *cheY*₄(D53A), was also constructed at the same time, phenotyped and used for further studies.

STRAIN CONSTRUCTION

JPA919 and JPA920 were made in two rounds. (1) pK18Y4D53A and pK18Y4D53N were used to independently transfer the mutant genes into the genome of JPA425 (*cheY*₃* $\Delta cheY_4$), making JPA917 (*cheY*₃* *cheY*₄(D53A)) and JPA918 (*cheY*₃*, *cheY*₄(D53N)) respectively.⁵ (2) The genes from pK18Y3D53A and pK18Y3D53N were then introduced into JPA917 and JPA918, to make JPA919 (*cheY*₃(D53A) *cheY*₄(D53A)) and JPA920 (*cheY*₃(D53N) *cheY*₄(D53N)) respectively.

The DNA from *cheY*₄ and *cheY*₃ transconjugants were digested with *Bsa*I and *Eco*RV respectively and screened by Southern blotting (Figure 5.4). Successful

⁵*cheY*₃* is an insertionally inactivated *cheY*₃ gene.

transconjugants were subject to PCR (using primers Y3-F/Y3-R and Y4-F/Y4-R (Appendix B.3, Page 124) for *cheY₃* and *cheY₄* respectively) and the products sequenced.

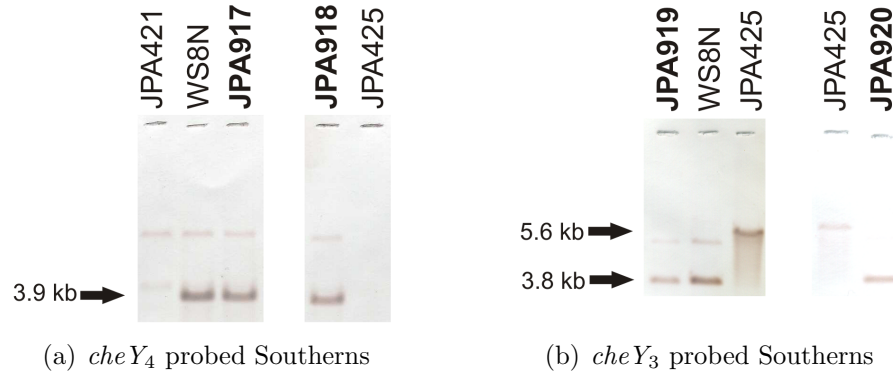


Figure 5.4: Southern blot analysis. (a) Round 1 - introducing *cheY₄* mutants into JPA425 (*cheY₃** Δ *cheY₄*). Blots were screened for the presence of the *cheY₄* gene fragment (3.9 kb). JPA421 is a Δ *cheY₄* control. (b) Round 2 - introducing *cheY₃* mutants into JPA917 and JPA918. This was not as simple as just looking for the presence of the *cheY₃* gene fragment; the background strains (JPA425 derivatives) carry a *cheY₃* gene that is functionally inactive (*cheY₃**). It was made by cloning a *Mlu*I linker (5'-GACGCGTC-3') into the *Eco*RV site near the beginning of *cheY₃* [82]. Thus *Eco*RV will cut in the wild-type and phosphorylation site mutant *cheY₃* genes giving a fragment size of 3.8 kb, but not in the insertionally inactivated gene, which gives a larger fragment of 5.6 kb. The probes were made by digesting pQEY4 with *Bam*HI/*Pst*I, and pQEY3 with *Eco*RI/*Hind*III.

PHENOTYPING

Unlike the *cheY₆*(D56N) strain (JPA1213), JPA920 (*cheY₃*(D53N) *cheY₄*(D53N)) was motile. In fact, when tested blind in capillary tubes, JPA920 showed significantly smoother swimming than WS8N (Figure 5.5, $P < 0.05$ Chi-Sq). However JPA919 (*cheY₃*(D53A) *cheY₄*(D53A)) was indistinguishable from WS8N. At present it is impossible to say why JPA920 is smoother than WS8N, there are simply too many unknowns (see discussion at the end of the chapter). It is known that CheA₂ can phosphorylate CheY₃(D53N) and CheY₄(D53N) at an alternative site but not CheY₃(D53A) and CheY₄(D53A) [62]; perhaps this may be part of the reason for different phenotypes of JPA919 and JPA920. Figure 5.6 shows that the *cheY₃* and *cheY₄* double mutants, JPA919 and JPA920, were non-chemotactic (doubling times were not significantly different from WS8N, $P > 0.05$ ANOVA, Figure C.4, Page 127). Next, immunoblots were used to quantify the cytoplasmic concentration of CheY₃, CheY₄, and CheY₆ in WS8N.

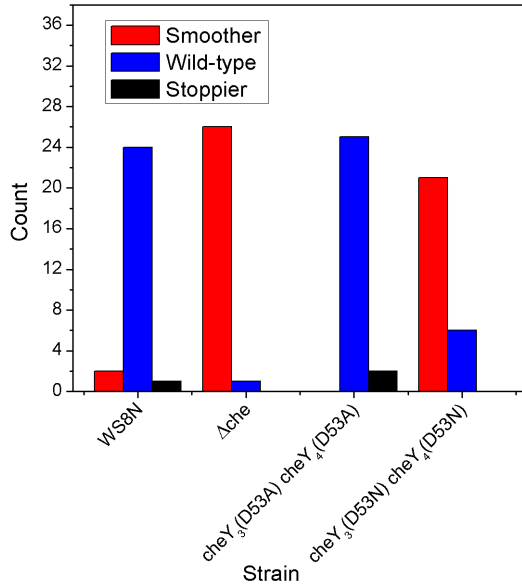


Figure 5.5: Free-swimming phenotypes of JPA919 (*cheY₃(D53A) cheY₄(D53A)*) and JPA920 (*cheY₃(D53N) cheY₄(D53N)*), tested blind in capillary tubes using a light microscope. Their behaviour was marked on a scale of 1 = smoother than WS8N, 2 = indistinguishable from WS8N, 3 = stopper than WS8N. See Section 2.2.2, Page 43 for method. Only 4 of the 11 strains tested at the same time are shown. JPA920 is significantly smoother than WS8N ($P < 0.05$ Chi-Sq).

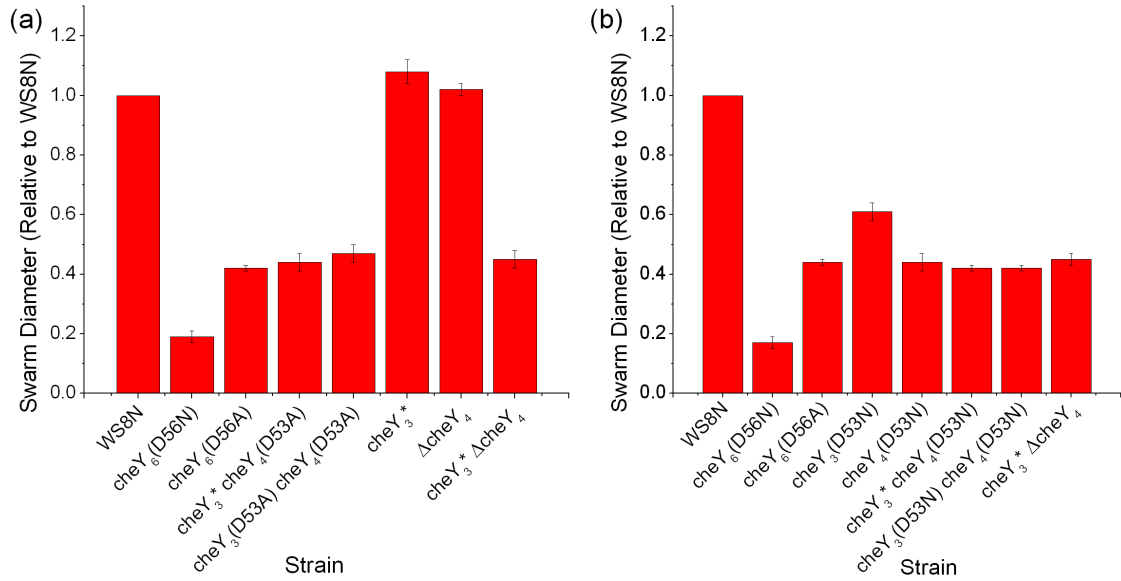


Figure 5.6: Swarm diameters of (a) D53A (JPA919 (*cheY₃(D53A) cheY₄(D53A)*)) and (b) D53N mutants (JPA920 (*cheY₃(D53N) cheY₄(D53N)*)) relative to WS8N. JPA917 (*cheY₃* cheY₄(D53A)*) and JPA918 (*cheY₃* cheY₄(D53N)*) are intermediate strains made after round 1 of strain construction. JPA1218 (*cheY₃(D53N)*) and JPA1220 (*cheY₄(D53N)*) migrate less than JPA410 (*cheY₃**) and JPA421 (*ΔcheY₄*). Furthermore JPA1220 (*cheY₄(D53N)*) abolishes taxis completely whilst it is just reduced in JPA1218 (*cheY₃(D53N)*). A similar pattern was observed when *cheY₃/cheY₄* mutants are overexpressed in WS8N (Figure C.2, Page 126).

5.2.3 COPY NUMBERS OF CHEY_{3/4/6} PER CELL

Immunoblots were used to assess the cytoplasmic concentration of CheY₃, CheY₄, and CheY₆, in *R. sphaeroides*, grown under micro-aerobic conditions. Initially, semi-quantitative immunoblots were carried out to ensure the proteins detected were of the correct size and that antibodies bound in a concentration-dependent manner (Figure 5.7). Then quantitative immunodotblots were used to estimate CheY₄ and CheY₆ concentrations more accurately (good standard curves from protein standards were obtained since more replicates could be included per blot). Unfortunately, due to the poor specificity of the α -CheY₃ antibody (Figure C.7, Page 129), this method could not be used to estimate CheY₃ concentration, despite using acetone powder from the deletion strain in an attempt to reduce non-specific binding. Thus CheY₃ concentration was estimated from semi-quantitative immunoblots. Table 5.1 summarises the data revealing major differences in expression levels. There is approximately 20 times more CheY₆ in the cytoplasm than CheY₄. Figure 5.8 compares these values to the known copy number of other Che proteins in *R. sphaeroides* and *E. coli*. The high values of CheA₂, CheB₁, and CheY₆ stand out against other components. Possible explanations for variations in copy number within the same operon are discussed at the end of the chapter.

Protein	n	Mean copies per cell	SE
CheY ₃	4	<1,000*	n/a
CheY ₄	12	2,900	800
CheY ₆	12	58,000	8,000

Table 5.1: Copy numbers of CheY₃, CheY₄ and CheY₆ in micro-aerobically grown WS8N. *Note that CheY₃ protein standards of 0.1 ng/ul were detectable via semi-quantitative immunoblots (corresponding to 1,197 copies of CheY₃ per cell). CheY₄ and CheY₆ concentrations were determined using quantitative immunodotblots. The values from the quantitative immunodotblots agree with estimates obtained with the semi-quantitative immunoblots where CheY₄ \approx 0.35 ng/ μ l = 4262 copies/cell and CheY₆ \approx 4 ng/ μ l = 43,960 copies/cell.

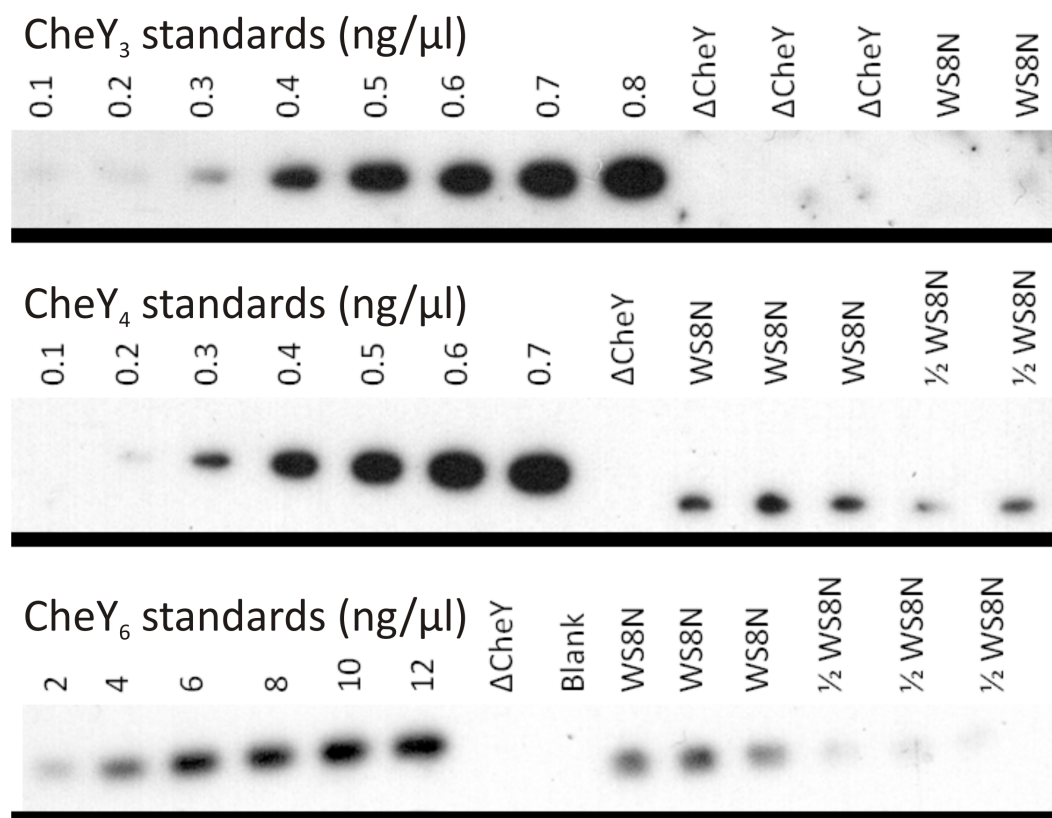


Figure 5.7: Semi-quantitative immunoblots to estimate CheY₃, CheY₄ and CheY₆ copy numbers in micro-aerobically grown WS8N. Primary antibody dilutions and exposure times were as follows; CheY₃ (1/500, 47 min), CheY₄ (1/2,000, 32 min), CheY₆ (1/10,000, 1 min). Δche refers to JPA1353. Note that although here it looks as if there may be no *cheY₃* expression at all, a strain carrying *yfp-cheY₃* does fluoresce above background levels (albeit with long exposure times) [62]. See Figure C.7, Page 129 for non-cropped western blots.

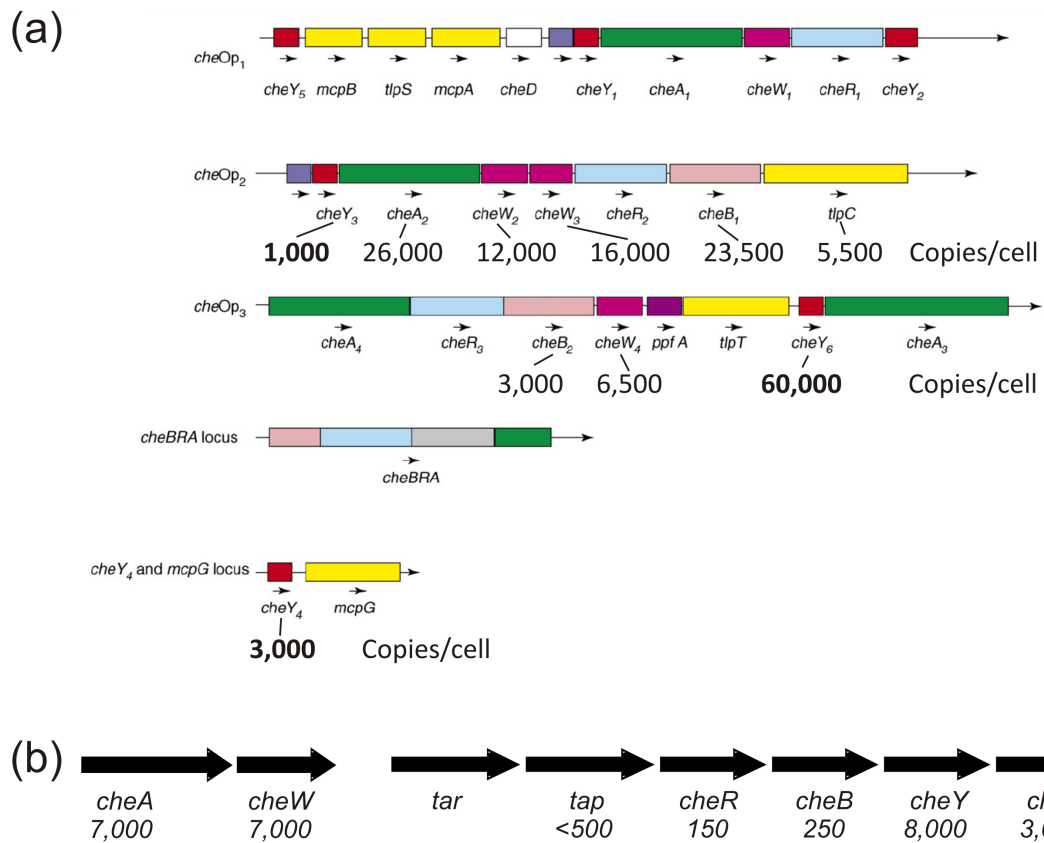


Figure 5.8: Copy numbers of Che proteins in (a) *R. sphaeroides* and (b) *E. coli*. (a) Copy number of important CheYs (bold) relative to other Che proteins tested in WS8N grown under the same conditions (micro-aerobically). Numbers not in bold were taken from [115]. (b) Copy number of *E. coli* proteins (encoded in two operons) for comparison, from [116].

5.2.4 PROTEIN QUANTIFICATION FROM pIND4

The stopping frequency of strains carrying *cheY* deletions are not obviously different from WS8N [62]. Thus in this study, an alternative approach was used; does overexpression of *cheY*₁, *cheY*₂, *cheY*₃, *cheY*₄, *cheY*₅, or *cheY*₆ increase the stop frequency?⁶ This technique has been used to show that only CheY₃ of the five CheYs in *Vibrio cholerae* directly controls flagellar rotation [117] and that a single CheY homologue controls both the bidirectional polar and unidirectional lateral flagellar motors of *V. alginolyticus* [108].

cheY genes and phosphorylation site mutants were amplified by PCR and cloned into pIND4 at the *NcoI* site situated downstream of the *lac* promoter and Shine-Dalgarno sequence. The plasmids were then transferred by conjugation into several strains, resulting in over a hundred combinations.

Before reviewing the phenotypes it is useful to know how much protein the plasmid produces at various inducer (IPTG) concentrations using quantitative immunodotblots as before. This work demonstrates the plasmid's capabilities and will shortly contribute to a paper describing the construction of pIND4 [93].

Strains containing appropriate plasmids were used to inoculate succinate medium containing kanamycin and appropriate IPTG concentrations. Cultures were left shaking overnight at 30 °C and spun down when they reached OD₇₀₀ = 0.6 (see Section 2.2.1 for full method). This meant that both the time spent in the presence of IPTG (~14 h) and the OD₇₀₀ for each sample when harvested, could be kept constant.

Table 5.2 and Figure 5.9 shows the output of CheY₄ and CheY₆ from the plasmid. Quantitative immunodotblots on CheY₃ samples were attempted but failed to give any signal over the high background. As in the wild-type levels, vastly more CheY₆ was produced than CheY₄ at all levels of induction.

Plasmid/Strain	IPTG (μ M)	CheY ₄ copies/cell Mean \pm SE (n)	CheY ₆ copies/cell Mean \pm SE (n)
pIND-empty/WS8N	0	2,900 \pm 800 (12)	58,000 \pm 8,000 (12)
pIND-Y/JPA1353	0	1,500 \pm 600 (6)	59,300 \pm 11,600 (10)
pIND-Y/JPA1353	50	43,900 \pm 8,400 (6)	90,500 \pm 6,400 (12)
pIND-Y/JPA1353	1,000	61,600 \pm 6,600 (12)	479,400 \pm 21,500 (10)

Table 5.2: Copy number of CheY₄ and CheY₆ per cell when expressed from pIND4.

⁶Note that *cheY*₁, *cheY*₂, and *cheY*₅ were tested despite not being expressed under lab conditions.

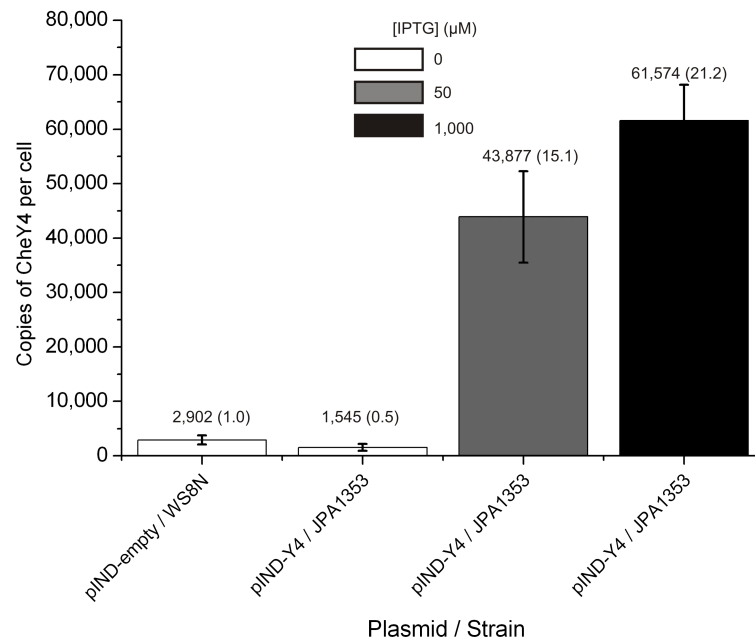
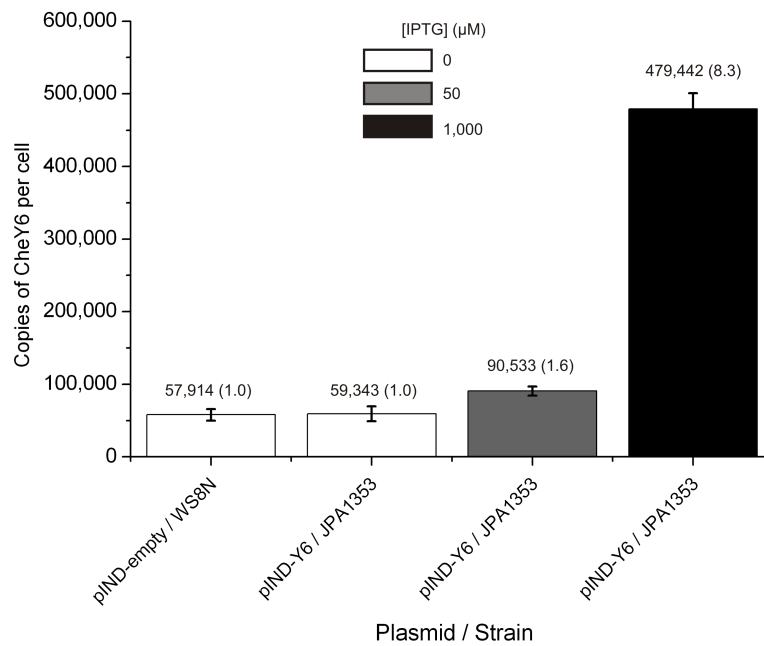
(a) Copy number of CheY₄ per cell(b) Copy number of CheY₆ per cell

Figure 5.9: Copy number of CheY₄ and CheY₆ per cell when expressed in pIND4 following 14 h exposure to set concentrations of IPTG (0, 50 and 1,000 μM ; these concentrations were chosen after conducting swim-plate analysis). The very low background from pIND-empty/JPA1353 control was accounted for in the analysis. The numbers in brackets refer to the copy numbers per cell relative to wild-type levels. Note the very different y-axis scales. The plasmid clearly shows that increasing IPTG concentrations lead to increasing protein output.

5.2.5 $\Delta cheY_6$ COULD NOT BE COMPLEMENTED

The completion of pIND4 meant that strains could be checked to make sure their phenotypes can be complemented. pIND4 was used to express the wild-type version of a gene that is deleted/mutated in the mutant strain.

Figure 5.10 shows that the $\Delta cheY_6$ strain (JPA1336) could not be complemented, but two $cheY_6$ point mutants could. Complementation of the two point mutants shows that the plasmid worked i.e. the presence of CheY₆ from the plasmid compensated for the mutant CheY₆ protein encoded in the genome. However in strain JPA1336 the presence of CheY₆ from the plasmid was insufficient to recover wild-type taxis. This suggests that the non-chemotactic phenotype of JPA1336 is caused by something in addition to the absence of the $cheY_6$ gene i.e. deletion of that region of DNA not only abolishes $cheY_6$ expression but changes something else as well. Since it is well-known that manipulating DNA at one site can have effects on the expression of downstream genes the expression of $cheA_3$ (located immediately downstream of $cheY_6$, Figure 5.8, Page 77) was investigated. Figure 5.11 showing that the expression of $cheA_3$ is reduced (if not abolished) in JPA1336 explaining why this strain could not be complemented by expression of $cheY_6$ alone.

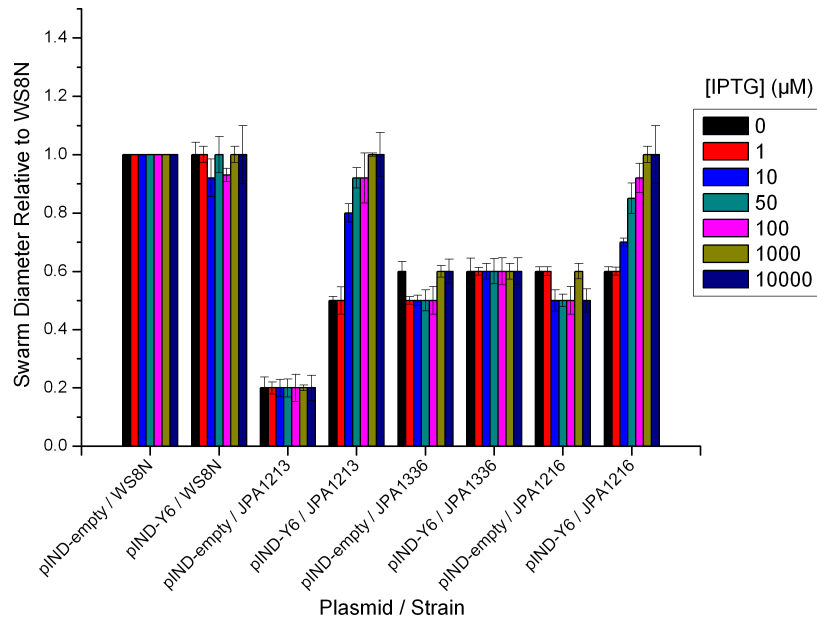


Figure 5.10: A comparison of swarm diameters of strains hosting pIND-Y6 (and pIND-empty controls) exposed to various IPTG concentrations. JPA1213 ($cheY_6$ (D56N)) is non-motile, JPA1336 ($\Delta cheY_6$) and JPA1216 ($cheY_6$ (D56A)) are non-chemotactic. Both $cheY_6$ point mutants could be complemented (JPA1213 and JPA1216) but $\Delta cheY_6$ could not. Leaky expression (0 μ M IPTG) is enough to recover motility in JPA1213. Note only expression of $cheY_6$ and not the other $cheY$ s, have this effect (Figure C.3, Page 127).

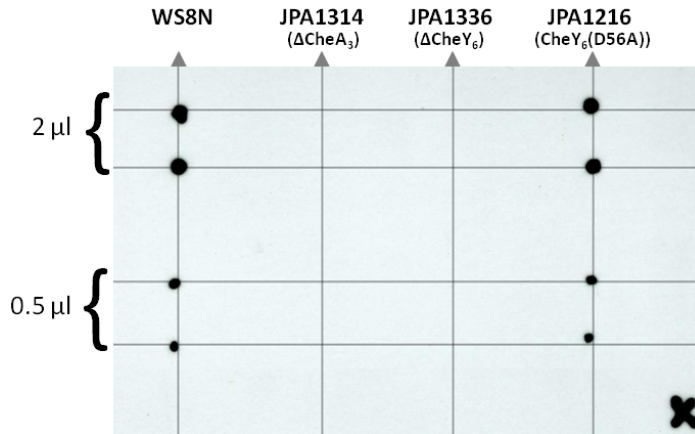


Figure 5.11: An immunodot blot probed with α -CheA₃ shows that the expression of *cheA₃* in two independent samples is reduced/undetectable in JPA1336. Primary antibody concentrations and exposure times were 1/10,000 and 2 min respectively.

Figure 5.10 also shows that overexpression of *cheY₆* can restore motility and taxis in the permanently stopped *cheY₆*(D56N) strain (JPA1213). It is known that the phosphotransfer from CheA₃ to CheY₆(D56N) is much slower than to wild-type CheY₆; similarly, auto-dephosphorylation of CheY₆(D56N)-P occurs at a much slower rate [62]. Thus it is likely that in the presence of wild-type CheY₆, CheY₆(D56N) proteins do not get phosphorylated, hence relieving the permanently stopped motor phenotype. This experiment highlights the advantage of making point mutants over gene knock-outs. It also dictated how future experiments were conducted; it was impractical to repeat each experiment with 7 different IPTG concentrations. Instead 0, 50 and 1,000 μ M concentrations were chosen as low, middle and high values respectively.

5.2.6 CHEY₅ IS FUNCTIONALLY EQUIVALENT TO CHEY₃/CHEY₄

pIND4 was used to test how the expression of various *cheY* genes in various backgrounds effected migration on swim-plates. The aim was to find out more about the roles of the different CheY proteins.

The first experiment was to express all the *cheY* genes in a WS8N background to identify which proteins if any, could interfere with wild-type taxis when overexpressed (Figure 5.12).

Surprisingly *cheY*₆ overexpression (~ 8 times more CheY₆ in the cytoplasm than WS8N) had no effect. However overexpression of *cheY*₃ and *cheY*₄ did reduce wild-type taxis. Overexpression of *cheOp*₁ encoded genes, *cheY*₁ and *cheY*₂, did not reduce wild-type taxis, but expression of *cheY*₅ did.

CheY₅ overexpression reduced taxis more than CheY₃ overexpression, but less than CheY₄ overexpression. It is possible that the differences observed here are due variations in the output of the plasmid depending on its insert, rather than differences in the actions of the proteins themselves (note the quantification of CheY₅ was not determined because no antibody was available).

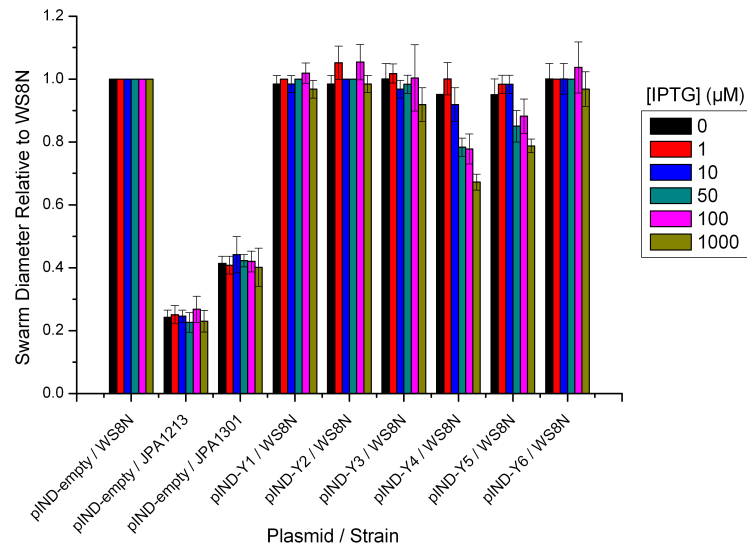


Figure 5.12: Swim-plates used to assess the effects of overexpressing *cheY* genes from pIND4 in WS8N. The swarm diameters show that overexpression of *cheY*₄, *cheY*₅, and to a small extent *cheY*₃, interfere with wild-type taxis, whilst the other CheYs do not. *cheY*₆(D56N) (JPA1213) and Δ *cheOp*₃ (JPA1301) served as non-motile and non-chemotactic controls respectively.

Figure 5.13 shows that overexpression of *cheY*₅ can restore taxis in JPA919 (*cheY*₃(D53A) *cheY*₄(D53A)), just like expression of *cheY*₃ or *cheY*₄. Thus, despite

their locations in the genome (*cheY₃* in *cheOp₂* and *cheY₅* in *cheOp₁* on CI, *cheY₄* on CII), it seems the products of *cheY₃*, *cheY₄*, and *cheY₅* are functionally interchangeable. Note that CheY₃, CheY₄, and CheY₅ share 69–75 % sequence identity and many conserved residues (Table 1.2 and Figure 1.11, Pages 17 and 18).

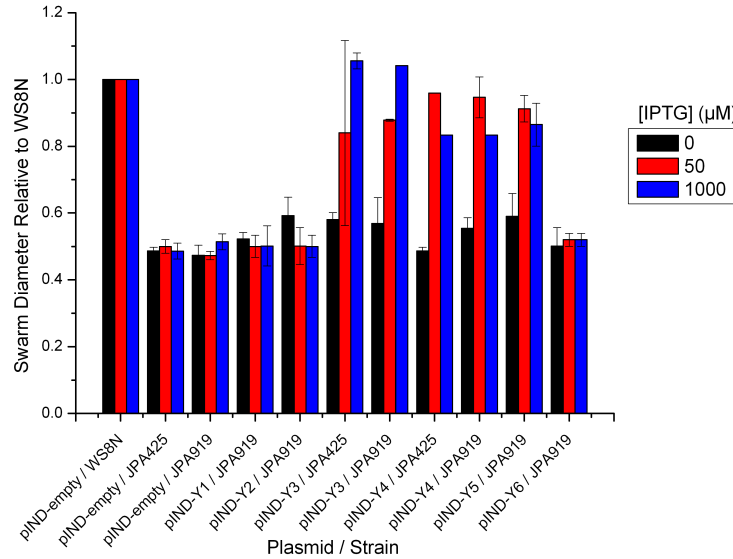


Figure 5.13: Overexpression of *cheY₃*, *cheY₄*, and *cheY₅* from pIND4 can restore taxis in JPA919 (*cheY₃*(D53A) *cheY₄*(D53A)). Overexpression of *cheY₃* or *cheY₄* can also restore taxis in JPA425 (*cheY₃** Δ *cheY₄*) (and JPA1025 (Δ *cheY₁* Δ *cheY₂* Δ *cheY₃* Δ *cheY₄* Δ *cheY₅*), data not shown).

It is intriguing that CheY₅ encoded by *cheOp₁*, has the potential to function in the pathway controlling the fla1 flagellum. This implies that the chemotaxis pathway which controls the fla1 flagellum may have the potential to function in the chemotaxis pathway controlling the fla2 flagella. Whilst it has been shown (through construction of deletion mutants) that *cheY₃*, *cheY₄*, and *cheY₆* are not essential for taxis in a strain expressing fla2 flagella [72], it is unknown if they could interfere with the control of fla2, if expressed. Similarly, deletion of *cheY₅* has never been shown to be important in WS8N (swimming using the fla1 flagellum) [62]. The reason that this has not been obvious before (by studying the phenotypes of deletion mutants) is that it is dependant on the gene being expressed (*cheY₅* is expressed with fla2 flagella; *cheY₃* and *cheY₄* are expressed with the fla1 flagellum).

It is tempting to hypothesise that CheY₃, CheY₄, and CheY₅ all play exactly the same role in the chemotaxis pathway of *R. sphaeroides*, regardless of which flagella set is being used. Their high-sequence similarity and functionality suggest that the binding targets of CheY₃, CheY₄, and CheY₅ are likely to be the same. The future task is to identify which protein(s), if any, they bind to following phosphorylation.

5.2.7 EFFECT OF EXPRESSION OF *E. coli* GENES ON *R. sphaeroides* BEHAVIOUR

Although highly unlikely, is the *R. sphaeroides* flagellar motor unidirectional because its CheYs make it stop rather than switch? Would binding of a CheY from a species which employs a bi-directional motor, cause the *R. sphaeroides* to switch? The wild-type *E. coli* *cheY* gene, along with two mutants (CheY(D13K) and CheY(D13K Y106W)) that are considered constitutively active and cause an enhanced CW-bias in *E. coli*, were cloned into pIND4. CheY(D13K Y106W) is referred to as CheY**. Both mutants (CheY(D13K) and CheY**) do not differ in structure much from unphosphorylated CheY [118, 119] but CheY** exhibits enhanced FlhM binding over CheY-P [120]. In addition, *cheZ* (and *cheYcheZ* as encoded on the genome) were cloned into pIND4 to see if they effected *R. sphaeroides* taxis.

Figure 5.14 shows the effect of expressing these *E. coli* genes in *R. sphaeroides*, assessed using swim-plates. Expression of *cheY*, *cheZ*, or *cheYZ* did not effect wild-type taxis at all. This implies that the products of these genes do not interact with the chemotaxis pathway, therefore they must not accept phosphoryl groups from the native system. However the presence of CheY(D13K) and CheY** did interfere with wild-type taxis. CheY** (which has a stronger CW-bias phenotype than CheY(D13K) in *E. coli*) has a more detrimental effect than CheY(D13K). Note *E. coli* CheY shares 32–39 % sequence identity with the *R. sphaeroides* CheYs (Table 1.2 and Figure 1.11, Pages 17 and 18).

To test whether CheY** was interfering with *R. sphaeroides* chemotaxis pathway, the plasmids were tested in a JPA1353 (Δche) background. Since the same pattern was observed (Figure 5.14(b)) it suggests that CheY** does not interfere with the chemotaxis pathway, but is likely to be interacting with the *R. sphaeroides* motor directly. The doubling time of pIND-ecY** / JPA1353 was not significantly different from pIND-empty / JPA1353 ($P > 0.05$ ANOVA, Figure C.5 and C.6, Page 128).

There was no visible difference in the free-swimming stop frequency when CheY** was maximally overexpressed in WS8N or JPA1353. Therefore the bead assay was used to investigate the motor output of pIND-ecY** / JPA1353 following ~ 14 h induction with 1 mM IPTG. Beads (0.83 μm diameter) rotated in the same direction and at similar speeds as the parental strain. It is therefore unclear why migration is reduced on swim-plates.

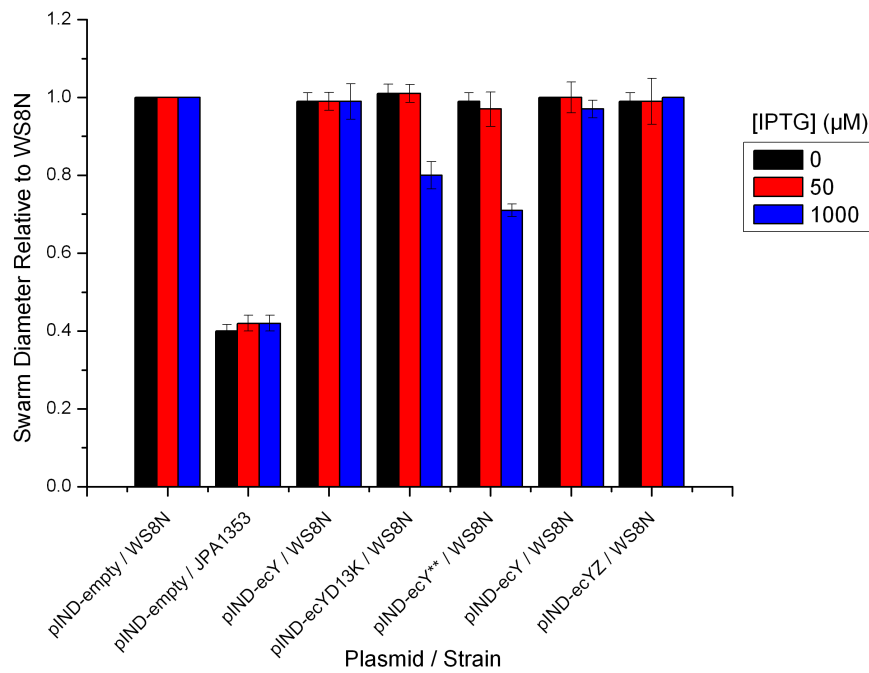
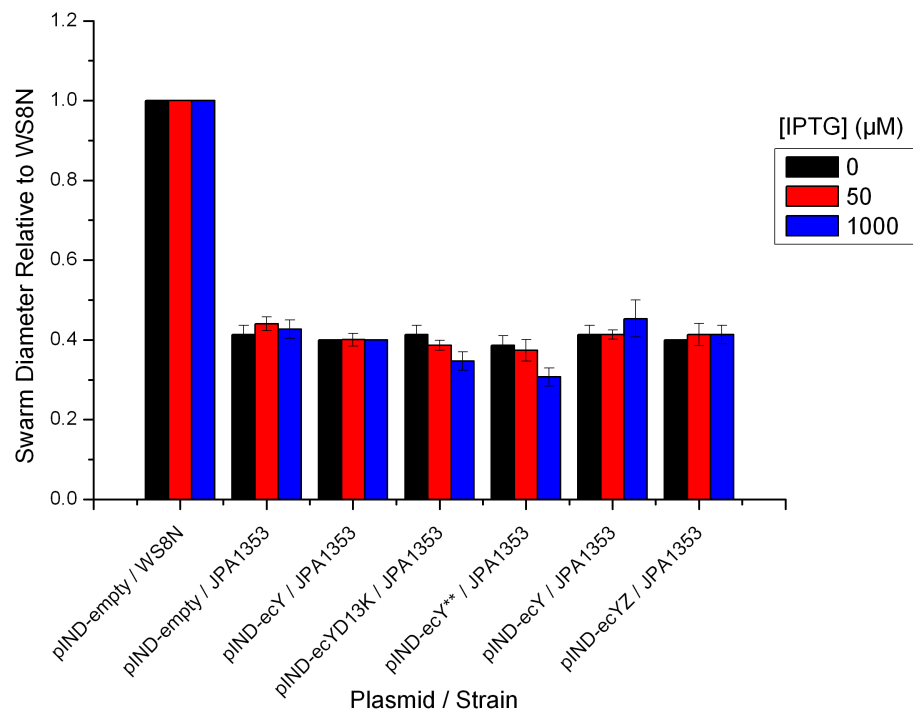
(a) *E. coli* gene expression in WS8N(b) *E. coli* gene expression in JPA1353 (Δche)

Figure 5.14: Effect of expressing *E. coli* genes on *R. sphaeroides* taxis and motility. The presence of CheY(D13K) and CheY** reduce wild-type taxis in an IPTG-dependent manner, whilst the presence of CheY, CheZ and CheYZ, do not effect taxis at all. A similar pattern was observed when they are expressed in JPA1353 (Δche).

5.2.8 STOP FREQUENCIES OF STRAINS OVEREXPRESSING CHEYS

Does overexpression of each individual *cheY* increase the stop frequency? Table 5.3 shows the effect of overexpressing each *cheY* plus phosphorylation site mutants in WS8N and JPA1353, assessed by examining free-swimming phenotypes in capillary tubes. Other than overexpression of *cheY*₆ (and *cheY*₆(D56A) and *cheY*₆(D56N)), no other *cheY* genes affected the swimming phenotypes of WS8N/JPA1353. But this is not proof that CheY₃ and CheY₄ cannot stop the motor as the copy numbers of proteins present are so different (Table 5.2, Page 78). At 0 mM IPTG for *cheY*₆, and 1 mM IPTG for *cheY*₄, concentrations are comparable (60,000 copies/cell each), but at 0 mM IPTG, pIND-Y6 in either WS8N or JPA1353 does not give a different phenotype from the background strain. Thus, this simple test was left incomplete.

Plasmid	Phenotype in WS8N	Phenotype in JPA1353
pIND-empty	wild-type	smoother
pIND-Y1	wild-type	smoother
pIND-Y2	wild-type	smoother
pIND-Y3	wild-type	smoother
pIND-Y3D53A	wild-type	smoother
pIND-Y3D53N	wild-type	smoother
pIND-Y4	wild-type	smoother
pIND-Y4D53A	wild-type	smoother
pIND-Y4D53N	wild-type	smoother
pIND-Y5	wild-type	smoother
pIND-Y6	stoppier	wild-type
pIND-Y6D56A	stoppier	wild-type
pIND-Y6D56N	non-motile	non-motile

Table 5.3: Stop frequency phenotypes of WS8N and JPA1353 overexpressing *che* genes and phosphorylation site mutants from pIND4. Samples were examined blind in capillaries (see Section 2.2.2 (top paragraph only) for method) after 14 h growth with 1 mM IPTG and marked as ‘non-motile’, ‘stoppier’, ‘wild-type’, or ‘smoother’, relative to WS8N. The process was repeated with another two replicates of each strain; the predominant phenotype is shown. Note that at 50 μ M IPTG, pIND-Y6/JPA1353 was clearly more stoppy than pIND-Y6D56A/JPA1353.

5.3 CONCLUSIONS

This chapter has been concerned with extending our knowledge of the terminal end of the chemotaxis pathway in *R. sphaeroides*; the interaction between CheY and FliM proteins. There are a number of conclusions with testable predictions that have arisen from the findings of this chapter.

PHENOTYPES OF STRAINS CARRYING GENOMIC MUTATIONS

Two strains with point mutations in *fliM*₁ (*fliM*₁(E12Q) and *fliM*₁(S9F)) exhibited a significantly increased free-swimming stop frequency than wild-type. It is likely that these mutant FliM₁ proteins have a higher affinity for binding CheY_x-P than wild-type FliM₁. This would be consistent with the finding of the previous chapter, that CheYs stop the motor when phosphorylated.

It was also found that the *cheY*₃(D53N) *cheY*₄(D53N) strain stopped less than wild-type, whilst the free-swimming phenotype of the *cheY*₃(D53A) *cheY*₄(D53A) strain was indistinguishable from wild-type. CheA₂ can phosphorylate CheY₃(D53N) and CheY₄(D53N) at an alternative site, but not CheY₃(D53A) and CheY₄(D53A) [62]. If we assume the actions of the phosphorylated D53N mutant proteins are the same as phosphorylated wild-type proteins (as just shown with CheY₆), the question can be posed - why does the acceptance of phosphoryl groups by CheY₃/CheY₄ reduce the number of stops? Three possible answers are outlined below.

1. CheY₃-P/CheY₄-P occupy the CheY₆-binding site at the motor, but do not cause a stop. Less CheY₆-P binding equates to a reduced stop frequency.
2. Phosphotransfer from CheA₂ to CheY₃/CheY₄ results in reduced phosphotransfer from CheA₂ to CheY₆, resulting in a lower level of CheY₆-P and a reduced stop frequency.
3. Phosphotransfer from CheA₂ to CheY₃/CheY₄ results in reduced phosphotransfer from CheA₂ to CheB₁. Lower CheB₁-P levels reduce the sensitivity of CheA₄ to phosphorylate CheA₃ via TlpC⁷. Reduced CheA₃-P levels lead to reduced levels of CheY₆-P and a reduced stop frequency.

All three of these hypotheses are compatible with what is currently known about *R. sphaeroides* chemotaxis, including the need for *cheOp*₂ and *cheOp*₃ components

⁷TlpC is the only known protein encoded in *cheOp*₂ to localise to the cytoplasmic cluster, encoded immediately downstream of *cheB*₁.

to interact with one another. It is left to future research to determine which, if any, is the correct hypothesis.

COPY NUMBER OF CHEYS - FROM THE GENOME AND pIND4

Genomic expression levels of *cheY₃*, *cheY₄*, and *cheY₆* in WS8N were determined. Under the conditions tested, their expression levels varied greatly; CheY₃ and CheY₄ levels are low ($<1,000$ and $2,900 \pm 800$ respectively), and CheY₆ levels are very high ($58,000 \pm 8,000$). The sequences of *cheY₃*, *cheY₄*, and *cheY₆* were examined for codon usage and Shine Dalgarno sequences as possible sources of variation. Figure C.8 (Page 130) shows that the codon usage of *cheY₃*, *cheY₄* and *cheY₆* differs by 15, 11 and 10 % respectively from the average codon usage for the genome; the per cent similarities do weakly correlate with amount of protein present. It is unlikely that the variation in copy number is due to the strength of each gene's Shine Dalgarno sequence as (i) all three Shine Dalgarno sequences are strong (Figure C.8) and (ii) pIND4 output mimics that of the genome (in pIND4 the genes are cloned downstream of the same Shine Dalgarno sequence). Without carrying out further experiments it is impossible to identify where this variation in copy number originates, be it in rate of synthesis/degradation of the RNA transcript or the rate of synthesis/degradation of the protein itself. A recent article reveals that the degree of folding of the RNA transcript at the 5' end has a particularly influential role in determining final protein copy number [121]. Folding at the 5' end obstructs translation initiation. In addition, as less ribosomes bind, the transcript is more exposed to digestion by ribonucleases e.g. RNase II.

Comparing the copy numbers to *E. coli che* proteins highlights CheY₆ as being particularly high rather than CheY₃ and CheY₄ being particularly low. Is $\sim 60,000$ copies per cell for CheY₆ suspiciously high? As a comparison, in *E. coli*, some proteins e.g. FepA (a Ton-B dependent receptor) are present in the region of 80,000–90,000 copies per cell [122]. Note that the cell volume of *E. coli* (1×10^{-15} l, http://redpoll.pharmacy.ualberta.ca/CCDB/cgi-bin/STAT_NEW.cgi) is approximately double that of *R. sphaeroides* (0.48×10^{-15} l, S.L. Porter, personal communication). In *R. sphaeroides*, RuBisCO (ribulose-1,5-bisphosphate carboxylase oxygenase) can be present in 165,600 copies per cell under certain growth conditions [123]. Even though the RuBisCO level is 2.5–3 times that of CheY₆, it is surprising the difference is not greater given RuBisCO's importance. In addition, when maximally overexpressed from pIND4, CheY₆ levels reached nearly 500,000 copies per cell. Again as a crude comparison, when overexpressed in a designated

E. coli expression system (pQE30 vector in M15pREP4 cells), CheY₆ is present at 800,000 copies per cell (although this may be an underestimate since one assumed 100 % of the protein present in *E. coli* was purified). Again, it is surprising that the difference in output from pIND4 in *R. sphaeroides* and the optimised expression system in *E. coli* is not greater.

In conclusion the copy number of CheY₆ does seem very high. However the errors are reasonable ($58,000 \pm 8,000$ for genomic levels, $479,400 \pm 21,500$ for pIND4 maximum IPTG), the method is robust and reliable ($n = 12$ for both genomic and pIND4 values; four replicates of three independent samples), and the α -CheY₆ antibody is superb (see Figure C.7, Page 129). The numbers are also compatible with the surprising observation that *cheY*₆ overexpression does not disrupt wild-type chemotaxis (Figures 5.10 and 5.12) if one argues that the addition of more protein to a pool of protein that is already present in high concentrations is likely to have less of an effect than if the protein was present in low concentrations. In addition, the ~ 10 -fold increase in copy number of CheY₆ versus the rest of *cheOp*₃ maybe due to the presence of an internal promoter inbetween *tlpT* and *cheY*₆, as suggested previously [115].

Together with CheY₆, CheA₂ and CheB₁ also stand out as having particularly high copy numbers. Initially it seems surprising that the histidine protein kinase CheA₂, is present at 26,000 copies per cell, whilst the response regulators CheY₃ and CheY₄, are only present at $<1,000$ and 3,000 copies per cell respectively. In *E. coli* for instance, the copy number of CheA and CheY are closely matched at 7,000 and 8,000 copies per cell respectively [116]. However it is important to consider that in addition to CheY₃ and CheY₄, CheA₂ can also phosphorylate CheY₆ (as well as CheB₁ and CheB₂), thus restoring the kinase to response regulator copy number balance. Perhaps the high cytoplasmic concentration of these components (CheY₆, CheA₂ and CheB₁) are required to ‘drown-out’ signals from other chemotaxis components. This may have been one of the necessary changes that occurred in order to maintain a functioning chemotaxis network, following the acquisition of a new operon by lateral gene transfer. Regardless of the reasons, this information should be incorporated into any working model of *R. sphaeroides* chemotaxis.

In carrying out these experiments, expression from pIND4 was shown to be IPTG dependent and a standard lab procedure for using pIND4 was established. This involved experimenting with different IPTG levels, induction times and quantification methods. The results of the first swim-plates dictated how the samples were prepared for protein quantification. Leaving cells to grow for as long as possible (~ 14

h) in appropriate IPTG concentrations, mean that the protein quantification data can be applied to the swim-plate data.

SWIM-PLATE DATA

Although overexpression of *cheY*₆ did not complement the non-chemotactic phenotype of a $\Delta cheY_6$ strain, *cheY*₆ overexpression could restore the non-chemotactic phenotype of *cheY*₆(D56A) proving that the pIND-Y6 construct was functional and that CheY₆ is still essential for chemotaxis. It was shown that the $\Delta cheY_6$ strain could not be complemented due to polar effects of the in-frame deletion of *cheY*₆ on *cheA*₃ expression levels. This highlights the importance of checking that deletion mutants do not have polar effects.

Complementation studies also revealed that CheY₃, CheY₄, and CheY₅ are functionally equivalent. It was already strongly suspected that CheY₃ and CheY₄ performed the same role in controlling the fla1 flagellum [62]. However it is surprising that CheY₅, encoded in *cheOp*₁, can also function in the pathway controlling the fla1 flagellum because it has recently been shown that the CheYs encoded in *cheOp*₁ (CheY₁, CheY₂, CheY₅) are all required for control of the fla2 flagella [72]. Hence cross-talk will occur if *cheOp*₁ is ever expressed at the same time as *cheOp*₂/*cheOp*₃; CheA₂ will phosphorylate all the CheYs, CheA₃ will phosphorylate CheY₁ and CheY₆. CheY₅ most likely performs the same role in controlling the fla2 flagellar set, as CheY₃ or CheY₄ do in controlling the fla1 flagellar set. Despite efforts made in this chapter, this role remains to be elucidated.

In light of these data and the existence of *flim*₂ from the fla2 flagellar set, it seems increasingly unlikely that CheY₁₋₆ bind to FliM₁ with approximately equal affinities as stated previously [67]. More *in vitro* binding assays should be conducted with CheY₁₋₆ and FliM₁/FliM₂. It would also be interesting to see if *E. coli* CheY (or CheY**) could interact with the *R. sphaeroides* FliM proteins, since the swarm diameters of JPA1353 are reduced by *cheY*** overexpression.

STOP FREQUENCIES OF STRAINS OVEREXPRESSING CHEY PROTEINS

Unfortunately, the simple technique of overexpressing *cheY*s to determine their motor-stopping capabilities was inconclusive, due to the large variation in expression levels between the different proteins from pIND4. However the experiment did support two previous hypotheses. Firstly, that CheY₆ can stop the motor, since stop

frequency increased when *cheY*₆ was expressed in WS8N or JPA1353.⁸ And secondly, that the motor-stopping capability of CheY₆ is enhanced when phosphorylated, since at 50 μ M IPTG induction, a JPA1353 strain expressing *cheY*₆ was clearly more stoppy than a JPA1353 strain expressing *cheY*₆(D56A).

It is unclear why the free-swimming stop frequencies of strains overexpressing *cheY*₃, *cheY*₄, *cheY*₅ and *cheY*₆ in WS8N did not tally with their phenotypes on swim-plates i.e. overexpression of *cheY*_{3,4,5} reduced wild-type taxis on swim plates but had no obvious effect on stop frequency, whilst overexpression of *cheY*₆ did not affect wild-type taxis but caused stop frequency to increase dramatically.

Intricacies and curiosities aside, if nothing else, this chapter showed that CheY₆-P stops the motor. The next and final results chapter probes how this mechanism occurs - using a clutch or a brake?

⁸Note that overexpression of *E. coli* CheY induces CW rotation of flagella even in an *E. coli* strain which has *cheA* and all other *che* genes deleted [124].

THE STOP MECHANISM

6.1 OVERVIEW AND AIMS

The *R. sphaeroides* flagellar motor is unusual in that it stops rotating in order for the cell to change swimming trajectory, whereas most motors (like in *E. coli*), switch direction of rotation. The change in rotation direction is thought to be brought about by the binding of CheY-P to the N-terminus of FliM, which causes FliG to change conformation resulting in different electrostatic interactions at the rotor-stator interface. In the stop-start motor of *R. sphaeroides*, a stop could be achieved by disengaging the torque-generating units, analagous to a clutch. If it puts in the clutch, the motor would coast to a stop within about a millionth of a revolution [17]. Alternatively CheY-P binding could trigger the rotor to jam, analogous to a brake. In this scenario the electrostatic interactions at the rotor-stator interface could prevent the rotor from moving.

Recently Blair *et al.* showed that *B. subtilis* uses a molecular clutch to disable its flagella for biofilm formation [125]. Bacteria need to swim to form biofilms but once at a surface swimming is a disadvantage and they rapidly stop swimming. A small protein, EspE, binds to FliG causing the the torque-generating units to disengage. Tethered cells overexpressing the clutch-initiating protein, EspE, behaved as though they were unpowered, analogous to a strain lacking torque-generating units ($\Delta motA motB$). Similarly, previous studies noted that tethered *R. sphaeroides* cells appeared to undergo free rotational Brownian motion during stop events, indicative of a clutch mechanism [85, 74].

As discussed at the end of Section 1.2.3, the motor is coupled to a helical filament via a hook. In the tethered cell assay we assess motor behaviour by monitoring the

position of the cell body which is tethered via the filament to a glass coverslip. By applying torque to partially locked tethered cells, Block *et al.* showed that the *E. coli* filament is stiff and rigid whilst the hook is relatively compliant [4, 126]. This illuminates an inherent problem of using the tethered cell assay to infer properties of the motor; one may be inclined to conclude prematurely that the motor is stopped using a clutch if the compliant nature of the hook is not taken into account.

6.2 RESULTS

To discriminate between the clutch-brake mechanisms the first test was to observe the motion of tethered *R. sphaeroides* like in the *B. subtilis* experiment above. The behaviour of JPA1213 (*cheY*₆(D56N)), which is entirely non-motile, was examined. Unfortunately, since cells do not rotate, it was impossible to tell which cells were correctly tethered by their flagellum and which were just stuck to the coverslip. Of the cells that appeared to be tethered, many appeared to flop around their tether, as they underwent free rotational Brownian motion. However the vast majority of cells were held rigid. Were these held firm with a brake or simply stuck to the coverslip? Were the cells that were undergoing free rotational Brownian motion stopped with a clutch, or locked with a brake which was masked by the elastic tether? Due to these ambiguities, it was impossible to form a sound conclusion.

Thus the clutch-brake hypothesis was investigated another way, by applying external torque to chemotactically stopped motors. Wild-type cells were tethered by their flagella in a flow chamber. Chemoattractant (1 mM propionate)¹ was removed to initiate a chemotactic response, a stop. The behaviour of the cell bodies was monitored as external torque was applied using viscous flow² or optical tweezers. The analysis of data from Sections 6.2.1, 6.2.2, and 6.2.3 were performed by Dr T. Pilizota.

6.2.1 APPLICATION OF EXTERNAL TORQUE USING VISCOUS FLOW

Following the removal of 1 mM propionate to initiate the stop, external torque was applied by flowing buffer past the cell. The flow rate was adjusted to be as high as possible without the possibility of stalling the motor when it pushed the cell body against the flow (positive angles, cartoon in Figure 6.1). A very thin tube (0.8 mm

¹This is a very large stimulus, thus cells stop for a relatively long time (~1–2 mins).

²The idea of using viscous flow was formulated by Dr R. Berry.

diameter, Anachem) was inserted in the end of the outflow tube so that the flow rate could be adjusted by changing its height.

The position of the cell body was recorded with a video camera (LCL-902K, Wattec) as the cell adapted. Data were saved to DVD before being converted to AVI files using Auto Gordian Knot software (<http://www.autogk.me.uk/>). Angle-time traces were compiled by Dr T. Pilizota using VirtualDub (<http://www.virtualdub.org/>) and custom LabView programs.

Clutch induced stops would cause the cell body to orientate with the flow at 0° . In contrast, Figure 6.1 shows that cell bodies are held at particular angles irrespective of the flow direction, indicating that the motor is locked. The central angle-time trace shows that cell bodies are held rigid during stops. The stop at -90° , when the cell rotates in the same direction as the flow, most clearly shows the presence of a lock as it is impossible that the motor is just stalled in the flow.

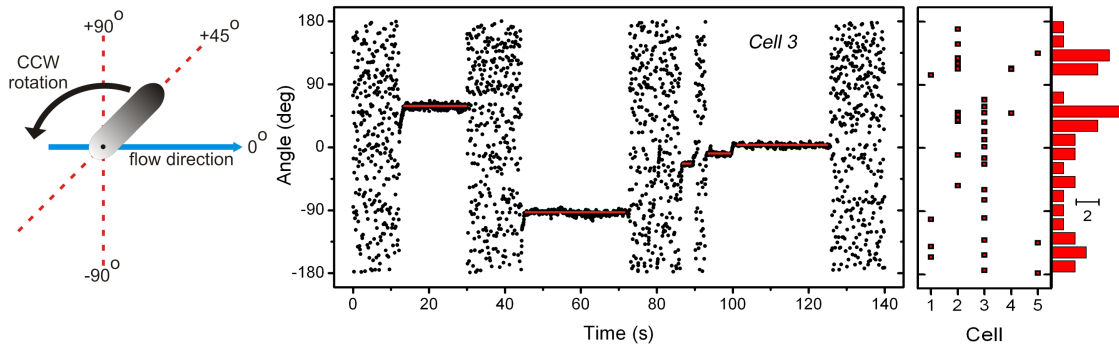


Figure 6.1: Application of external torque by flow on the *R. sphaeroides* motor during a stop. Cartoon depicting experimental setup (left), angle-time trace of a tethered cell in the flow shows that stops occur at random angles (middle), and the mean stop angles of another 4 cells complete with histogram showing a broad distribution (right).

6.2.2 EXTERNAL TORQUE USING AN OPTICAL TRAP

Thus it appears that the motor is actively stopped using a brake. Whilst the flow rate could be controlled with adequate precision to give a yes/no clutch/brake answer, it was not possible to estimate how much torque needed to be applied to move the rotor out of its locked state (T_{lock}). Thus the experiment was repeated, but this time external torque was administered using the cell body as a handle for an optical trap (see Section 1.4.4 for an introduction to optical trapping).

The maximum torque (T_{max}) the trap can exert on the motor was calibrated against the motor's stall torque (T_{stall}) at the start of each run. T_{stall} is the amount

of torque applied by the motor when the load on the motor becomes so large that it cannot rotate at all ($T_{stall} = 1,333 \pm 286$ pNm/rad, Section 3.2.4, Page 57). The trap was kept at a fixed position and the laser power increased until the rotating cell body was just stalled (i.e. it was just enough to temporarily halt the motor). T_{max} could then be varied with respect to T_{stall} by using a set of ND filters.

To estimate how much the motor resisted forward motion, a stop was initiated by removing chemoattractant, and the trap used to try to move the cell body in a series of 45° angles (up to a maximum of 315° , 7 increments). The procedure was repeated to give different values of T_{max} : (0.1, 0.2, 0.5, 1.0, 2.0, 3.2, 5.0, 10.0) $\times T_{stall}$. These values were achieved by calibrating T_{max} to T_{stall} with a certain ND filter in place, which was then swapped with another just before the cell was grabbed with the trap (see Table 6.1). The position of the cell body was recorded using a video camera and analysed as above.

T_{stall}	ND _A	ND _B
0.1	0.0	1.0
0.2	0.3	1.0
0.5	0.0	0.3
1.0	0.0	0.0
2.0	0.3	0.0
3.2	0.5	0.0
5.0	1.0	0.3
10.0	1.0	0.0

Table 6.1: ND filter settings used to apply 8 different torque values, all relative to the stall torque of the particular motor used in the run. T_{max} was calibrated to T_{stall} with ND_A in place, which was then replaced with ND_B before the cell was grabbed with the trap. Note $T_{max} = 10^{ND_{change}}$; e.g. for 3.2 T_{max} , the ND change is 0.5; $10^{0.5} = 3.2$.

Figure 6.2 shows the angle the cell body moved with the trap at various applied torques. (1) At $T_{max} \leq 0.2T_{stall}$ the applied external torque was too weak to move the rotor out of the lock; after the first 45° trap increment, the cell body only moved 12° and rebounded to its original position (inset). (2) At a T_{max} of 0.5 - $2.0T_{stall}$, the angle the rotor could be moved was variable; the cell body moved in a range from $\sim 30 - 315^\circ$, rebounding $28 \pm 14^\circ$. (3) At a T_{max} of $3.2T_{stall}$, approximately 50 % of the cells had their rotor moved until the trap was shuttered (i.e. the laser path was blocked and the cell released); the cell body moved with the trap up to 315° , rebounding $37 \pm 18^\circ$. (4) At $T_{max} > 3.2T_{stall}$ the rotor could be freely manipulated with the trap (see video in Appendix D.2, Page 131); the cell body always moved all the way to 315° , rebounding $31 \pm 14^\circ$. Based on this, T_{lock} is ~ 3 times greater than

the motor's stall torque. The large variability in response at $T_{max} = 0.5\text{--}3.2T_{stall}$ may in part be attributable to the reported variation in trap stiffness at different angles [101].

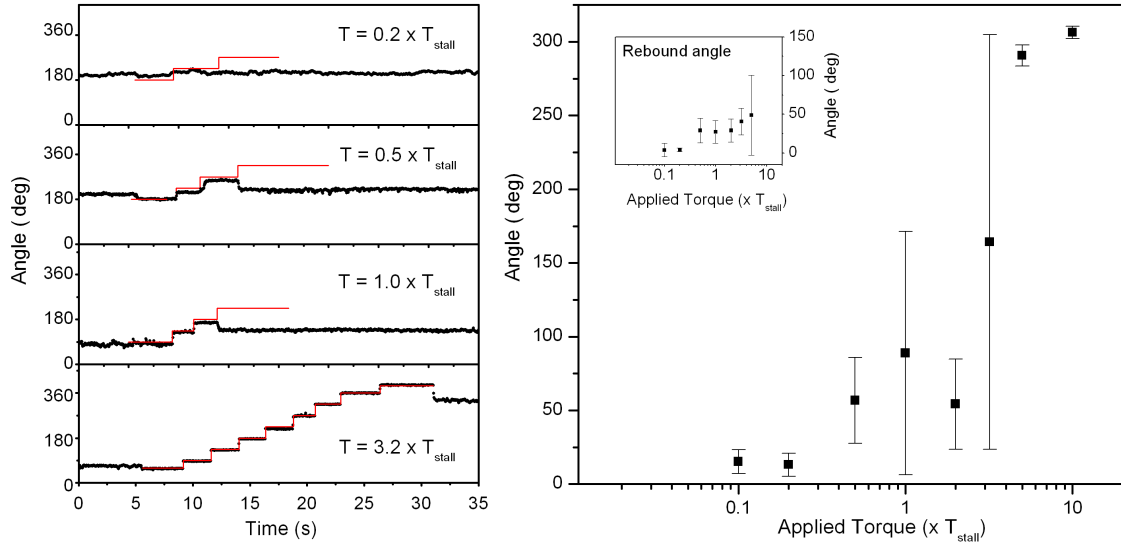


Figure 6.2: Angle the cell body moved with the trap at various applied torques. *Left*, raw data - angle-time traces of tethered cells as above (black), with the angle of the trap when on (red). The trap moves in 45° increments; as a general rule the higher the applied torque, the greater the propensity for the cells to follow the trap. *Right*, mean angle cell bodies moved as a function of trap strength (T_{max}) for the dataset; $n_{run}(n_{cell}) = 6(4), 4(4), 7(5), 9(7), 6(4), 10(9), 4(4), 2(2)$ for $T_{max} = 0.1, 0.2, 0.5, 1.0, 2.0, 3.2, 5.0, 10.0 \times T_{stall}$ respectively. The inset shows the mean cell body rebound angle upon release/escape from the trap. It was not possible to accurately estimate the rebound angle when at $T_{max} = 10.0 \times T_{stall}$ because at such large torques the cell body moved from its initial centre of attachment, introducing a large error. The constant rebound angle (mean = $32 \pm 15^\circ$) indicates that a torque, was maintained throughout the forced rotation of the locked motor. Error bars correspond to the standard deviation about the mean.

More information was extracted by examining the angle the cell body rebounded (R_θ). First the tether stiffness (k_θ) could be determined and second, this value could be used to formulate another estimation of T_{lock} . The analysis, performed by Dr T. Pilizota, was carried out as follows.

When cells escaped/were released from the trap they rebounded $\sim 32 \pm 15^\circ$. For comparison, tethered *E. coli* rebound $\sim 180^\circ$ [4]. Angle-time traces of the cell body following release/escape from the trap reveals that the *R. sphaeroides* tether relaxes exponentially (Figure 6.3). This is expected when the main contribution of k_θ comes from the hook rather than the filament [126]. Thus k_θ was estimated by fitting the relaxation with an exponential of time constant $\tau = 0.1$ s, where $\tau = f/k_\theta$ (f being the drag coefficient of the tethered cell). f of each individual cell was

calculated using the equation $T = \omega \cdot f$, since both T and ω were known; $T = 1,225$ pNm/rad (plateau torque obtained in Chapter 3.2.4) and ω was estimated from the speed of the cell's rotation before and after external torque was applied. This gave $k_\theta = 6900 \pm 900$ pNm/rad² ($k_\theta = f/\tau$). k_θ has been estimated in *E. coli* at 400 pNm/rad² [4], thus the *R. sphaeroides* hook is an order of magnitude stiffer.

This agrees with previous observations (a) that the *R. sphaeroides* hook is straight and therefore possibly stiffer than *E. coli*'s hook [55], and (b), that a $0.83\mu\text{m}$ bead held down in the z-plane by the trap bounces back up when released/when it escaped (see video in Appendix D.2, Page 131; the bead was held down by the trap at time = 3–6 s and 8–14 s).

Once the tether stiffness was known, T_{lock} could be estimated using the formula, $T_{lock} = k_\theta \cdot R_\theta$. Using this method, T_{lock} was estimated at $2,800 \pm 1,000$ pNm/rad. Given that $T_{stall} \approx 1,333$ pNm/rad (obtained earlier with $1.90\mu\text{m}$ beads), $T_{lock} = 2.1$. Thus $T_{lock} \approx 2-3 T_{stall} \approx 2,500-4,000$ pNm/rad.

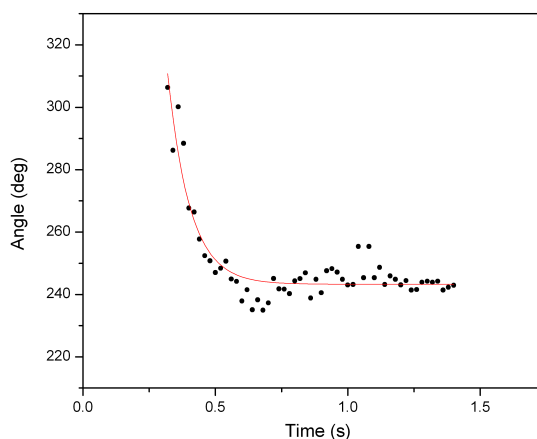


Figure 6.3: An angle-time trace of a tethered cell rebound. The cell body was moved by the trap in increments of 45° ($T_{max} = 0.5 \times T_{stall}$). The trap moved 135° while the cell body moved $\sim 100^\circ$ and rebounded. Thus the optical trap wound up the tether and was able to partially move the rotor out of its original lock position. The cell body rebound corresponds to relaxation of the tether and was fitted with an exponential (red line).

6.2.3 STOPS OCCUR AT DISCRETE ANGLES

In order to gain more information about the motor-locking mechanism, angle-time traces of beads on flagellar stubs from wild-type cells were examined. It was already clear from earlier work that the variation in speed when undergoing a stop was minimal (Figure 3.5, Page 56). Figure 6.4 shows that beads are held at particular angles, showing no large-scale deviations during a stop. These are maintained for

extensive periods of time when stops are induced by removing chemoattractant (Figure 6.4, bottom). $0.83 \mu\text{m}$ beads attached to filament stubs of free motors would be expected to move $\sim 172^\circ$ in 2 s by free rotational Brownian motion alone.³ This supports evidence from the previous experiments that the motor is locked with a brake. It was also apparent from these traces that beads can proceed in series of steps in angle during a stop.

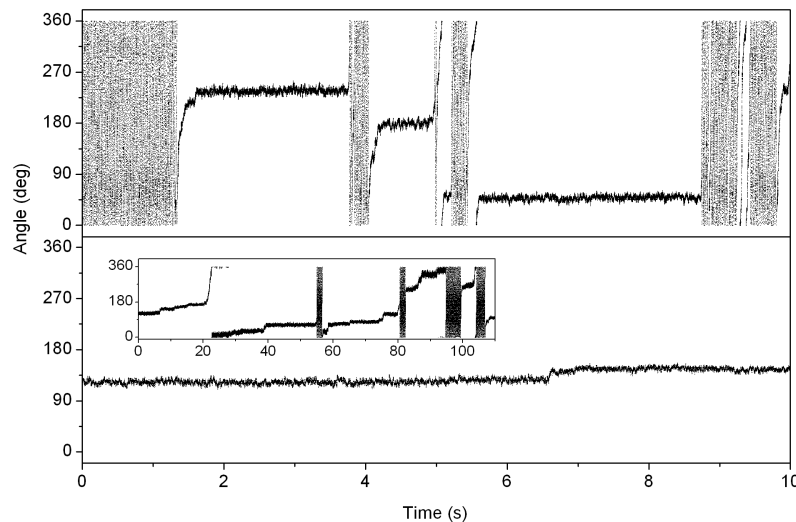


Figure 6.4: Angle of beads ($0.83 \mu\text{m}$) attached to flagellar stubs from WS8N cells as a function of time. Traces were obtained as described earlier in Section 3.2.3 (632 nm laser, 10 kHz sampling rate) and Section 4.2.4 (1064 nm laser, 2 kHz sampling rate) for *top* and *bottom* traces respectively. Beads are held at constant angles and exhibit no large-scale deviations during a stop at steady-state (*top*) or when long chemotactic stops are induced by removal of chemoattractant (*bottom*). The *bottom* trace (*inset*) shows the bead rotating very slowly forward in a series of steps during stop events.

To increase the chance of observing steps, *cheY₆* was overexpressed in WS8N from pIND4 (~ 14 h induction, 1 mM IPTG), resulting in an increase in stop frequency (Chapter 5). The position of $0.83 \mu\text{m}$ beads attached to flagellar stubs were detected using the 1064 nm laser at a sampling rate of 5 kHz. Under these conditions the motor regularly underwent prolonged stop events which consisted of ‘steppy’ slow rotation.

Figure 6.5 show examples of steppy traces observed from WS8N and pIND-Y6 / WS8N overexpression cells. Backwards steps were not observed. It is clear that the motor is stopped at *particular* angles; however, are these angles *discrete*, i.e. can the motor stop be stopped at any single possible angle or is it restricted? To

³Root mean-square angular deviation $= \sqrt{2D_r t}$, where D_r is the rotational diffusion coefficient of the bead and t is the time interval.

answer this question step analysis was performed by Dr T. Pilizota using a computer algorithm as described previously [37, 102]. Figure 6.5 *bottom right* shows the step size histogram. A Gaussian fit gives a peak of $13.0 \pm 4.5^\circ$ corresponding to approximately 27–28 steps per revolution.

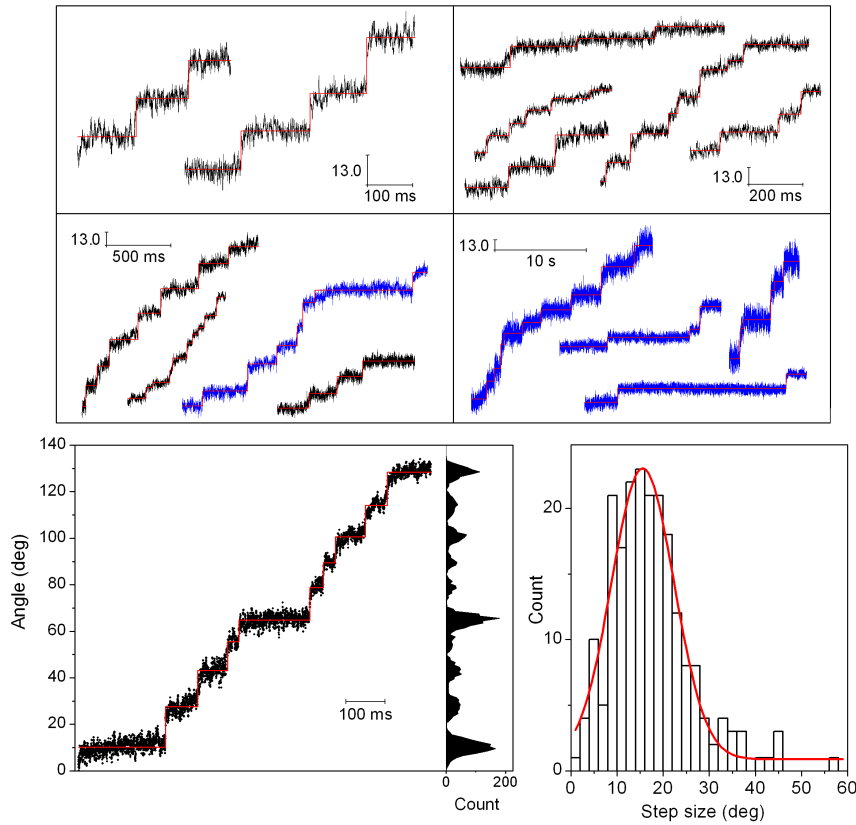


Figure 6.5: Step analysis. *Top*, examples of angle-time traces showing steps during stop events from WS8N (blue) and pIND-Y6 / WS8N overexpression (black) cells. In all cases $0.83 \mu\text{m}$ beads were used. The output of a step-finding algorithm is superimposed (red). *Bottom left*, angle-time trace and its accompanying histogram of dwell angles (bin size = 1°). *Bottom right*, the step size obtained from step-finding algorithm was used to construct a step size histogram ($n_{\text{step}} = 361$ (WS8N and pIND-Y6 / WS8N), histogram bin size = 2°).

In bidirectional motors, the binding of CheY-P to the switch complex is presumed to instigate a conformational change in FliM which in turn affects the orientation of the charged ridge in the C-terminus of FliG [42, 30]. The different electrostatic interactions, resulting from this new rotor-stator interface (between FliG and the cytoplasmic loop of the stator (MotA)), are deemed responsible for rotation in the alternative direction [43].

Similarly, it is likely this new rotor-stator interface stops the *R. sphaeroides*

motor. During a stop the conformation of FliG may increase the periodic potential barriers along which the motor steps, making movement in either direction unfavourable. Alternatively perhaps the rotor could interact with an unidentified motor component. With this in mind the $\Delta fliM_2$ strain was examined using the bead assay but it behaved like wild-type.

In either case, steps could also be due to a temporary reduction in the amplitude of the locking potential, permitting a thermally activated jump from one minimum to the next. This is exaggerated in a strain overexpressing *cheY*₆, perhaps due to the binding of unphosphorylated CheY₆ to the motor. Consequently the rotor may lapse into an intermediate state rather than the ‘all or none’ behaviour of wild-type. Alternatively, the frequency of transitions between the ‘stop’ and the ‘run’ conformations of the rotor maybe increased.

Since no backwards steps were observed, there may be a higher barrier to backwards rotation in *R. sphaeroides*. This could be tested by pushing the cell body with the trap in the backward direction, as well as forwards. This will be tested in future work.

6.3 CONCLUSIONS

By applying external torque to the motor using two independent techniques, it was discovered that, during chemotactic-induced stops, motors were held rigid and resisted rotation indicating a braking mechanism. Using the cell body as a handle for an optical trap, the value of torque resisting forward motion (keeping it locked) was estimated to be 2–3 times the motor’s stall torque (2,500–4,000 pNnm/rad). Furthermore beads attached to flagellar stubs are held at a fixed angle for several seconds, exhibiting no large-scale deviations. Thus, *R. sphaeroides* uses a braking mechanism to stop its flagellar motor. Finally step analysis revealed that stop events occur at 27-28 *discrete* angles around the motor.

This is in contrast to the clutch mechanism used by *B. subtilis* to disable its flagella for biofilm formation [125]. Whilst it is perfectly possible that *B. subtilis* uses a clutch, merely *observing* the behaviour of tethered cells is not proof because the stiffness of the tether is not known (parameters were based on the stiffness of the *E. coli* hook which is a fair assumption given that *B. subtilis* has multiple flagella). Indeed previous studies mentioned that tethered *R. sphaeroides* cells appeared to undergo free rotational Brownian motion during stop events [85, 74]. Applying external torque is the best way to discriminate between the clutch-brake hypotheses.

Elucidating the *R. sphaeroides* stop mechanism was much easier than in *B. subtilis* because stop events were frequent, reversible, and controllable on a short time-scale.

In order for a brake to occur, the rotor must interact with a stationary component. As stated above, the obvious candidates are the stator units. A number of experiments could be conducted to confirm this. It is highly likely the stator units are still present during a stop since there was no indication of ‘de-resurrection/resurrection’ going into/out of stops (Chapter 3). However, it could be confirmed by performing fluorescent microscopy of tethered *R. sphaeroides* strains carrying ‘MotB-GFP’ and ‘MotB-GFP plus CheY₆(D56N)’. Also, work done on *V. alginolyticus* suggests that stators are held in place by the ion-motive force [127]. After inducing a long stop by removal of propionate, one could quickly eliminate the *pmf* in *R. sphaeroides* by adding respiratory and ATPase poisons and observe the behaviour of the bead. One would expect the ‘rigid locked-brake’ characteristic to be replaced with ‘free rotational Brownian motion’ characteristics as stator units disengage and the lock eases. Alternatively, one could repeat the trap experiment with a strain that has a low number of stator units (i.e. leaky expression of MotB/pIND4 in a Δ *MotB* strain). It is likely that the T_{lock} would be reduced in absolute terms but that the ratio ($T_{lock} \approx 2-3T_{stall}$) is maintained. Disrupting the lock strength by making point mutants in the conserved charged residues of MotA and FliG would be the most elegant way of showing that it is the electrostatic forces between the rotor and stators that are responsible for locking the motor.

Finally, the observation that beads stop at only $\sim 27-28$ discrete angles around the motor is in agreement with the ~ 26 steps per revolution observed previously using a very slowly rotating Na⁺-driven chimaeric flagellar motor in *E. coli*, achieved using a low sodium-motive force with controlled expression of a small number of torque-generating units [37]. They concluded that the steps reflected the rotor track that the stators ran on (~ 26 FliG copies). However it was possible that these steps were a result of using a motor with only one functional Mot complex. Since stepping is also observed in the *R. sphaeroides* wild-type motor, with a full complement of stators, it is likely that both the torque-generating and stopping mechanisms are governed solely by the periodicity of the rotor ring. The switching process in bidirectional motors such as *E. coli* probably also obeys this periodicity, but it is hard to observe because the flexible hook must be un-wound and re-wound upon each reversal. *R. sphaeroides*, with its stiff hook and unusual motor switch mechanism, has provided an insight into molecular motor mechanics, which would not have been possible had research been restricted to *E. coli*.

DISCUSSION AND FUTURE WORK

Controlling the output of molecular motors is critical for many cellular processes governing cell growth, division and transport. In addition, regulating their force-generating capabilities is a prerequisite for the operation of useful bionanodevices [128]. This thesis contributes to our understanding of how the unidirectional proton-driven flagellar motor of *R. sphaeroides* is controlled. Progress was made by applying several forms of motor manipulation (genetic, environmental, and mechanical) often in combination. The contribution of the bead assay, facilitating high-resolution analysis of motor output for the first time, cannot be underestimated.

Chapter 3 describes the behaviour of the motor under the control of the native, wild-type chemotaxis system. This was achieved by monitoring the rotation of 0.83 μm beads stuck to flagellar stubs by BFP-interferometry with a 632 nm laser at a sampling rate of 10 kHz. Speed-time traces from 41 wild-type cells were analysed individually using custom software. Motor behaviour (assessed in terms of stop length, stop frequency, and run bias) was highly variable. Perhaps this confers a selective advantage for *R. sphaeroides*, a metabolically diverse scavenger. Studying the steady-state variability in motor behaviour from other species occupying a range of ecological niches may expose a theme (e.g. the more diverse the niche, the more variable the behaviour).

Next, the performance of the motor itself (in the high-load low-speed regime at least) was examined. Its plateau torque, cruising speed and direction of rotation were identical to the proton-driven motor of *E. coli*. Transient step changes in speed were also clearly visible. These events are more obvious than in *E. coli*, perhaps because of the stiffer *R. sphaeroides* hook.

Given the similarities in performance, it seems that the same motor is coupled to a different molecular gearbox. We will probably never know why two flagellar motor gearboxes evolved, but it may be possible to determine what makes the *R. sphaeroides* motor unidirectional as opposed to bidirectional. With this in mind, one study showed that a chimeric FliG protein, N-terminal *E. coli*–C-terminal *R. sphaeroides*, supports bidirectional rotation in *E. coli* [129]. Thus it is not just the C-terminus of *R. sphaeroides* FliG that confers unidirectionality. The next experiment would be to establish if the *R. sphaeroides* stators can push a bidirectional rotor in both directions.

Lower risk future experiments could characterise the low-load high-speed regime of the *R. sphaeroides* torque-speed curve using smaller beads, and perform resurrection experiments to determine how many torque-generating units are present in a functioning motor. More interestingly, the characteristics of the *R. sphaeroides* *fla2* flagellar motor are waiting to be discovered.

Chapter 4 revealed some fundamental control characteristics. (1) Without any CheY-P to stop the motor, it rotates continuously. (2) By monitoring the behaviour of the motor at an adequate resolution, the suggestion that the chemotaxis system could control motor speed, as well as the propensity to stop, was dispelled. (3) In addition, the flow cell experiments also illustrated that *R. sphaeroides* does respond to positive (increasing chemoattractant concentration) by reducing its stop frequency, which was previously hard to detect with video recordings of tethered cells. (4) Finally, preliminary evidence indicates that a component of PBS buffer may elicit a repellent response in *R. sphaeroides*. Further experiments are required to identify which components are responsible. These simple observations make unscrambling the *R. sphaeroides* chemotaxis pathway a little easier.

Although many technical obstacles were circumnavigated in designing and conducting experiments presented in this thesis, some aspects were compromised. In particular, it was unfortunate that there was not more time to expose cells to environmentally relevant stimuli rather than using high levels of chemoattractant (1 mM propionate), delivered via flow cell. This was both (i) artificial, since bacteria in the wild would never experience sharp 1 mM gradients due to mixing, and (ii), imprecise since one cannot know exactly when the bacterium was exposed to the stimulus in the first instance. Monitoring the rotation of beads whilst delivering instantaneous, controllable, sub-saturating stimuli in the form of light is the next challenge.

Chapter 5 attempted to ‘unscramble’ the terminal end of the pathway by determining the roles of CheY₃, CheY₄, and CheY₆. The simple experiment to test the motor-stopping capabilities of the various CheYs failed to give conclusive results. However it did show that a useful IPTG-regulated expression vector, pIND4, has been successfully developed for *R. sphaeroides*.

The most interesting discovery was that CheY₃, CheY₄, and CheY₅ are functionally equivalent. This means that there would certainly be cross-talk between *cheOp*₁ and *cheOp*₂/*cheOp*₃ if both *fla1* and *fla2* flagellar sets were expressed at the same time. *cheY*₃, *cheY*₄, and *cheY*₅ are probably gene duplicates of one another, but which was the original copy and why was it useful in another operon which is turned on under different conditions/controls a completely different flagellar set? It is also intriguing that *cheY*₃ is barely expressed under the conditions tested, yet is essential for chemotaxis in the absence of *cheY*₄. The vast differences in cytoplasmic concentration between CheY₃/CheY₄ and CheY₆ in WS8N must be taken into account when constructing any *R. sphaeroides* chemotaxis model. Interestingly the pattern of expression levels between CheY₃, CheY₄, and CheY₆ from the plasmid, mimicked that of the genome.

The previous results; (1) CheY-P is required to stop the motor, (2) CheYs do not control the cruising speed of the motor, and (3), overexpression of *cheY*₆ increases the stopping frequency, meant that an interesting question could be proposed with clarity - did CheY-P binding cause a loss in transmission of torque (a clutch) or did it lock the motor in a particular configuration (a brake)?

Cells were tethered down to glass coverslips by their flagella and exposed to external forces, either via viscous flow or optical tweezers. Cell bodies resisted re-orientation during a chemotactic stop implying that the motor was held in a locked state. By controlling the power and position of the optical trap it was possible to apply calibrated amounts of torque. At low applied torques the rotor could not be moved, at high applied torques the rotor could always be moved. At an applied torque of 3.2 x stall torque, approximately 50 % of the cells had their rotor moved. Thus, during a chemotactic stop the motor becomes firmly locked up. The value of torque resisting forward motion (keeping it locked) was estimated to be 2–3 x stall torque (2,500–4,000 pNnm/rad).

When cells escaped/were released from the trap they rebounded $\sim 32 \pm 15^\circ$. For comparison, tethered *E. coli* rebound $\sim 180^\circ$ [4]. The *R. sphaeroides* hook stiffness was estimated at 6900 ± 900 pNnm/rad², an order of magnitude stiffer than the *E.*

coli hook (400 pNnm/rad²) [4]. One imagines that a stiffer hook would allow a bacterium faster acceleration from a re-orientation event because less time would be spent winding up the hook. Perhaps the *E. coli* hook is less stiff because it must act as a universal joint, enabling flagella positioned at random over the cell body to come together and form a bundle at the pole. Regardless, perhaps the *R. sphaeroides* flagellar motor should be used in future experiments looking at steps in motor rotation (like Sowa *et al.*, 2005 [37] but at higher speeds), as it is thought that the flexible *E. coli* hook has a damping effect.

Returning to the bead data, it was clear that during a stop the motor resists free rotational Brownian motion and is held at discrete angles, providing further proof of a locking mechanism. Overexpression of *cheY₆* was used to increase the frequency of stop events. Exposing wild-type cells to a decreasing ramp of chemoattractant concentration may be another way of getting many stop events in a short space of time (i.e. before the stage starts to drift/the bead trajectory changes). Another possibility would be to use photoheterotrophically grown cells, and elicit photoresponses by strobing the light stimulus (e.g. at 10 Hz).

The stop angles most likely reflect the periodicity of the site of force generation on the rotor. This represents the first experimental resolution of steps in the rotation of a wild-type bacterial flagellar motor with a full complement of torque generating units. Future work must first determine if it really is the stator units doing the locking and if the lock mechanism behaves like a ratchet i.e. it is harder to force backwards than forwards.

Understanding this mechanism will be helped by revealing the structural changes in the switch complex that occur following the binding of CheY-P. Unfortunately elucidating the structure of single motor proteins in one conformation is difficult enough at this stage. However technology for obtaining structural information for macromolecular complexes is advancing, particularly through the use of cryo-electron microscopy. Recently this has led to the direct visualisation and spatial organisation of chemoreceptor arrays in intact *E. coli* [130], and of the entire flagellar motor (including stator units) in the spirochete *Treponema primitia* at 7 nm resolution [131].

However, even with structural data, the operation and control of the bacterial flagellar motor will remain partially mysterious until it can be probed and manipulated *in vitro*. This has been crucial in understanding the molecular mechanisms governing other molecular motors such as F₁F_o-ATPase, myosin, kinesin and dynein. The Rainville Lab (Laval University, Québec) are working towards this goal by using

a laser to punch holes through the *E. coli* cell wall/membrane, granting access to the inside of the cell. Motor performance can be monitored as an external voltage is applied causing the motors rotate (Mathieu Gauthier, personal communication). However there are a few large technical obstacles to overcome before a fully *in vitro* system is developed.

The aim of this project was to learn more about the *R. sphaeroides* flagellar motor and the sensory pathway that controls its output. This work falls on the boundary between two disciplines; the Biology of the chemotaxis pathway and the Physics of the flagellar motor. Applying techniques that were already well established in biophysics with ‘traditional’ assays used in microbiology (genetics/behavioural assays) proved to be a rewarding experimental strategy. Finding a way to measure *R. sphaeroides* motor output at a high-resolution, establishing the default motor behaviour, and observing steps in the rotation of wild-type motors were the highlights. Finally, mechanical manipulation of the 45 nm diameter rotor answered the clutch versus brake mechanism question, providing an insight into how nature controls one of its molecular machines in the unfamiliar world of the nanoscale.

BIBLIOGRAPHY

- [1] H.C. Berg, **Random Walks in Biology** (Princeton University Press, 1993).
- [2] S. Vogel, **Life in Moving Fluids** (Princeton University Press, 1994).
- [3] S. Trachtenberg and D.J. DeRosier, *Three-dimensional structure of the frozen-hydrated flagellar filament: the left-handed filament of Salmonella typhimurium*, Journal of Molecular Biology **195**, 581–601 (1987).
- [4] SM. Block, DF. Blair, and HC. Berg, *Compliance of bacterial flagella measured with optical tweezers*, Nature **338**, 514–517 (1989).
- [5] F.A. Samatey, H. Matsunami, K. Imada, S. Nagashima, T.R. Shaikh, D.R. Thomas, J.Z. Chen, D.J. Derosier, A. Kitao, and K. Namba, *Structure of the bacterial flagellar hook and implication for the molecular universal joint mechanism*, Nature **431**, 1062–1068 (2004).
- [6] H.C. Berg, *Motile behavior of bacteria*, Physics Today **53**, 24–30 (2000).
- [7] S.M. Block, J.E. Segall, and H.C. Berg, *Adaptation kinetics in bacterial chemotaxis*, Journal of Bacteriology **154**, 312–323 (1983).
- [8] L. Turner, W.S. Ryu, and H.C. Berg, *Real time imaging of fluorescent flagellar filaments*, Journal of Bacteriology **182**, 2793–2801 (2000).
- [9] M.D. Baker, P.M. Wolanin, and J.B. Stock, *Signal transduction in bacterial chemotaxis*, Bioessays **28**, 9–22 (2006).
- [10] J.E. Segall, S.M. Block, and H.C. Berg, *Temporal comparisons in bacterial chemotaxis*, Proceedings of the National Academy of Sciences USA **83**, 8987–8991 (1986).

-
- [11] C.M. Dyer and F.W. Dahlquist, *Switched or not?: the structure of unphosphorylated CheY bound to the N terminus of FliM*, Journal of Bacteriology **188**, 7354–7363 (2006).
- [12] X. Zhu, J. Rebello, P. Matsumura, and K. Volz, *Crystal structures of CheY mutants Y106W and T87I/Y106W. CheY activation correlates with movement of residue 106*, Journal of Biological Chemistry **272**, 5000–5006 (1997).
- [13] M. Welch, K. Oosawa, S. Aizawa, and M. Eisenbach, *Phosphorylation-dependent binding of a signal molecule to the flagellar switch of bacteria*, Proceedings of the National Academy of Sciences USA **90**, 8787–8791 (1993).
- [14] G.S. Lukat and J.B. Stock, *Response regulation in bacterial chemotaxis*, Journal of Cellular Biochemistry **51**, 41–46 (1993).
- [15] R.M. Macnab, *How bacteria assemble flagella*, Annual Review of Microbiology **57**, 77–100 (2003).
- [16] S.W. Reid, M.C. Leake, J.H. Chandler, C.J. Lo, J.P. Armitage, and R.M. Berry, *The maximum number of torque-generating units in the flagellar motor of Escherichia coli is at least 11*, Proceedings of the National Academy of Sciences USA **103**, 8066–8071 (2006).
- [17] H.C. Berg, *Bacterial flagellar motor*, Current Biology **18**, 689–691 (2008).
- [18] D. Thomas, D.G. Morgan, and D.J. DeRosier, *Structures of bacterial flagellar motors from two FliF-FliG gene fusion mutants*, Journal of Bacteriology **183**, 6404–6412 (2001).
- [19] H.C. Berg, *The rotary motor of bacterial flagella*, Annual Review of Biochemistry **72**, 19–54 (2003).
- [20] Y. Sowa and R.M. Berry, *Bacterial flagellar motor*, Quarterly Reviews of Biophysics **41**, 1–30 (2008).
- [21] S. Kojima and D.F. Blair, *Solubilization and purification of the MotA/MotB complex of Escherichia coli*, Biochemistry **43**, 26–34 (2004).
- [22] S. Kojima, Y. Furukawa, H. Matsunami, T. Minamino, and K. Namba, *Characterization of the periplasmic domain of MotB and implications for its role in the stator assembly of the bacterial flagellar motor*, Journal of Bacteriology **190**, 3314–3322 (2008).

-
- [23] A. Roujeinikova, *Crystal structure of the cell wall anchor domain of MotB, a stator component of the bacterial flagellar motor: Implications for peptidoglycan recognition*, Proceedings of the National Academy of Sciences USA **105**, 10348–10353 (2008).
- [24] E.R. Hosking, C. Vogt, E.P. Bakker, and M.D. Manson, *The Escherichia coli MotAB proton channel unplugged*, Journal of Molecular Biology **364**, 921–937 (2006).
- [25] M.C. Leake, J.H. Chandler, G.H. Wadhams, F. Bai, R.M. Berry, and J.P. Armitage, *Stoichiometry and turnover in single, functioning membrane protein complexes*, Nature **443**, 355–358 (2006).
- [26] S.M. Block and H.C. Berg, *Successive incorporation of force-generating units in the bacterial rotary motor*, Nature **309**, 470–472 (1984).
- [27] W.S. Ryu, R.M. Berry, and H.C. Berg, *Torque-generating units of the flagellar motor of Escherichia coli have a high duty ratio*, Nature **403**, 444–447 (2000).
- [28] D.R. Thomas, N.R. Francis, C. Xu, and D.J. DeRosier, *The three-dimensional structure of the flagellar rotor from a clockwise-locked mutant of Salmonella enterica Serovar Typhimurium*, Journal of Bacteriology **188**, 7039–7048 (2006).
- [29] R. Zhao, C.D. Amsler, P. Matsumura, and S. Khan, *FliG and FliM distribution in the Salmonella typhimurium cell and flagellar basal bodies*, Journal of Bacteriology **178**, 258–265 (1996).
- [30] S.E. Passmore, R. Meas, and D.L. Marykwas, *Analysis of the FliM/FliG motor protein interaction by two-hybrid mutation suppression analysis*, Microbiology **154**, 714–724 (2008).
- [31] T. Minamino, K. Imada, and K. Namba, *Molecular motors of the bacterial flagella*, Current Opinion in Structural Biology **18**, 693–701 (2008).
- [32] Y. Asai, I. Kawagishi, R.E. Sockett, and M. Homma, *Coupling ion specificity of chimeras between H^+ and Na^+ driven motor proteins in Vibrio polar flagella*, The EMBO Journal **19**, 3639–3648 (2000).
- [33] Y. Asai, T. Yakushi, I. Kawagishi, and M. Homma, *Ion-coupling determinants of Na^+ -driven and H^+ -driven flagellar motors*, Journal of Molecular Biology **327**, 453–463 (2003).

-
- [34] Y. Inoue, C.J. Lo, H. Fukuoka, H. Takahashi, Y. Sowa, T. Pilizota, G.H. Wadhams, M. Homma, R.M. Berry, and A. Ishijima, *Torque–speed relationships of Na^+ -driven chimeric flagellar motors in Escherichia coli*, Journal of Molecular Biology **376**, 1251–1259 (2007).
- [35] C.V. Gabel and H.C. Berg, *The speed of the flagellar rotary motor of Escherichia coli varies linearly with protonmotive force*, Proceedings of the National Academy of Science USA **100**, 8748–8751 (2003).
- [36] R.M. Berry and J.P. Armitage, *The bacterial flagella motor*, Advances in Microbial Physiology **41**, 291–337 (1999).
- [37] Y. Sowa, A.D. Rowe, M.C. Leake, T. Yakushi, M. Homma, A. Ishijima, and R.M. Berry, *Direct observation of steps in rotation of the bacterial flagellar motor*, Nature **437**, 916–919 (2005).
- [38] J. Zhou, L.L. Sharp, H.L. Tang, S.A. Lloyd, S. Billings, T.F. Braun, and D.F. Blair, *Function of protonatable residues in the flagellar motor of Escherichia coli: a critical role for Asp-32 of MotB*, Journal of Bacteriology **180**, 2729–2735 (1998).
- [39] D.F. Blair and H.C. Berg, *Restoration of torque in defective flagellar motors*, Science **242**, 1678–1681 (1988).
- [40] K. Paul, J.G. Harmon, and D.F. Blair, *Mutational analysis of the flagellar rotor protein FliN: identification of surfaces important for flagellar assembly and switching*, Journal of Bacteriology **188**, 5240–5248 (2006).
- [41] D.F. Blair, *Flagellar movement driven by proton translocation*, FEBS Letters **545**, 86–95 (2003).
- [42] P.N. Brown, M. Terrazas, K. Paul, and D.F. Blair, *Mutational analysis of the flagellar protein FliG: sites of interaction with FliM and implications for organization of the switch complex*, Journal of Bacteriology **189**, 305–312 (2007).
- [43] S.M. Van Way, S.G. Millas, A.H. Lee, and M.D. Manson, *Rusty, jammed, and well-oiled hinges: mutations affecting the interdomain region of FliG, a rotor element of the Escherichia coli flagellar motor*, Journal of Bacteriology **186**, 3173–3181 (2004).

-
- [44] P.N. Brown, C.P. Hill, and D.F. Blair, *Crystal structure of the middle and C-terminal domains of the flagellar rotor protein FliG*, The EMBO Journal **21**, 3225–3234 (2002).
- [45] P. Cluzel, M. Surette, and S. Leibler, *An ultrasensitive bacterial motor revealed by monitoring signaling proteins in single cells*, Science **287**, 1652–1655 (2000).
- [46] V. Sourjik and H.C. Berg, *Binding of the Escherichia coli response regulator CheY to its target measured in vivo by fluorescence resonance energy transfer*, Proceedings of the National Academy of Sciences USA **99**, 12669–12674 (2002).
- [47] D. Bray and T.A.J. Duke, *Conformational spread: the propagation of allosteric states in large multiprotein complexes*, Rendiconti Lincei **17**, 221–241 (2006).
- [48] T.A.J. Duke, N. Le Novère, and D. Bray, *Conformational spread in a ring of proteins: a stochastic approach to allostery*, Journal of Molecular Biology **308**, 541–553 (2001).
- [49] G.H. Wadhams and J.P. Armitage, *Making sense of it all: bacterial chemotaxis*, Nature Reviews Molecular Cell Biology **5**, 1024–1037 (2004).
- [50] P.M. Slovak, G.H. Wadhams, and J.P. Armitage, *Localization of MreB in Rhodobacter sphaeroides under conditions causing changes in cell shape and membrane structure*, Journal of Bacteriology **187**, 54–64 (2005).
- [51] J.P. Armitage and R.M. Macnab, *Unidirectional, intermittent rotation of the flagellum of Rhodobacter sphaeroides*, Journal of Bacteriology **169**, 514–518 (1987).
- [52] J.P. Armitage, T.P. Pitta, M.A. Vigeant, H.L. Packer, and R.M. Ford, *Transformations in flagellar structure of Rhodobacter sphaeroides and possible relationship to changes in swimming speed*, Journal of Bacteriology **181**, 4825–4833 (1999).
- [53] H.L. Packer and J.P. Armitage, *The unidirectional flagellar motor of Rhodobacter sphaeroides WS8 can rotate either clockwise or counterclockwise: characterization of the flagellum under both conditions by antibody decoration*, Journal of Bacteriology **175**, 6041–6045 (1993).

-
- [54] M. Fujii, S. Shibata, and S.I. Aizawa, *Polar, peritrichous, and lateral flagella belong to three distinguishable flagellar families*, Journal of Molecular Biology **379**, 273–283 (2008).
- [55] K. Kobayashi, T. Saitoh, D.S.H. Shah, K. Ohnishi, I.G. Goodfellows, R.E. Sockett, and S.I. Aizawa, *Purification and characterization of the flagellar basal body of Rhodobacter sphaeroides*, Journal of Bacteriology **185**, 5295–5300 (2003).
- [56] H.L. Packer, D.M. Harrison, R.M. Dixon, and J.P. Armitage, *The effect of pH on the growth and motility of Rhodobacter sphaeroides WS8N and the nature of the driving force of the flagellar motor*, Biochimica et biophysica acta. Bioenergetics **1188**, 101–107 (1994).
- [57] S. Poggio, C. Abreu-Goodger, S. Fabela, A. Osorio, G. Dreyfus, P. Vinuesa, and L. Camarena, *A complete set of flagellar genes acquired by horizontal transfer coexists with the endogenous flagellar system in Rhodobacter sphaeroides*, Journal of Bacteriology **189**, 3208–3216 (2007).
- [58] G.H. Wadhams, A.V. Warren, A.C. Martin, and J.P. Armitage, *Targeting of two signal transduction pathways to different regions of the bacterial cell*, Molecular Microbiology **50**, 763–770 (2003).
- [59] S.L. Porter, G.H. Wadhams, and J.P. Armitage, *Rhodobacter sphaeroides: complexity in chemotactic signalling*, Trends in Microbiology **16**, 251–260 (2008).
- [60] S.L. Porter, M.A. Roberts, C.S. Manning, and J.P. Armitage, *A bifunctional kinase-phosphatase in bacterial chemotaxis*, Proceedings of the National Academy of Sciences USA **105**, 18531–18536 (2008).
- [61] S.L. Porter, A.V. Warren, A.C. Martin, and J.P. Armitage, *The third chemotaxis locus of Rhodobacter sphaeroides is essential for chemotaxis*, Molecular Microbiology **46**, 1081–1094 (2002).
- [62] S.L. Porter, G.H. Wadhams, A.C. Martin, E.D. Byles, D.E. Lancaster, and J.P. Armitage, *The CheYs of Rhodobacter sphaeroides*, Journal of Biological Chemistry **281**, 32694–32704 (2006).
- [63] S.L. Porter, **The chemotaxis proteins of *Rhodobacter sphaeroides***, D.Phil thesis, University of Oxford, 2002.

-
- [64] M.M. McEvoy, A.C. Hausrath, G.B. Randolph, S.J. Remington, and F.W. Dahlquist, *Two binding modes reveal flexibility in kinase/response regulator interactions in the bacterial chemotaxis pathway*, Proceedings of the National Academy of Sciences USA **95**, 7333–7338 (1998).
- [65] S.J. Roman, M. Meyers, K. Volz, and P. Matsumura, *A chemotactic signaling surface on CheY defined by suppressors of flagellar switch mutations*, Journal of Bacteriology **174**, 6247–6255 (1992).
- [66] S.L. Porter and J.P. Armitage, *Chemotaxis in Rhodobacter sphaeroides requires an atypical histidine protein kinase*, Journal of Biological Chemistry **279**, 54573–54580 (2004).
- [67] A. Ferre, J. de la Mora, T. Ballado, L. Camarena, and G. Dreyfus, *Biochemical study of multiple CheY response regulators of the chemotactic pathway of Rhodobacter sphaeroides*, Journal of Bacteriology **186**, 5172–5177 (2004).
- [68] N. Garcia, A. Campos, A. Osorio, S. Poggio, B. Gonzalez-Pedrajo, L. Camarena, and G. Dreyfus, *The flagellar switch genes fliM and fliN of Rhodobacter sphaeroides are contained in a large flagellar gene cluster*, Journal of Bacteriology **180**, 3978–3982 (1998).
- [69] S. Poggio, A. Osorio, G. Corkidi, G. Dreyfus, and L. Camarena, *The N terminus of FliM is essential to promote flagellar rotation in Rhodobacter sphaeroides*, Journal of Bacteriology **183**, 3142–3148 (2001).
- [70] D.S. Bischoff and G.W. Ordal, *Sequence and characterization of Bacillus subtilis CheB, a homolog of Escherichia coli CheY, and its role in a different mechanism of chemotaxis*, Journal of Biological Chemistry **266**, 12301–12305 (1991).
- [71] V. Sourjik and R. Schmitt, *Phosphotransfer between CheA, CheY₁, and CheY₂ in the chemotaxis signal transduction chain of Rhizobium meliloti*, Biochemistry **37**, 2327–2335 (1998).
- [72] A.M. del Campo, T. Ballado, J. de la Mora, S. Poggio, L. Camarena, and G. Dreyfus, *Chemotactic control of the two flagellar systems of Rhodobacter sphaeroides is mediated by different sets of CheY and FliM Proteins*, Journal of Bacteriology **189**, 8397–8401 (2007).

-
- [73] A.J. Wolfe and H.C. Berg, *Migration of bacteria in semisolid agar*, Proceedings of the National Academy of Sciences USA **86**, 6973–6977 (1989).
- [74] R.M. Berry and J.P. Armitage, *Response kinetics of tethered Rhodobacter sphaeroides to changes in light intensity*, Biophysical Journal **78**, 1207–1215 (2000).
- [75] N.C. Darnton, L. Turner, S. Rojevsky, and H.C. Berg, *On torque and tumbling in swimming Escherichia coli*, Journal of Bacteriology **189**, 1756–1764 (2007).
- [76] A.D. Rowe, M.C. Leake, H. Morgan, and R.M. Berry, *Rapid rotation of micron and sub-micron dielectric particles measured using optical tweezers*, Journal of Modern Optics **50**, 1539–1554 (2003).
- [77] M. Hashimoto, T. Mashimo, T. Hirano, S. Yamaguchi, and S.I. Aizawa, *Functional roles of the hook in a rotating tethered cell*, Journal of Molecular Biology **375**, 367–375 (2007).
- [78] A.D. Rowe, **Rotation of the sodium driven bacterial flagellar motor**, D.Phil thesis, University of Oxford, 2005.
- [79] G. Kuwajima, *Construction of a minimum-size functional flagellin of Escherichia coli*, Journal of Bacteriology **170**, 3305–3309 (1988).
- [80] H.L. Packer and J.P. Armitage, *The chemokinetic and chemotactic behavior of Rhodobacter sphaeroides: two independent responses*, Journal of Bacteriology **176**, 206–212 (1994).
- [81] H.L. Packer, D.E. Gauden, and J.P. Armitage, *The behavioural response of anaerobic Rhodobacter sphaeroides to temporal stimuli*, Microbiology **142**, 593–599 (1996).
- [82] D.S.H. Shah, S.L. Porter, A.C. Martin, P.A. Hamblin, and J.P. Armitage, *Fine tuning bacterial chemotaxis: analysis of Rhodobacter sphaeroides behaviour under aerobic and anaerobic conditions by mutation of the major chemotaxis operons and cheY genes*, The EMBO Journal **19**, 4601–4613 (2000).
- [83] P.S. Poole, R.L. Williams, and J.P. Armitage, *Chemotactic responses of Rhodobacter sphaeroides in the absence of apparent adaptation*, Archives of Microbiology **153**, 368–372 (1990).

-
- [84] S. Brown, P.S. Poole, W. Jeziorska, and J.P. Armitage, *Chemokinesis in Rhodobacter sphaeroides is the result of a long term increase in the rate of flagellar rotation*, Biochimica et biophysica acta. Bioenergetics **1141**, 309–312 (1993).
- [85] H.L. Packer, H. Lawther, and J.P. Armitage, *The Rhodobacter sphaeroides flagellar motor is a variable-speed rotor*, FEBS Letters **409**, 37–40 (1997).
- [86] M.W. Allersma, F. Gittes, M.J. deCastro, R.J. Stewart, and C.F. Schmidt, *Two-dimensional tracking of ncd motility by back focal plane interferometry*, Biophysical Journal **74**, 1074–1085 (1998).
- [87] K.C. Neuman, E.H. Chadd, G.F. Liu, K. Bergman, and S.M. Block, *Characterisation of photodamage to Escherichia coli in optical traps*, Biophysical Journal **77**, 2856–2863 (1999).
- [88] S. Hormeno and J.R. Arias-Gonzalez, *Exploring mechanochemical processes in the cell with optical tweezers*, Biology of the Cell **98**, 679–95 (2006).
- [89] K.C. Neuman and S.M. Block, *Optical trapping*, Review of Scientific Instruments **75**, 2787–2809 (2004).
- [90] J.E. Molloy and M.J. Padgett, *Lights, action: optical tweezers*, Contemporary Physics **43**, 241–258 (2002).
- [91] R.J. Penfold and J.M. Pemberton, *An improved suicide vector for construction of chromosomal insertion mutations in bacteria*, Gene **118**, 145–146 (1992).
- [92] R.E. Sockett and J.P. Armitage, *Isolation, characterization, and complementation of a paralyzed flagellar mutant of Rhodobacter sphaeroides WS8*, Journal of Bacteriology **173**, 2786–2790 (1991).
- [93] A.C. Ind, S.L. Porter, E.D. Byles, S.A.C. Godfrey, M.T. Brown, and J.P. Armitage, *An inducible expression plasmid for Rhodobacter sphaeroides and its use to investigate chemotaxis* (In preparation).
- [94] A. Schafer, A. Tauch, W. Jager, J. Kalinowski, G. Thierbach, and A. Puhler, *Small mobilizable multi-purpose cloning vectors derived from the Escherichia coli plasmids pK18 and pK19: selection of defined deletions in the chromosome of Corynebacterium glutamicum*, Gene **145**, 69–73 (1994).

-
- [95] D.S.H. Shah, S.L. Porter, D.C. Harris, G.H. Wadhams, P.A. Hamblin, and J.P. Armitage, *Identification of a fourth cheY gene in Rhodobacter sphaeroides and interspecies interaction within the bacterial chemotaxis signal transduction pathway*, Molecular Microbiology **35**, 101–112 (2000).
- [96] J. Sambrook and D.W. Russell, **Molecular Cloning: A Laboratory Manual** (CSHL Press, 2001).
- [97] S.L. Porter and J.P. Armitage, *Phosphotransfer in Rhodobacter sphaeroides chemotaxis*, Journal of Molecular Biology **324**, 35–45 (2002).
- [98] D.E. Gauden, **Electron transport dependent taxis in *Rhodobacter sphaeroides***, D.Phil thesis, University of Oxford, 1996.
- [99] Y. Mimori, I. Yamashita, K. Murata, Y. Fujiyoshi, K. Yonekura, C. Toyoshima, and K. Namba, *The structure of the R-type straight flagellar filament of Salmonella at 9 Å resolution by electron cryomicroscopy*, Journal of Molecular Biology **249**, 69–87 (1995).
- [100] T. Pilizota, **A programmable optical angle clamp for rotary molecular motors**, D.Phil thesis, University of Oxford, 2006.
- [101] T. Pilizota, T. Bilyard, F. Bai, M. Futai, H. Hosokawa, and R.M. Berry, *A programmable optical angle clamp for rotary molecular motors*, Biophysical Journal **93**, 264–275 (2007).
- [102] J.W.J. Kerssemakers, E.L. Munteanu, L. Laan, T.L. Noetzel, M.E. Janson, and M. Dogterom, *Assembly dynamics of microtubules at molecular resolution*, Nature **442**, 709–712 (2006).
- [103] J.S. Parkinson, *Complementation analysis and deletion mapping of Escherichia coli mutants defective in chemotaxis*, Journal of Bacteriology **135**, 45–53 (1978).
- [104] D.K. Fuhrer and G.W. Ordal, *Bacillus subtilis CheN, a homolog of CheA, the central regulator of chemotaxis in Escherichia coli*, Journal of Bacteriology **173**, 7443–7448 (1991).
- [105] L.F. Garritty and G.W. Ordal, *Activation of the CheA kinase by asparagine in Bacillus subtilis chemotaxis*, Microbiology **143**, 2945–2951 (1997).

-
- [106] P.S. Poole, S. Brown, D. Counsell, and J.P. Armitage, *The effect of phosphate on the motility of Rhodobacter sphaeroides*, FEMS Microbiology Letters **79**, 1–4 (1991).
- [107] V. Sourjik and R. Schmitt, *Different roles of CheY₁ and CheY₂ in the chemotaxis of Rhizobium meliloti*, Molecular Microbiology **22**, 427–436 (1996).
- [108] M. Kojima, R. Kubo, T. Yakushi, M. Homma, and I. Kawagishi, *The bidirectional polar and unidirectional lateral flagellar motors of Vibrio alginolyticus are controlled by a single CheY species*, Molecular Microbiology **64**, 57–67 (2007).
- [109] J.L. Appleby and R.B. Bourret, *Activation of CheY mutant D57N by phosphorylation at an alternative site, Ser-56*, Molecular Microbiology **34**, 915–925 (1999).
- [110] A. Bren and M. Eisenbach, *The N terminus of the flagellar switch protein, FliM, is the binding domain for the chemotactic response regulator, CheY*, Journal of Molecular Biology **278**, 507–514 (1998).
- [111] H. Sockett, S. Yamaguchi, M. Kihara, V.M. Irikura, and R.M. Macnab, *Molecular analysis of the flagellar switch protein FliM of Salmonella typhimurium*, Journal of Bacteriology **174**, 793–806 (1992).
- [112] C.L. Gardel and J.J. Mekalanos, *Alterations in Vibrio cholerae motility phenotypes correlate with changes in virulence factor expression*, Infection and Immunity **64**, 2246–2255 (1996).
- [113] J.K. Hatt and P.N. Rather, *Characterization of a novel gene, wosA, regulating FlhDC expression in Proteus mirabilis*, Journal of Bacteriology **190**, 1946–1955 (2008).
- [114] J. Mantotta, **Analysis of chemosensory proteins in Rhodobacter sphaeroides**, D.Phil thesis, University of Oxford, 2002.
- [115] M. Gould, **Chemotaxis gene expression in Rhodobacter sphaeroides WS8N**, D.Phil thesis, University of Oxford, 2006.
- [116] M. Li and G.L. Hazelbauer, *Cellular stoichiometry of the components of the chemotaxis signaling complex*, Journal of Bacteriology **186**, 3687–3694 (2004).

-
- [117] A. Hyakutake, M. Homma, M.J. Austin, M.A. Boin, C.C. Häse, and I. Kawagishi, *Only one of the five CheY homologs in Vibrio cholerae directly switches flagellar rotation*, Journal of Bacteriology **187**, 8403–8410 (2005).
- [118] R.B. Bourret, S.K. Drake, S.A. Chervitz, M.I. Simon, and J.J. Falke, *Activation of the phosphosignaling protein CheY. II. Analysis of activated mutants by ¹⁹F NMR and protein engineering*, Journal of Biological Chemistry **268**, 13089–13096 (1993).
- [119] C.M. Dyer, M.L. Quillin, A. Campos, J. Lu, M.M. McEvoy, A.C. Hausrath, E.M. Westbrook, P. Matsumura, B.W. Matthews, and F.W. Dahlquist, *Structure of the constitutively active double mutant CheYD13K Y106W alone and in complex with a FliM peptide*, Journal of Molecular Biology **342**, 1325–1335 (2004).
- [120] M. Schuster, R. Zhao, R.B. Bourret, and E.J. Collins, *Correlated switch binding and signaling in bacterial chemotaxis*, Journal of Biological Chemistry **275**, 19752–19758 (2000).
- [121] G. Kudla, A.W. Murray, D. Tollervey, and J.B. Plotkin, *Coding-sequence determinants of gene expression in Escherichia coli*, Science **324**, 255–258 (2009).
- [122] S.M.C. Newton, J.S. Allen, Z. Cao, Z. Qi, X. Jiang, C. Sprencel, J.D. Igo, S.B. Foster, M.A. Payne, and P.E. Klebba, *Double mutagenesis of a positive charge cluster in the ligand-binding site of the ferric enterobactin receptor, FepA*, Proceedings of the National Academy of Sciences USA **94**, 4560–4565 (1997).
- [123] G.C. Paoli and F.R. Tabita, *Aerobic chemolithoautotrophic growth and RubisCO function in Rhodobacter capsulatus and a spontaneous gain of function mutant of Rhodobacter sphaeroides*, Archives of Microbiology **170**, 8–17 (1998).
- [124] R.B. Bourret, J.F. Hess, and M.I. Simon, *Conserved aspartate residues and phosphorylation in signal transduction by the chemotaxis protein CheY*, Proceedings of the National Academy of Sciences USA **87**, 41–45 (1990).
- [125] K.M. Blair, L. Turner, J.T. Winkelman, H.C. Berg, and D.B. Kearns, *A molecular clutch disables flagella in the Bacillus subtilis biofilm*, Science **320**, 1636–1638 (2008).

-
- [126] S.M. Block, D.F. Blair, and H.C. Berg, *Compliance of bacterial polyhooks measured with optical tweezers*, Cytometry **12**, 492–496 (1991).
- [127] H. Fukuoka, T. Wada, S. Kojima, A. Ishijima, and M. Homma, *Sodium-dependent dynamic assembly of membrane complexes in sodium-driven flagellar motors*, Molecular Microbiology **71**, 825–835 (2009).
- [128] M.G.L. van den Heuvel and C. Dekker, *Motor proteins at work for nanotechnology*, Science **317**, 333–336 (2007).
- [129] K.A. Morehouse, I.G. Goodfellow, and R.E. Sockett, *A chimeric N-terminal Escherichia coli-C-terminal Rhodobacter sphaeroides FliG rotor protein supports bidirectional E. coli flagellar rotation and chemotaxis*, Journal of Bacteriology **187**, 1695–1701 (2005).
- [130] P. Zhang, C.M. Khursigara, L.M. Hartnell, and S. Subramaniam, *Direct visualization of Escherichia coli chemotaxis receptor arrays using cryo-electron microscopy*, Proceedings of the National Academy of Sciences USA **104**, 3777–3781 (2007).
- [131] G.E. Murphy, J.R. Leadbetter, and G.J. Jensen, *In situ structure of the complete Treponema primitia flagellar motor*, Nature **442**, 1062–1064 (2006).
- [132] C.J. Lo, M.C. Leake, T. Pilizota, and R.M. Berry, *Nonequivalence of membrane voltage and ion-gradient as driving forces for the bacterial flagellar motor at low load*, Biophysical Journal **93**, 294–302 (2007).

MEDIA RECIPES AND REAGENTS

LB Medium

Bacto-tryptone 10g/l

Yeast extract 5g/l

NaCl 5g/l

pH 7.0

Succinate Medium

1M Phosphate buffer 20ml

Concentrated base 20ml

Ammonium sulphate 0.5g

Growth factors 2ml

Sodium succinate 2g

NaCl 0.5g

Casamino acids 1g

Made up to 1l, pH 7.2

M22 Medium

As for succinate medium but omitting sodium succinate and casamino acids.

Concentrated Base

Nitriloacetic acid (disodium salt) 5.94g

Metals 44 solution 25ml

MgSO₄·7H₂O 14.5g

CaCl₂·6H₂O 2.5g

FeSO₄·7H₂O 50mg

Ammonium molybdate (4H₂O) 4.6mg

Made up to 1l, pH 6.8. Store at 4 °C.

Metals 44 Solution

EDTA 2.5g

ZnSO₄·7H₂O 11g

FeSO₄·7H₂O 5g

MnSO₄·4H₂O 2g

CuSO₄·5H₂O 0.39g

CoCl₂·6H₂O 0.2g

Boric acid 0.12g

Sulphuric acid 1.5ml

Made up to 1l and filter sterilised. Store at 4 °C.

Growth Factors

NaHCO₃ 50mg

Biotin 2mg

Niacin 100mg

Thiamine 50mg

Made up to 100ml and filter sterilised. Store at 4 °C.

1M Phosphate Buffer

Buffer A 136.8g K₂HPO₄·3H₂O in 600ml water

Buffer B 68g KH₂PO₄ in 500ml water

Mix 61.5ml Buffer A with 38.5ml Buffer B, adjust to pH 7.0 and store at 4 °C.

HEPES

4-(2-hydroxyethyl)-1-piperazineethanesulfonic acid 2.38g in 1l water, pH 7.2 (NaOH)

5X SDS-PAGE Loading Dye

Glycerol 25ml

0.5M Tris pH 6.8 22.5ml

SDS 2.5g

β-mercaptoethanol 2.5g

Phosphate Buffered Saline (PBS) Buffer

NaCl 8g

KCl 0.2g

Na₂HPO₄·12H₂O 1.44g

KH₂PO₄ 0.24g

Made up to 1l, pH 7.4

MOLECULAR MICROBIOLOGY

B.1 PLASMID MAP - pIND4

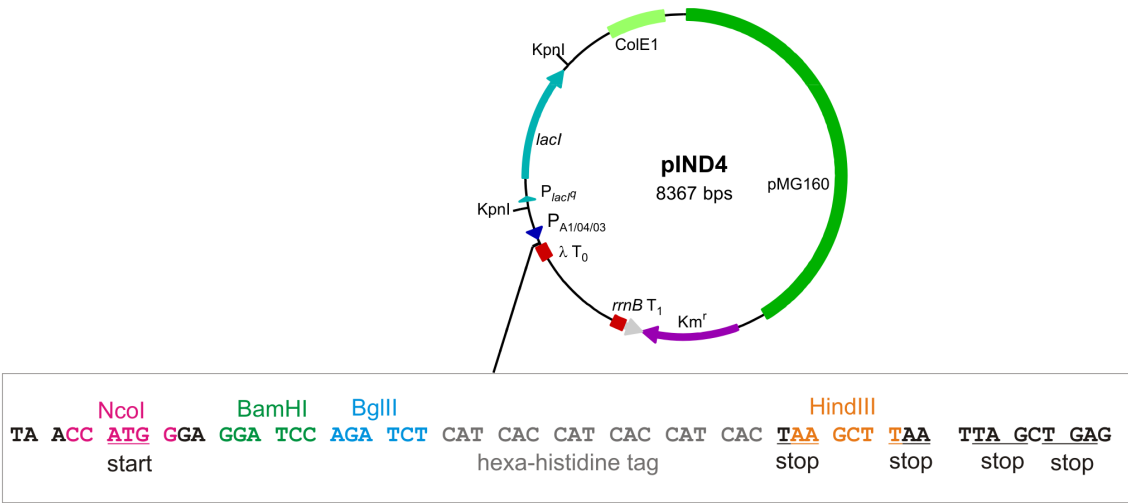


Figure B.1: pIND4 plasmid map showing important features, taken from [93]. Expanded section shows the cloning site - inserts must start with the ATG codon which forms part of the *NcoI* restriction site. If the stop codon of the inserted gene is omitted, a C-terminal histidine tag will be added. All the pIND4 derivatives made in this work included the stop codon so no tag was added.

B.2 PRIMERS

In the tables below, restriction cut sites are underlined and deliberate mutations are marked in **bold**.

Name	Sequence	Restriction Site
Y6-A	AATAC <u>CCCAT</u> GGTGAGCAAGGGCGAGGAG	<i>Nco</i> I
Y6-B	CATCTCGAT GGC GAGCAGGAT	-
Y6-C	ATCCTGCTC GCC ATCGAGATG	-
Y6-D	AATAC <u>GGATCCT</u> CAGGCGGCCATCAGCGTC	<i>Bam</i> HI

Table B.1: Primers for making *yfp-cheY*₆(D56A) using pIND-YFPY6 as a template. The *cheY*₆(D56A) gene was later amplified from this plasmid to give pIND-Y6D56A using primers Y6-F and Y6-R (Table B.3).

Name	Sequence	Restriction Site
Ec-Y-A	TACACCATGGCGGATAAAGAACTT	<i>Nco</i> I
Ec-Y-B	CTTCACCA CCC AGCCACTGGC	-
Ec-Y-C	GCCAGTGGCT TGG GTGGTGAAG	-
Ec-Y-D	ATCG <u>GGATCCT</u> CAAAATCCAAGACTATC	<i>Bam</i> HI

Table B.2: Primers for introducing the Y106W mutation in *E. coli cheY*. The AB PCR was carried out on a pBAD-ecYD13K template. The CD PCR was amplified from *E. coli* RP437 genomic DNA. The overlap PCR (AD) yields a 1053 bp product containing *cheY* (including the two point mutants) and the neighbouring *cheZ* gene. Following digestion, this product was ligated into cut pIND4. After sequencing the correct clone was used as a template to amplify just *cheY*(D13K, Y106W) (commonly known as CheY**) with primers Ec-Y-F and Ec-Y-R (Table B.3).

Name	Target	Sequence	Restriction Site
Ec-Y-F	<i>E. coli cheY</i>	TACACCATGGGGATAAAGAACTT	<i>NcoI</i>
Ec-Y-R	<i>E. coli cheY</i>	ATCGGGATCCTCACATGCCAGTTTCTC	<i>BamHI</i>
Ec-YZ-F	<i>E. coli cheY cheZ</i>	Same as Ec-Y-F	<i>NcoI</i>
Ec-YZ-R	<i>E. coli cheY cheZ</i>	ATCGGGATCCTCAAATCCAAGACTATC	<i>BamHI</i>
Ec-Z-F	<i>E. coli cheZ</i>	AGCTAGGGTCTCCCATGATGCAACCATCAATC	<i>BsaI</i>
Ec-Z-R	<i>E. coli cheZ</i>	Same as Ec-YZ-R	<i>BamHI</i>
Y1-F	<i>cheY₁</i>	AGCTAGGGTCTCCCATGCGGCTGACCGTTCTTGCC	<i>BsaI</i>
Y1-R	<i>cheY₁</i>	AATACGGATCCTCACGGACCGCCACGGG	<i>BamHI</i>
Y2-F	<i>cheY₂</i>	AGCTAGACCTGCATATCATGCGACTCAGGGACAGCATT	<i>BfuAI</i>
Y2-R	<i>cheY₂</i>	AATACAAGCTTTCATAGAGCGCCTACGAC	<i>HindIII</i>
Y3-F	<i>cheY₃</i>	AGCTAGACCTGCATATCATGAGCAGGACGGTTCTCGCC	<i>BfuAI</i>
Y3-R	<i>cheY₃</i>	AATACGGATCCTCATCCGAGCACCTTCTTG	<i>BamHI</i>
Y4-F	<i>cheY₄</i>	AGCTAGACCTGCATATCATGACGAAACCGTCCCTCGCA	<i>BfuAI</i>
Y4-R	<i>cheY₄</i>	AATACGGATCCTCAGCCAAGAAGCTTCTTC	<i>BamHI</i>
Y5-F	<i>cheY₅</i>	AGCTAGACCTGCATATCATGAGCAAGACGATCCTCGCG	<i>BfuAI</i>
Y5-R	<i>cheY₅</i>	AGCTAGACCTGCATATCATGAGCAAGACGATCCTCGCG	<i>BamHI</i>
Y6-F	<i>cheY₆</i>	AGCTAGACCTGCATATCATGCCCTACAATGTCATGATC	<i>BfuAI</i>
Y6-R	<i>cheY₆</i>	AATACGGATCCTCAGGGCGGCATCAGCGTC	<i>BamHI</i>
YFP-Y6-F	<i>yfp-cheY₆</i>	AATACCCATGGTGAGCAAGGGCGAGGAG	<i>NcoI</i>
YFP-Y6-R	<i>yfp-cheY₆</i>	AATACGGATCCTCAGGGCGGCATCAGCGTC	<i>BamHI</i>

Table B.3: Primers for cloning genes into pIND4. All genes were cloned into *NcoI*/*BamHI* cut pIND4 (except for *cheY₂* which was cloned into *NcoI*/*HindIII*) cut pIND4. Note *BsaI* and *BfuAI* are compatible with *NcoI*.

SUPPLEMENTARY DATA

Microscope	Direction of Rotation		
	CCW	CW	Mean % CCW
Trap	121	9	93%
Leica	21	112	16%
Nikon	25	135	16%

Table C.1: The direction of cell body rotation of wild-type tethered cells noted by looking at the monitor/eyepiece. Two slides were made from cultures grown micro-aerobically and were tested on three different microscopes. Note that a motor spinning a bead in the CCW direction would also cause the cell body to rotate in the CCW direction if it were tethered by its filament. Also note that the Trap microscope is inverted, where as the Leica and Nikon microscopes are not (subsequently the direction of rotation is opposite).

Buffer	V_M (mV)	n_{cells}
Succinate medium	-46 ± 14	42
PBS	-103 ± 8	44
PBS _s	-100 ± 9	32
HEPES (anaerobic)	-117 ± 5	41
HEPES	-117 ± 8	28
HEPES + 1 mM propionate	-112 ± 6	35

Table C.2: Membrane voltage (V_M) measured by Dr C-J Lo using a membrane permeable, charge sensitive fluorescent dye, as described in [132]. WS8N was used in all measurements. The mean V_M of cells in PBS_s is $\sim 85\%$ of the V_M of cells in HEPES.

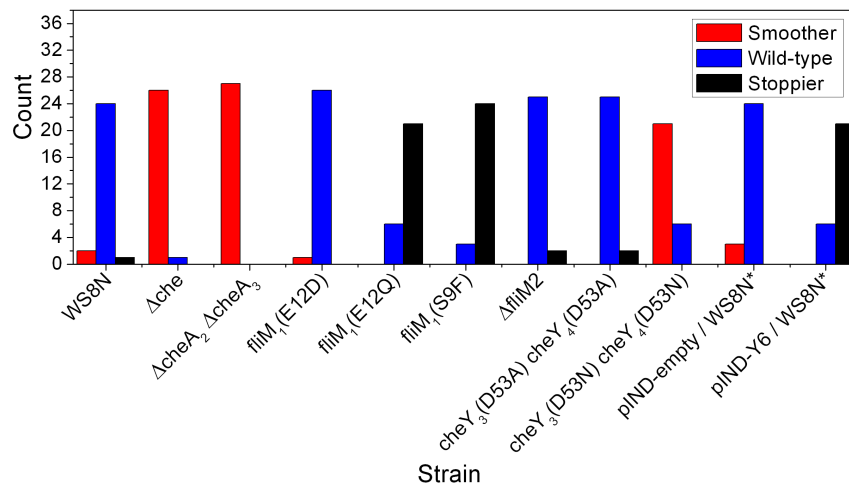


Figure C.1: Free swimming phenotypes of various strains, tested blind in capillary tubes using a light microscope. *Indicates that these strains were grown in the presence of kanamycin and 1 mM IPTG. A chi-squared test was used to find if there a strain was significantly different stop frequency ($P < 0.05$) from the 2:24:1 ratio of WS8N ($df = 2$). Strains JPA1353 (Δche), JPA1319 ($\Delta cheA_2 \Delta cheA_3$), and JPA920 ($cheY_3(D53N) cheY_4(D53N)$) were smoother than WS8N; $fliM_1(E12Q)$, $fliM_1(S9F)$, and pIND-Y6 in WS8N were stopper. The others were not significantly different from WS8N.

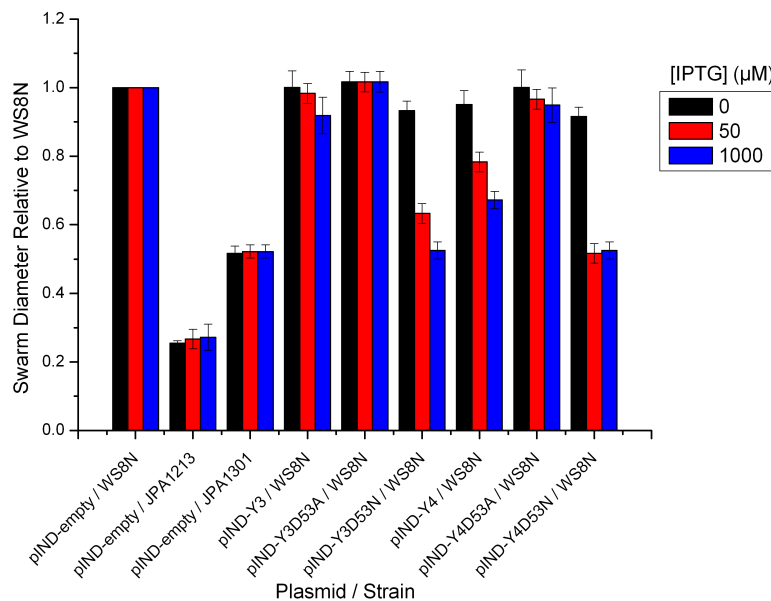


Figure C.2: Swarm diameters of strains overexpressing *cheY*₃, *cheY*₄, and phosphorylation site mutants in WS8N. The D53N mutants have a more severe detrimental effect on taxis than expressing the wild-type genes. JPA1213 (*cheY*₆(D56N)) and JPA1301 ($\Delta cheOp_3$) are non-motile and non-chemotactic controls respectively.

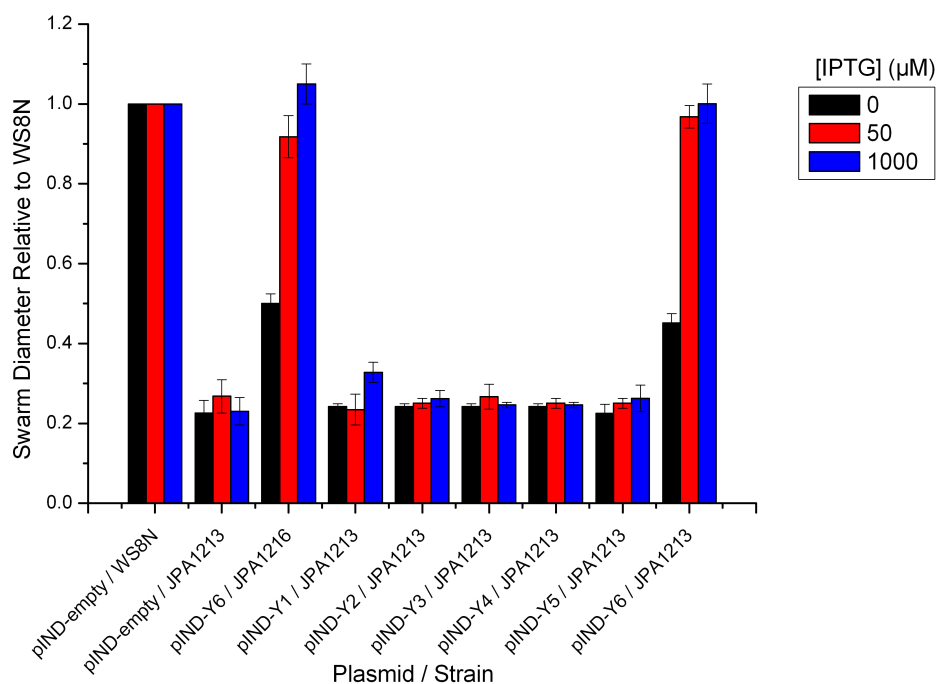


Figure C.3: Swarm diameters of strains expressing various *cheY* genes to see which can relieve the stopped phenotype of JPA1213 (*cheY*₆(D56N)). Note that pIND-Y3D53N or pIND-Y4D53N could not recover motility in JPA1213 either. JPA1216 (*cheY*₆(D56A)) is a non-chemotactic control.

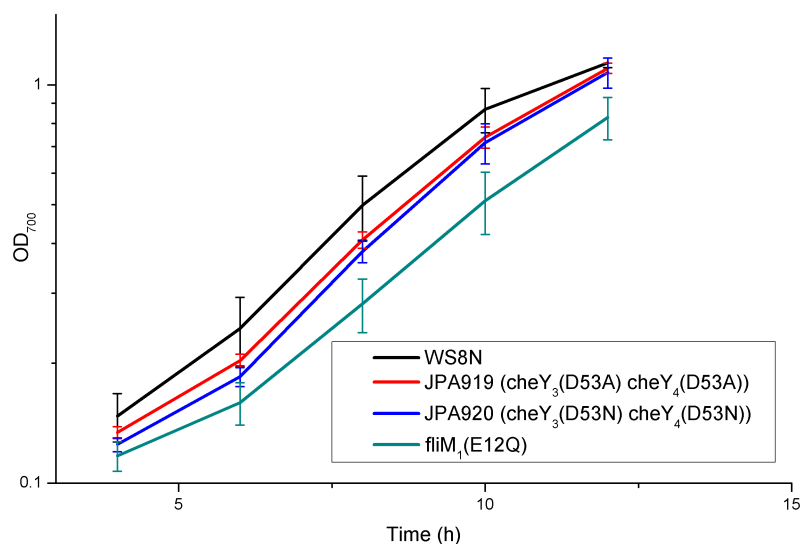


Figure C.4: Comparison of growth rates of three mutant strains relative to WS8N. Cells were grown micro-aerobically. The mean and standard deviation of three independent samples are shown.

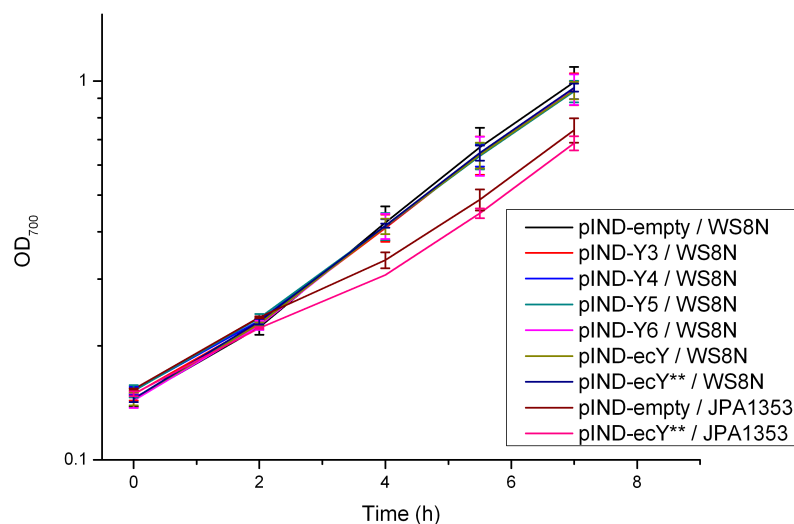


Figure C.5: Comparison of growth rates of WS8N and JPA1353 strains containing pIND4 derivatives. Cells were grown micro-aerobically in the presence of kanamycin and 1 mM IPTG. The mean and standard deviation of three independent samples are shown. JPA1353 strains grow significantly more slowly than pIND-empty / WS8N ($P < 0.05$ ANOVA).

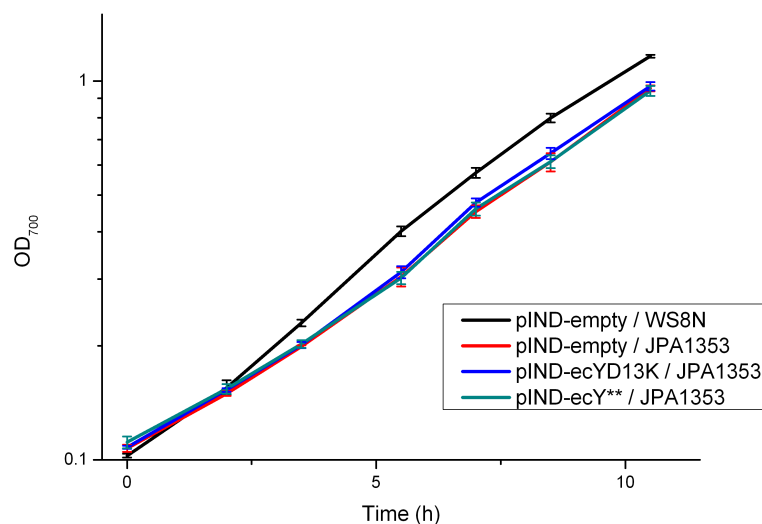


Figure C.6: Comparison of growth rates JPA1353 strains containing pIND4 derivatives relative to pIND-empty/WS8N. Cells were grown micro-aerobically in the presence of kanamycin and 1 mM IPTG. The mean and standard deviation of three independent samples are shown. JPA1353 strains grow significantly more slowly than pIND-empty / WS8N ($P < 0.05$ ANOVA).

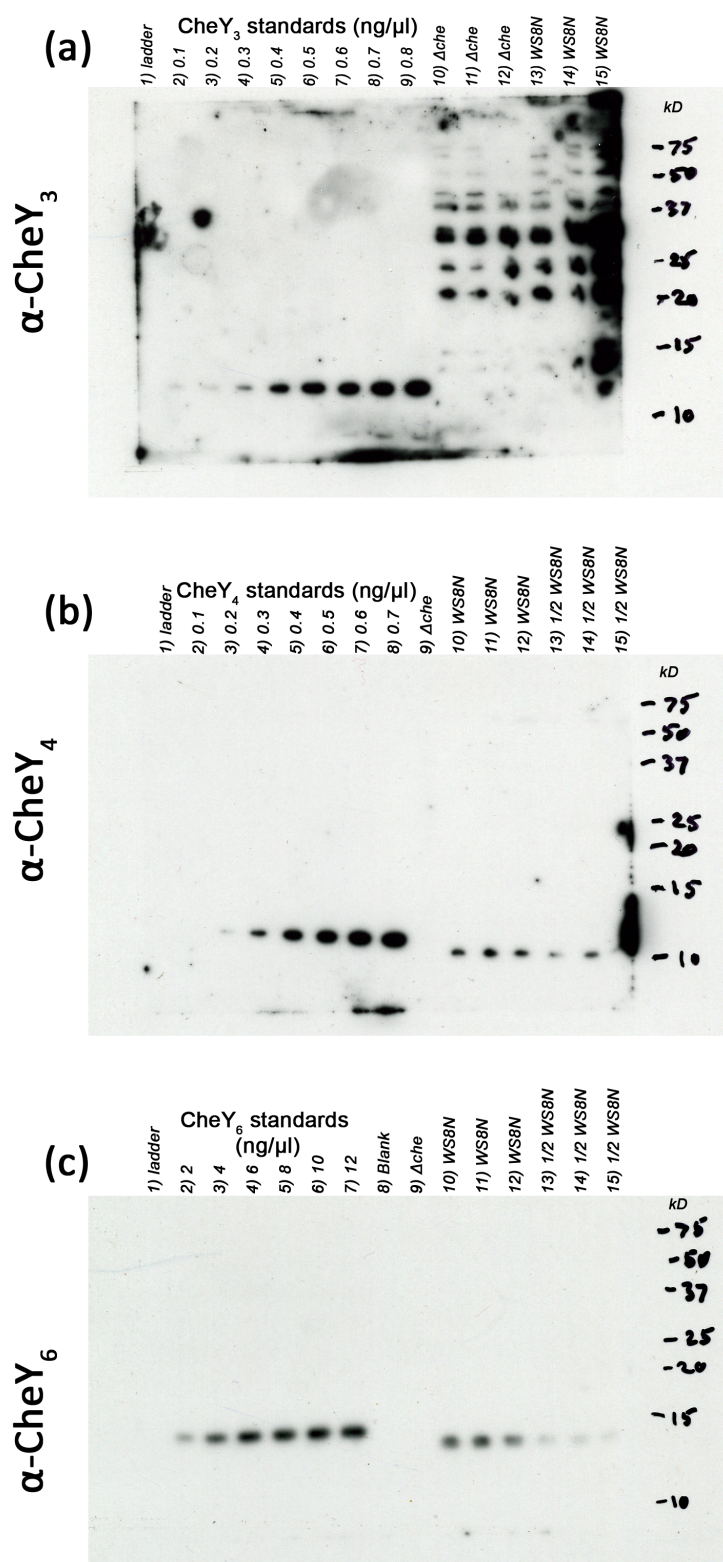


Figure C.7: Western blots probed with α -CheY₃, α -CheY₄, and α -CheY₆ showing the poor specificity of the CheY₃ antibody.

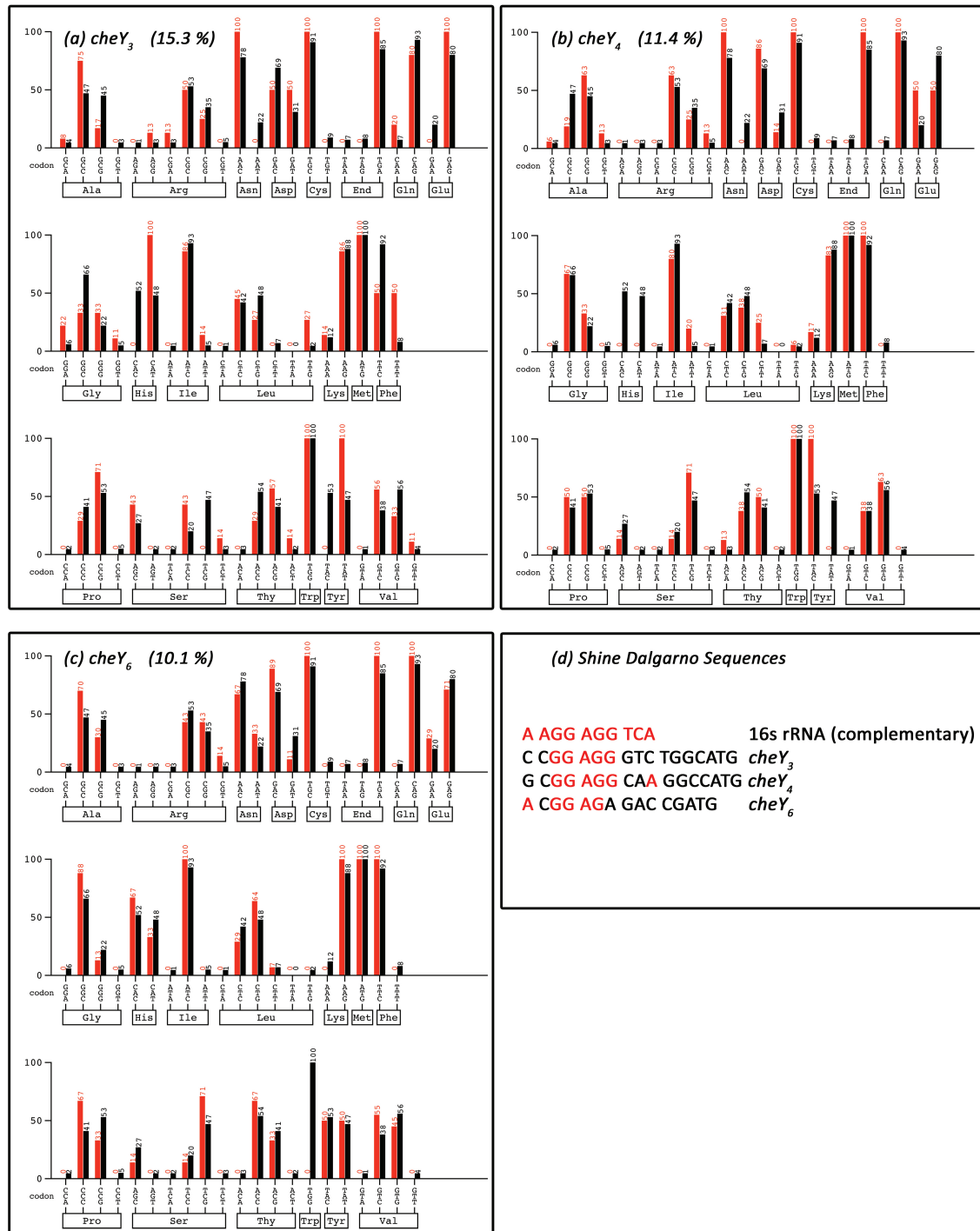


Figure C.8: Codon usage and Shine Dalgarno sequences for *cheY₃*, *cheY₄*, and *cheY₆*. (a–c) Numbers in brackets indicate the mean difference between the *cheY* gene (red) and the average codon usage for *R. sphaeroides* 2.4.1 (black). The average codon usage table was taken from <http://www.kazusa.or.jp/codon/>. Plots were made using the Graphical Codon Usage Analyser (<http://gcua.schoedl.de/>). (d) Shine Dalgarno sequences - bases that match the complementary sequence of the 3' end of the 16S rRNA gene are highlighted in red.

ONLINE RESOURCES

The digital appendix divided into the following sections, is available in a CD at the back of the paper copy or online:

<http://databank.ouls.ox.ac.uk/objects/dataset:3.html>

D.1 THESIS

L^AT_EX files including the style file and figures used to compile this document.

D.2 VIDEOS

Videos relevant to this project.

D.3 MY PROTOCOLS

Step by step protocols used in this project, from molecular biology fundamentals to *R. sphaeroides* swarm plates and the bead assay.

D.4 BEAD ROTATION DATA

Divided into the following sections - (1) Wild-type Bead Rotation Data, (2) JPA1353 Bead Rotation Data, (3) Flow Cell Bead Data, and (4) Analysis Programs.